Fission yield measurements from deuterium-tritium fusion produced neutrons using cyclic neutron activation analysis and γ-γ coincidence counting

by

Bruce D. Pierson

A dissertation submitted in partial fulfillment
of the requirements for the degree of
Doctor of Philosophy
(Nuclear Engineering & Radiological Sciences)
in The University of Michigan
2016

Doctoral Committee:

Professor Sara A. Pozzi, co-chair
Assistant Professor Marek Flaska, Penn. State University, co-chair
Professor, John E. Foster
Larry R. Greenwood, Pacific Northwest National Laboratory
Assistant Professor Physics Thomas Schwarz

This dissertation is dedicated to my family for their unyielding patience and support throughout my graduate career.

ACKNOWLEDGEMENTS

I would like to thank Drs. Marek Flaska, Larry Greenwood, Amanda Prinke, Sara Pozzi, and Sean Stave for their assistance, guidance, mentorship, and revisions to written works; their support and input drastically improved the quality of the final analysis and results (between the five them, I was getting at least one form of support from each of them). I'd also like to thank Drs. Ovidiu Toader and Joe Miklos for their assistance and support in maintaining and managing the Neutron Science Laboratory. Dr. Miklos was instrumental in amending the Nuclear Science Laboratory Nuclear Regulatory Commission license that allowed me to even do the work outlined in this document. He is a good friend and cheered me on to the finish at every opportunity. Dr. Toader was an invaluable resource for tools and ideas, and even emotional support when confronted with complex problems and the, what seemed to be, near endless graduate career. The constant stream of candy that likely helped make Brian Kitchen, Jeff Katalenich, and myself just a bit fatter, served as a nice daily treat.

Without the support of Larry Greenwood, Amanda Prinke, and Sean Stave and the resources of Pacific Northwest National Laboratory, completing this work would have been a nightmare. The complexities of using the original equipment alone would've extended the code development by as much as a year. I have to extend a thanks to Dr. Han Joo of South Korea who's NERS 551 Reactor Design course forced me out of my fortran coding and into C++ while also pushing me to the edge. I've never written so much code in a single semester in my life. Granted, I am not writing any codes for core modeling anymore but the familiarity with it will serve me to the day I die. I'd like to extend a thank you to the

Department of Nuclear Engineering & Radiological Sciences (NERS), specifically Dr. Ron Gilgenbach, for making the effort to help Brian, Jeff, and I after the sudden and unexpected departure of our advisor that left me in what I perceived to be quite a precarious position.

A special thanks goes to Brian Kitchen and Jeff Katalenich. The three of us served as teammates not only in managing aspects of the Neutron Science Laboratory but also as friends and peers to review one anothers work and provide additional ideas and fresh perspective. In all honesty, it would take a separate dissertation to list our adventures in the lab and due justice to how much assistance and support these two provided me. I'll never forget seeing them everyday for four years!

Finally, I have to thank my family. My mother was a constant source of positivity, my brother an excellent escape in humor, and my father a constant source of focus and channeling to isolate and complete the task at hand.

TABLE OF CONTENTS

LIST OF FIGURES

Figure

LIST OF TABLES

Table

LIST OF ABBREVIATIONS

ADC Analog-to-Digital Converter

CERN Conseil Europen pour la Recherche Nuclaire

CNAA Cyclic Neutron Activation Analysis

CTBTO Comprehensive Test Ban Treaty Organization

DAQ Data Aquisition

DHS Department of Homeland Security

d-t Deuterium-tritium

EOI End of Irradiation

ENDF Evaluated Nuclear Data Files

EST asdf

FEP Full-Energy Peak

FIRST Fast Irradiated Rabbit Sample Transfer

GEANT4 Geometry And Tracking toolkit version 4

HPGe High-Purity Germanium

IAEA International Atomic Energy Agency

ITWG International Technical Working Group

low-Z Low Atomic Weight Fission Yield Peak

MCNP6 Monte Carlo N-Particle code version 6

MPB 1σ Mean Prediction Band

MS Mass Spectrometry

ND Non-Destructive

NTNFC National Technical Nuclear Forensics Center

PMT Photomultiplier Tube

SEM Scanning Electron Microscopy

SIMS Secondary Ion Mass Spectrometry

SNM Special Nuclear Material

STAYSL PNNL STAY'SL Pacific Northwest National Laboratory (Neutron Spectrum Least-squares Adjustment Software)

TCS True-Coincidence Summing

UofM-NSL University of Michigan Neutron Science Laboratory

XRF X-ray Fluorescence

ABSTRACT

Isotopic Analysis of Actinides using Active Neutron Interrogation

by

Bruce D. Pierson

The work described in this dissertation used Cyclic Neutron Activation Analysis (CNAA) coupled with gamma-gamma coincidence counting with high-purity germanium detectors to measure the independent and cumulative fission yields of short-lived fission products from thorium-232, uranium-235, and uranium-238. Fission yields of short-lived fission products are needed to enhance the precision and expediency of pre- and post-detonation nuclear forensics. The measurements presented in this work illustrate the large differences in the delayed gamma-ray response following a nuclear detonation. The work performed in this dissertation applied non-destructive CNAA using deuterium-tritium fusion produced neutrons to induce fission. Irradiated targets were shuttled from the irradiation position at the face of the neutron generator to a radiation detection system in less than 0.3 seconds using a pneumatic transfer system. Delayed gamma-rays emitted by fission progeny with half-lives on the order of seconds to several minutes were acquired using three high-purity germanium detectors operating in coincidence. Gamma emissions from this timescale exhibit the largest differences in intensity between individual actinides because of order-of-magnitude variations in independent fission yields for fission products at the wings and valley of the fission product distribution curve.

Fission product decay data from the listed targets were evaluated to measure the fission yields of arsenic-84, selenium-86, bromine-88, krypton-90 and -92, rubidium-94, strontium-94, -95, and -96, yttrium-96m, zirconium-99, barium-143, and lanthanum-146. Time-dependent gamma-ray spectra were used to measure the fission yields of the listed radioisotopes along with: bromine-86 and -87, krypton-89, yttrium-97m and -99, tellurium-136, iodine-136 metastable and ground states, xenon-138, -139, and -140, cesium-140 and -142, and barium and lanthanum-144. All of the measured fission yields have yet to be experimentally determined, with exception to the noble gases. In the near term, these fission yields will improve the accuracy of the fission yields of fission products with half-lives on the order of hours to days produced by deuterium-tritium fusion neutron induced fission. Better precision in the fission yields of longer lived fission products improves the accuracy of the nuclear forensics process. In the future, these fission yields could aid nuclear forensics analyses from a global array of high-resolution gamma spectrometers.

CHAPTER I

Introduction

Nuclear weapons are a serious international concern. Uncooperative countries in control of assembled nuclear weapons and militant political organizations actively working to acquire weapons of mass destruction complicate international commerce and disrupt the natural global socio-economic progression [3, 4, 5, 6]. This issue is only further exacerbated by the concern of clandestine or overt weapons proliferation by the international community. Take, for example, the lack of transparency in the enrichment practices of the Islamic Republic of Iran that geopolitical analysts believe may start a regional nuclear arms race or the proliferation of enrichment technology abetted by A.Q. Khan to Pakistan, Libya, Iran, China, and North Korea [7, 8]. Both of these issues have strained international relations with countries neighboring proliferators and diverted financial resources and focus better spent on infrastructure to support economic growth towards military security.

Given the strong international disdain for nuclear weapons and the threat of international economic sanctions, risks regarding immediate retaliation in force far exceed the original attack and a costly war make overt nuclear weapon strikes improbable. These deterrents leave only one real avenue of attack using nuclear weapons. Directed weapon strikes are most likely to be carried out as clandestine missions designed to mimic an attack from a well funded terrorist organization [9, 10, p. 8; p. vii]. In response to this limited means of attack, forensics techniques designed to identify the source of production of nuclear fuel

used in a nuclear weapon are under development [11]. Current U.S. policy is written such that the producer of the nuclear material is responsible for any incidents involving said material [12]. The ability to identify the source of material acts as a deterrent to nuclear based attacks while encouraging best practices in nuclear materials accountability. These forensics methods are designed to assist in the process of attribution after discovery of a pre- or post-detonation nuclear weapon. The United States, with support from the international community, is actively investigating new approaches of radiological material characterization with a directed focus towards weapons capable actinide materials and mixtures that may be used for illicit or hostile purposes. The techniques and examination of nuclear materials in support of criminal investigations is referred to as "nuclear forensics."

This chapter serves as a brief introduction to the field of nuclear forensics, applications of the work proposed, and the primary problem under investigation within this document. It will close with a short discussion detailing the method to be used for this dissertation, novelty of the approach and data, and the project deliverables of this work.

1.1 Nuclear Forensics

Nuclear forensics is, "the technical means by which nuclear materials, whether intercepted intact or retrieved from post-explosion debris, are characterized (as to composition, physical condition, age, provenance or history) and interpreted (as to provenance, industrial history, and implications for nuclear device design). This characterization and interpretation results from field work to obtain representative samples of the device materials, laboratory analyses, computer modeling, and comparison with databases that contain empirical data from previous analyses of materials samples or that may be the result of numerical simulations of device performance or both. It requires a combination of technical data, relevant databases, and specialized skills and knowledge to retrieve, analyze, and interpret the data," as described by the Joint Working Group of the American Physical Society and the American Association for the Advancement of Science [13]. In more layman terms, nuclear forensics is

the examination of nuclear materials for the purpose of understanding the processing history of the material in support of attribution or exclusion of suspects of a nuclear attack on a civilian population. Nuclear forensics is meant to encourage international safeguards efforts and deter clandestine plans of attack.

The field of nuclear forensics is divided into three technical mission areas.They are: characterization of interdicted pre-detonation samples, interdicted nuclear devices, and post-detonation debris [14]. The focus of this work is post-detonation debris characterization. Post-detonation debris characterization includes trace element and isotopic analysis to discern relevant design characteristics of the weapon indicative of a particular source.

1.2 The Problem: Weapons Grade Whodunit?

Post-nuclear weapon detonation scenarios are difficult to extract reliable data from because the energy release from a nuclear blast destroys nearly all traditional forensic evidence. With the loss of traditional sources of evidence, like trigger components and chemical residue, from an explosion, alternative means of analysis must be employed. For post-nuclear weapon detonations the nuclear fuel, fission products, and bomb components are atomized and blasted into the environment. Depending on the type of detonation, this material settles out of the debris cloud or is captured in melt glass at the detonation locus. Weapon yield, trigger and tamper design, the type of high-explosive used, bomb performance, and other forensically relevant facts about the device can be inferred from the trace element analysis of a bomb site [15, 16, 17, 18, 19, 20, 21, 22]. Historically, debris collected from a detonation site has been examined using a combination of radiochemical and radiation detection measurement techniques and final analysis results were made available over the course of weeks to months [23, 24]. This time-scale of analysis is considered far too long by homeland security agencies concerned about the likelihood of a second event, military and political entities preparing for retaliatory action, and criminal investigators seeking possible culprits. The broad interest question becomes, "how can the process of attribution be

expedited?" This question must be addressed with utmost care. New methods must be tested against and provide similar or better precision than full radiochemical assay before they are trusted. There is no room for error when drawing conclusions about culprits associated with a nuclear attack. Radiochemical purification, radiation detection, and mass spectrometry of debris have been used to determine yields and infer information about bomb design [25, 26, 27, 28, 29, 19, 16]. The majority of these exercises were performed under the assumption that the perpetrator was known; expediency was never a concern nor was providing the information in a judicially acceptable format ever made a priority. Times have changed since the cold war. The threat of a nuclear attack from an easily identifiable culprit is complicated by the threat of a clandestine attack instigated by a terrorist network. Numerous organizations like the International Atomic Energy Agency (IAEA), the United Nations Security Council, the American Physical Society's Panel on Public Affairs (POPA), and the National Academy of Sciences (NAS) have identified an unattributed nuclear attack as an increasingly likely security concern [13]. Current methods, though slow, are reliable and are continually being improved upon. The Comprehensive Nuclear Test Ban Treaty Organization (CTBTO) operates the International Monitoring System (IMS). The IMS is a global array of seismic, acoustic, infrared, and radiation detectors designed to precisely identify the size and location of any nuclear weapon detonation. Resources like the IMS and traditional forensics assay techniques add a constraint to new analysis techniques. New techniques should not interfere drastically with current methods of analysis. Ideally, they should complement the traditional methods while improving the speed and accuracy of the results.

1.3 Methods of Nuclear Forensics Attribution

An assortment of analysis techniques pervade the sciences: x-ray fluorescence, ultraviolet visual spectroscopy, raman spectroscopy, passive gamma-ray spectroscopy, active photon/neutron interrogation and spectroscopy, alpha/beta spectroscopy, coincident radiation

spectroscopy, resonance ion mass spectrometry, inductively coupled plasma mass spectrometry, scanning/transmission electron microscopy, etc. With such a wide variety of analysis techniques available, selecting one method as preferable to the others is exceedingly difficult. Each method has its own pros and cons relative to the others. However, one critical capability necessary to the nuclear forensics mission is isotopic sensitivity. Only two of the listed methods have trace level sensitivities to sample isotopics: mass spectrometric techniques, and radiation detection.

Non-destructive methods like some forms of radiation detection are preferable to destructive methods that depend on chemical separations that are time consuming and energy intensive. Non-destructive actinide material assay techniques fall into one of two categories: active or passive. Both techniques predominantly work by analyzing the time behavior and intensity of ionizing radiation with strong penetrability; i.e., gamma- and x-rays, and neutrons. Active methods make use of well-characterized sources of radiation to stimulate a unique response from the target while passive methods take advantage of naturally occurring nuclear decay inherent to the material for identification. Passive assay techniques are limited to gamma-ray spectroscopy and neutron multiplicity counting, while active methods have a much wider array of gamma-/x-ray and neutron responses available for assay.

1.4 Method Examined: CNAA + gamma-gamma

One method of analysis that is active, non-destructive, and highly penetrating, capable of analyzing large bulk samples, is neutron activation analysis using deuterium-tritium fusion produced neutrons. These 14 MeV neutrons easily penetrate and activate non-hydrogenous material. Activated samples emit highly penetrating gamma-rays that are easily detected using high-purity germanium detectors. Neutron irradiation and detection with high-purity germanium detectors is a method sensitive to a vast range of elements and isotopes with a sensitivity on the order of parts-per-billion [30, 31] in circumstances where radiation background is strictly controlled. The sensitivity and expediency of standard instrumental acti-

vation analysis can be improved by tailoring the irradiation time to preferentially generate short-lived radionuclides. Tailoring is achieved by using short pulses of neutrons. Probing the sample with repeated pulses of neutrons with stop-gaps to measure the sample gamma-ray emissions provides a simple means of improving the statistical precision of the acquired gamma-ray spectra. The high specific activity of short-lived radio-isotopes improves the signal-to-noise, increasing the discriminatory power of the technique [32, 33]. An additional improvement to the technique is achieved by using multiple high-purity germanium detectors operating simultaneously, acquiring separate and coincident data sets. The coincidence spectrum discriminates against spurious background gamma-ray emissions and spreads the acquired data over an additional dimension. The additional dimension decreases peak convolution and background at the expense of detection efficiency, but is still an important and useful means of sample analysis that is provided for free when two or more detectors are available for counting the same sample [34, 35].

The method of cyclically irradiating and counting actinide samples using three matched high-purity germanium detectors operating in coincidence and deuterium-tritum fusion produced 14 MeV neutrons to induce fission, was the method used in this work. Sample transfer times between the detector and neutron generator less than 500 milliseconds were used to quantify significant differences in the delayed gamma-ray response of thorium-232, uranium-238, and uranium-235. Measurable differences in the delayed gamma-ray response from fusion neutron induced fission are discussed regarding its applicability to identifying the actinide fuel of a nuclear weapon using radiation detectors.

1.5 Scientific Justification & Novelty of CNAA + gamma-gamma

Simply put, different actinides produce varied quantities of fission products and these differences in fission product generation can be used to discern the isotopics of the fissioned actinide. Figure 1.1 illustrates the differences in independent fission yields from 14 MeV neutron induced fission between uranium-235 and -238. The largest variations tend to con-

centrate in the lower atomic mass (low-Z) curve as a result of the doubly magic nuclear shell closure at the atomic weight of 132-134 nucleons (52 protons and 80 neutrons) with some variation due to nuclear shape effects [36, p. 148].

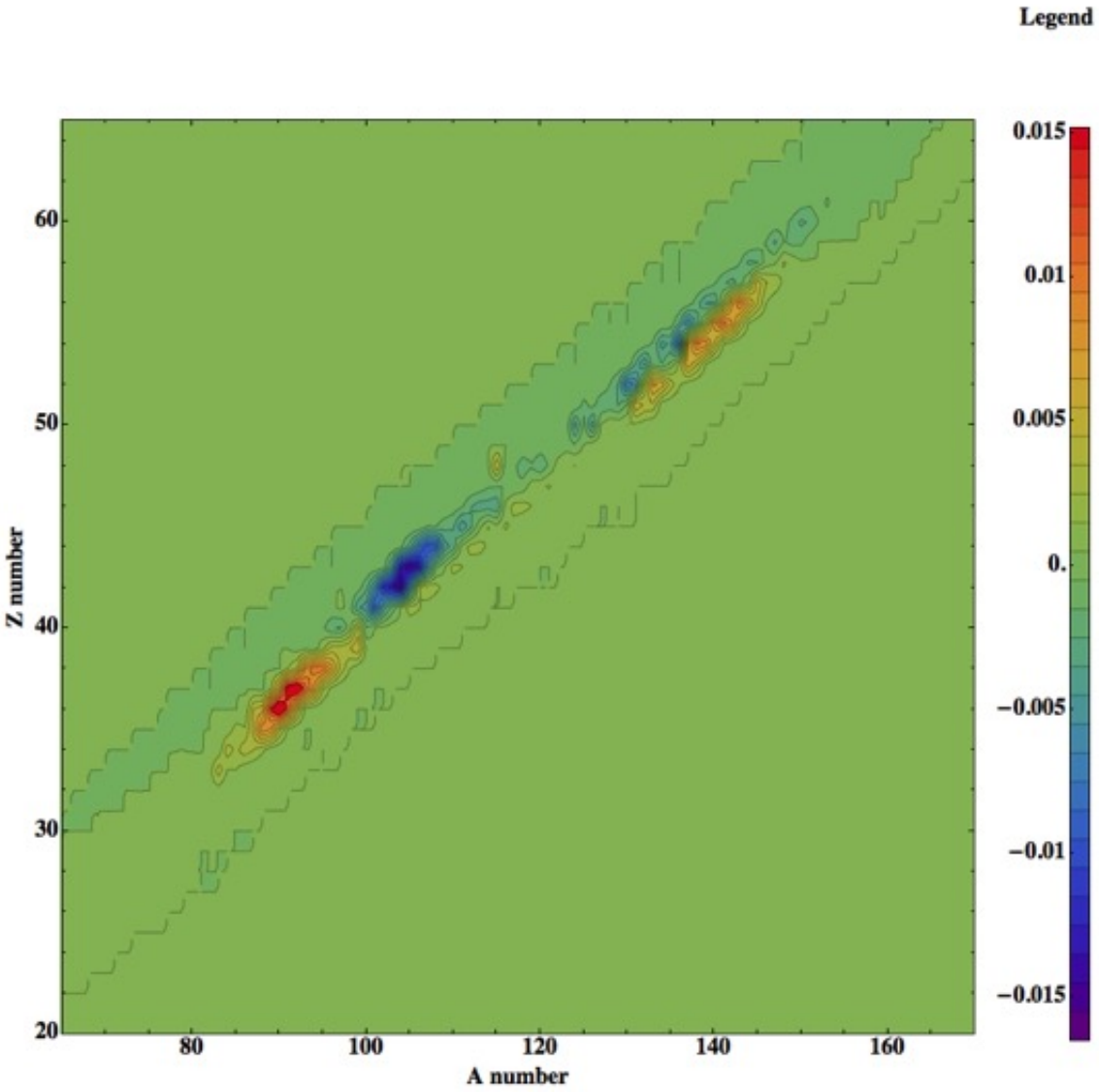

Figure 1.1: Independent fission yield differences between uranium-235 and -238 from 14 MeV neutron induced fission [1].

The largest differences in fission yield in the low-Z mass curve are generally centered along the highest probability fission product of each isobar as predicted by the charge distribution model [37, 38, 39, 40]. High-yield fission products are located far from the line of stability and

have characteristically short half-lives (roughly on the order of seconds); i.e., high specific activity. The application of fission product yield and gamma-line emission ratios has been suggested as a means of actinide characterization for decades [41, 42, 43]. However, none of the previous line ratios suggested have ever used fission products with sub-minute half-lives nor have they made these measurements using 14 MeV neutrons and a gamma-gamma coincidence detection system.

1.6 Summary

CNAA is a proven analysis technique that has been used almost exclusively with reactor neutron sources. Samples analyzed using CNAA were usually chemically processed using gas-jet separators, ion mass separators, or rapid chemical dissolution techniques to isolate individual radioisotopes, commonly fission products [44, 45, 46, 47, 48, 49, 50, 51, 52, 53, 54]. Isolation was necessary to make fundamental nuclear measurements of individual elemental species. CNAA has yet to be applied to examine bulk sample spectra from fissioned actinides to measure delayed gamma-rays from 14 MeV neutrons in the fractional second to minute timeframe. This region of time is both interesting from the perspective of standalone detection of a nuclear weapon detonation and for the development of a portable pulsed neutron source and gamma-gamma coincidence tool for actinide characterization of samples. The work performed in this dissertation optimized a cyclic activation analysis facility and examined the delayed gamma-ray response of thorium-232, uranium-238 (99.9%), and uranium-235 (99.5%). Singles gamma-ray spectra were acquired to estimate the half-lives and independent/cumulative fission yields of detected fission products and to identify quantitative differences in the spectra indicative of the individual actinides.

CHAPTER II

Background

Nuclear forensics is by no means a new field of research. Nuclear forensics analysis is a well developed field of science that has been under review since the first atomic bomb was detonated in Alamogordo, NM in 1944 [55]. Photographic, seismic, chemical, and physical analyses have been reviewed for thousands of nuclear detonations. Chemical digestion, separation, and analysis methods have already been developed and tested to identify the fuel and relevant bomb design information from a detonation sight over decades of testing [24]. Renewed interest in revisiting the processes of nuclear forensics and expanding the state-of-the-art is primarily a result of globalization and terrorism. Technological advancements in, and globalization of, the import of goods make ports of trade critical hubs of economic commerce but also attractive targets for attack or for the smuggling of goods. Add an increase in nuclear materials smuggling and the ability to design and build a crude but functional nuclear weapon from commercially available parts, and the need to enforce nuclear materials accountability becomes readily apparent [56]. Couple the possibility of design variation by amateur bomb designers, and the need for more robust techniques for discerning design characteristics becomes very clear. Finally, consider the fact that the attack is an event under federal investigation where time is a critical part of catching up to and capturing perpetrators and that full radiochemical workup of a detonation sight is a lengthy process, and the need for more rapid analysis methods becomes apparent [23]. The only conclusion

is to revisit and rethink the science from the ground up.

Multiple methods of material analysis, capable of identifying actinide element concentrations within amorphous samples, exist. Several of these methods were listed in section 1.3. Each of these techniques have particular advantages and disadvantages relative to each other. This chapter will review the importance of nuclear forensics and state of the science; it will examine the physics of the two isotopically sensitive analysis methods, mass spectrometry and radiation detection, and identify their respective advantages and disadvantages. Finally, this chapter will close with a final discussion regarding gamma-gamma coincidence analysis and CNAA, highlighting gaps in technical experience and the novelty of the approach.

2.1 Nuclear Forensics

Nuclear forensics is the study of radioactive or nuclear material to determine its purpose and origin. It is a field of study that shares a similar history with nuclear weapons development and proliferation. Some capabilities of nuclear forensics were employed even before the detonation of the first nuclear bomb and were relatively rapidly developed and expanded to meet the needs of the U.S. intelligence community. Throughout the development of this field, time and time-again, isotopic ratios have been the primary signature used to deciphering the history of the material. This section reviews the history of nuclear forensics, why isotopic ratios are so valuable to forensics, and the two primary methods of analyzing isotopic ratios.

2.1.1 History

Nuclear forensics began as a field of study to acquire and analyze information about the German nuclear weapons program in 1944 [57, 24]. The U.S. Airforce set out to capture radio-xenon from the atmosphere at suspected plutonium processing plants in Germany. At that time, the Hanford nuclear site was already producing weapons grade plutonium from B reactor and reprocessing the nuclear fuel at T plant [58]. From that experience, the U.S. government had already learned that fission progeny could be used to locate and track fuel

dissolution at reprocessing facilities. In 1949, the U.S. government successfully exercised their expertise in nuclear forensics analysis by acquiring airborne debris from the first Soviet nuclear weapons test [24, 57]. Subsequent radiochemical dissolution and radiation detection counting were used to infer that the weapon design was a replicate of the first U.S. test, which was indeed the case. Previously, under the direction of General Groves and the oversight of General Dwight Eisenhower, the Airforce developed the Atomic Energy Detection System (AEDS) in 1947. The AEDS relied on radiochemical separation and radiation detection of air filters from planes and rain water [59, 60]. This system would later expand to include infrared sensing satellites and seismic, acoustic, and radiation monitoring stations placed globally [61, 24, 60].

Nuclear weapon fall-out analysis could've aided the Soviet nuclear weapons program during the development of the thermo-nuclear weapon. Initially, the Soviet weapons program tried the "alarm-clock" design and were the first to detonate a boosted nuclear weapon in 1952 but only achieved about 20% burn of the fusion fuel, lithium-deuteride. Because of the low percentage of fusion fuel consumption from this test, it is generally considered a failed test [62]. The difficulty with the "alarm clock" design was that the required energy for compression was too high to truly achieve a thermo-nuclear detonation. Edward Teller, the mother of the U.S. thermo-nuclear weapon, developed a different approach with the assistance of Ullam. The U.S. design used a "staged" nuclear weapon where the fission primary and radiation compressed secondary were kept separate. Had the fall-out of the first U.S. thermo-nuclear test, Ivy Mike, been acquired and analyzed by the Soviet program, their lead scientists would've likely realized the U.S. weapon design was achieving fusion fuel compression well before the detonation of the fission device and concluded the two were separate. Regardless, the Soviets did develop the idea of x-ray induced fusion fuel compression and demonstrated their design using the staged approach in 1955 and later their expertise in 1961 with the largest detonation in human history, "Tsar Bomba", a 50 megaton, three-stage thermonuclear weapon [62]. The Soviets replaced the standard tamper,

depleted-uranium, with lead to decrease the radiation fall-out because of how massive Tsar Bomba was. It derived 97% of the total released energy from the fusion nuclear fuel; this coupled with the lead tamper, meant this bomb design had the lowest radiation fall-out to explosive power ratio of any detonated nuclear weapon [62]. All of this information was made known to the U.S. intelligence community through the use of nuclear forensics.

Today, the Comprehensive Test-ban Treaty Organization (CTBTO), an international organization of the Comprehensive Test-ban Treaty (CTBT) ratified under the Clinton administration, manages a global array of nuclear weapon detection sensors in collaboration with national classified intelligence organizations. The CTBTO is responsible for detection of the last three North Korean nuclear tests and complements the non-proliferation goals enforced by the International Atomic Energy Agency (IAEA) [8]. International organizations such as the CTBTO and the IAEA serve their designed purposes well. The difficulty with these organizations relative to the changing nuclear threat arises from their objectives and operating structure. The CTBTO, being an international organization, requires time to develop the political clout needed to effect change. Currently, the CTBTO and IAEA can only report and monitor on the activities of nation states and their activities associated with detonating and developing nuclear weapon production capabilities. After the fall of the Soviet Union in 1991, nuclear weapon sites and laboratories housing weapons ready material were no longer under strict protection by the government. Employees of these sites, without work, recognizing the value of the material and in need of income were naturally more susceptible to trade of nuclear weapons material for monetary compensation. These sites immediately became international security threats [63, 64]. Criminal organizations and terrorist groups targeted these facilities with the sole purpose of acquiring the necessary material to make a nuclear weapon. The term, "nuclear forensics" was coined starting in 1994 when 560 grams of a mixture of uranium and plutonium-oxide (87.6% enriched in Pu-239) and 210 grams of lithium (89.4% lithium-6) were intercepted at the Munich airport in Germany [65, 66, 67]. Upon discovery of this material, local and international agencies deemed it critical that the

source of this "nuclear material leak" be found. The emphasis and need for improved nuclear materials tracking through nuclear forensics analysis was cemented after the September 11th, 2001 terrorist attack on the world trade center in New York, New York that killed 2996 people.

Since the fall of the Soviet Union more than 442 nuclear material smuggling events have occurred [68, 69, p. 7]. Of the cases that occurred between 1993-2014, 21 have involved HEU and plutonium containing sources [70, 71, 69]. These events indicate severe deficiencies exist in nuclear materials control and accountability in the world and there's no telling how many undetected smuggling events have occurred. In 2003 the Director of the IAEA issued a request to all nations for improvements in nuclear security and prevention of nuclear terrorism [72]. In response, the International Technical Working Group (ITWG) has actively supported nuclear forensics research, the United States has instituted the National Technical Nuclear Forensics Center (NTNFC) under the Department of Homeland Security (DHS), and other nations have followed [73]. Research organizations today funded through the aforementioned organizations are examining ways to expedite the nuclear forensics process and analyses to aid criminal investigations and to identify nuclear material sources that must be secured to stop future smuggling endeavors [11].

2.1.2 Forensics Metrics

This dissertation, thus far, has introduced what nuclear forensics is, why nuclear forensics is important, what sorts of questions nuclear forensics addresses, and several different quantitative analysis techniques used by nuclear forensics scientist, but has yet to describe why or how nuclear forensics works. There are three primary metrics of analysis pertinent to nuclear forensics: isotopic variation, morphology, and chemical composition [25, 74]. Assay of isotopic variation and composition are commonly collected using the same techniques but are treated separately. Isotopic composition is used to identify geography and age while all three are used to infer about the processing history of the material.

There are 90 stable elements that make up all matter on Earth. Most of these materials have immeasurably stable lifetimes, others lifetimes that are inconceivably long compared to the length of recorded human history. These elements were synthesized from the stars that formed, ignited, burned, exploded, and reformed over billions of years. The ratios of the elements and their stable isotopes contained within the Earth have not changed dramatically over the last few millenia; however, isotopic concentrations vary across the planets surface enough to be quantified [75, 17, 15]. Differences in isotopic ratios, chemical purity, material morphology, and age since human manipulation are indicative of the geographic location from where the material was derived and its processing history [76].

The Earth is continuously changing; tectonic shifts, volcanic eruptions, changes in humidity, barometric pressure, and temperature, are all moving atoms around. Isotopes of the same element vary by mass and differences in mass impact their chemical behavior. For example, oxygen-18 has two more neutrons than oxygen-16. When it rains some of that water contains oxygen-18. As surface water evaporates into the atmosphere, lighter oxygen-16 water molecules preferentially evaporate at a faster rate than water containing oxygen-18. If a soil analysis were to be conducted before and after it rained using x-ray fluorescence or scanning electron microscopy an increase in the elemental concentrations of oxygen, hydrogen, and other elements commonly found in small airborne particulate would be observed. If these samples were passed through a mass spectrometer or irradiated and counted using radiation detection, both elemental and isotopic variations in the sample material would become apparent. This trivial example may seem absurd. Why would anyone in their right mind use such rigorous scientific evidence just to indicate it rained and how recently? The answer is, it doesn't rain everywhere everyday. Mining operations, burning of fossil fuels, isotopic enrichment, nuclear reactor transmutation, chemical processing, and many more activities change the isotopic ratios of those 90 stable isotopes. Quantifying isotopic ratios narrows down the set of locations where a material or set of material concentrations would be found. Extrapolating this simple idea to post-nuclear weapon detonation debris characterization

quickly becomes quite complicated.

A battery of questions must be addressed after a nuclear weapon detonation. These include: what was the device yield, what was the primary weapon fuel, was the device boosted, what type of tamper was used, what type of neutron initiator was used, ...etc. Device yield is approximated using the magnitude of the seismic, infrared, and acoustic signals generated by the device. The final estimate of device yield is determined using a concentration ratio of the lanthanide fission products to the concentration of fissile material contained in the nuclear fall-out [77, 16]. Ratios of lanthanides and fissile actinides are commonly used to minimize the impact of fractionation post-detonation on the result. Ratios with lighter fission fragments can be averaged over the detonation sight and from samples acquired from the fall-out plume to improve yield estimates further. The primary fuel is based on the isotopics of the actinides present in the fall-out debris. Higher concentrations of a particular weapon usable actinide (uranium-233, uranium-235, neptunium-237, plutonium-239, and americium-241/243) determines the primary fuel or fuel mixture of the device. Actinide species do not naturally separate isotopically or suffer from significant fractionation in a nuclear detonation. For example, if the uranium-233 concentration were found to be elevated following a nuclear detonation, a likely conclusion would be that a thorium reactor fuel cycle had been used to produce the weapon fuel. More isotopically pure uranium-233, free of fission products and other actinide contaminants regularly present in the thorium fuel cycle, is indicative of a highly sophisticated chemical separation and a controlled irradiation history of the material. Very few research facilities are capable of generating high quality uranium-233; thus, narrowing the range of possible sources. Boosted nuclear weapons are often composed of a particular material, lithium-deuteride. Lithium is an uncommon environmental contaminant. Increased concentrations of lithium would indicate an attempt at a boosted device. Debris from more sophisticated boosted weapons would contain elevated concentrations of lithium enriched in lithium-6. The material of choice for a nuclear weapon tamper is depleted-uranium but other ductile heavy metals like lead may be used, as it was

in Tsar Bomba. Depleted-uranium tamper isotopic concentrations can be used to infer what enrichment technique i.e. what type of facility, this material was generated from. Lead isotopics can be analyzed to determine both the era the lead tamper was purified (pre or post atmospheric testing of nuclear weapons) and its geographic origin. Implosion-type nuclear weapons are significantly more complex than gun-type devices and require a neutron initiator to detonate correctly. Early during weapons development, small mixtures of high-energy alpha emitting radio-isotopes and beryllium were used in initiators. The presence of initiator materials is another indicator related to the complexity of the device. Yield and detailed flux analysis produced using isotopic activation analysis of the top soil can help determine the efficiency of the detonation. All of this information and more can be determined from the fall-out debris from a nuclear weapon detonation. All using isotopic concentration ratios. Morphology of samples around the detonation center can be used to determine the temperature of the detonation which is related to yield and height of the event. Chemical speciation and fractionation are correlated with environmental conditions during the detonation.

2.1.3 Current Assay Methods

Isotopic characterization of sample materials can only be done one of two ways: using mass spectrometric techniques that take advantage of the charge-to-mass ratio of ionized materials, or using radiation detection. Both techniques suffer from different forms of interference. Mass spectrometric techniques have difficulty with atoms and molecules with similar masses like uranium bonded to a single positive hydrogen (UH^+) and plutonium-239. Radiation detection suffers from poor resolution for alpha and beta spectroscopy techniques and efficiency for gamma spectroscopy. Many nuclear transitions relevant to gamma spectroscopy also overlap and require more advanced lower efficiency radiation counting techniques to eliminate these interferences. Regardless, post-detonation debris samples will be highly radioactive. Since radiation detection sensitivity is proportional to the activity of the sample, this form of analysis is most sensitive early on and must be performed before mass

spectrometry. Mass spectrometry is comparable in sensitivity but requires time consuming chemical processing of sample materials before analysis.

2.2 Actinide Analysis & Quantification

The list of neutral actinides and transuranics relevant to nuclear weapons begins at atomic mass number 90; meaning there are 90 or more electrons that orbit the nuclei of these isotopes. So many bound electrons within the Coulomb potential of the nucleus, leads to degeneracies and closely overlapping energy levels in the electron shells of heavy elements. Overlapping energy levels adds complexity and homogeneity to the ionization potential of the heavy elements and complicates chemical methods of elemental isolation. In addition to sharing chemical properties, they are commonly found in low or trace quantities within fall-out debris. These low concentrations limit the set of chemical analysis techniques sensitive enough to identify them; more specifically, the practice of identifying trace actinide constituents is referred to as radiochemistry. Radiochemical assay relies on quantitative separation techniques, radiation detection, and mass spectrometry to characterize complex mixtures of radioactive samples containing trace actinides i.e. fission product samples. Many of the actinides have multiple long-lived isotopes with overlapping masses, making it difficult to discern between actinide isotopes with similar masses using separation techniques reliant upon mass-to-charge ratios, i.e. mass spectrometry, without the support of radiation detection assay.

2.2.1 Radiochemistry

Radiochemistry has long been the work horse of nuclear materials analysis. Solvent extraction, chromatography, co-precipitation, distillation, electro-chemistry and many other separations techniques are all different methods of isolating single elements from complex mixtures. Oxidation and reduction of charge using different concentrations of acids is used to selectively isolate particular charge states of actinide chemical species. For solvent extrac-

tion, immiscible organic and aqueous phases are contacted; based on the polarity, charge, and molecular size of particular chemical species, these different phases have different retention affinities [78, 79]. For chromatography, the sample material is put in contact with an immobile phase. Based, once again on charge, polarity, and molecular size, different chemical species will stick to the immobile phase [80]. With precipitation, the analyte of interest is pushed into an immiscible chemical phase in solution and can be separated using centrifuge, decantation, or filtration methods [19, 81, 74]. When the concentration of the analyte of interest is incredibly small like part-per-million/billion concentrations, the precipitation process is aided using a scavenger [67]. When a scavenger is used, it is referred to as co-precipitation. Distillation relies on differences in the heat of vaporization to separate chemical species. Electro-chemistry uses electrical charge to enhance the migration of different charge species within a material. For example, processes like electro-osmotic flow are used in electrophoresis to isolate anionic and cationic species in solution. Any number of chemical separation techniques can be strung together to isolate and purify particular elements or chemical species of an element. Chemical assay of separations historically have been done using calibrated mass balances. For the case of nuclear forensics, the concentrations of actinide constituents within the sample are commonly so small, they are difficult to measure using a scale. Radiochemistry must be paired with other analysis techniques to provide this information. The only two viable techniques to achieve isotopic sensitivity are mass spectrometry and radiation detection.

Radiochemical separation is often the first step to cleansing a sample to minimize unwanted contaminants and improve the accuracy and precision of applied isotopic analysis techniques. Radiochemistry is time consuming and requires well trained chemistry technicians or quality tested separation apparati to be performed quantitatively. Even with well tested procedures, radiochemistry is sample dependent. The best radiochemical separation procedure must be tailored to the sample material. In contrast, gamma-ray spectroscopy does not require radiochemistry and requires no sample preparation.

2.2.2 Mass Spectrometry

Mass spectrometry retains a unique place in the history of actinide material assay. The original separation technique used to produce the first uranium-235 fueled nuclear weapon was mass spectrometry. Banks of calutrons (high ion current mass separators) were setup at Oak Ridge National Laboratory in the 1940s to extract the 0.7% fraction of the fissile isotope of uranium from uranium-238. Using uranium-hexachloride targets and electron arc ionization, the solid material would be liberated into vacuum as ions and accelerated using an electric field [82, 83]. As the ions were accelerated, they would pass orthogonally across an applied magnetic field. The cross-product of the applied magnetic field and momentum of the uranium ions resulted in a centripetal acceleration. Equation (2.1) is the relationship of the charge-to-mass ratio, $\frac{m}{q}$, and the applied magnetic, B, and electric, E, fields to the radius of curvature, r. The arc path of the uranium ions varied based on the mass of the ionic species. Figure 2.1 is a diagram of how a mass spectrometer works. Magnetic separation later became less prominent as an isotopic enrichment technique because of the limitations on material throughput due to field charge effects in accelerators [84]. However, this technique has become common place in nearly all fields of material science because of its impeccable sensitivity. Current mass spectrometers generally have mass resolutions of less than an atomic mass unit (amu) and sensitivities as low as one part per billion atoms.

$$\frac{m}{q} = \frac{r^2 \cdot B^2}{2E} \tag{2.1}$$

Mass spectrometric techniques used today all require some form of ionization. There are numerous means of ionizing a sample with many variants. These ionization techniques can roughly be categorized as: secondary ion, thermal, glow discharge, spark discharge, and photoionization. Not all of these ionization techniques directly lend themselves to solid samples likely to be encountered at a post-detonation site. The glass matrices containing bomb fission products are unlikely to easily be ionized using thermal, spark discharge, or

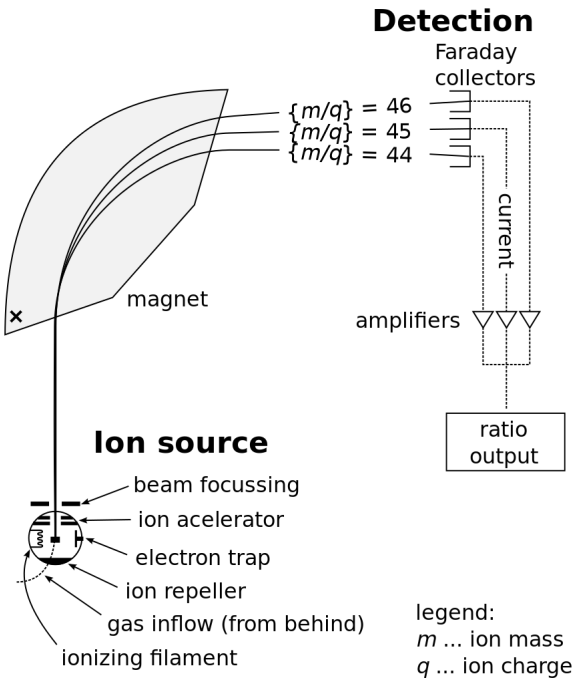

Figure 2.1: Schematic of a mass spectrometer

glow discharge ionization. This only leaves secondary ion and photoionization as readily useable ionization approaches for melt glass.

Secondary ion ionization works by producing a monoenergetic beam of ions that are accelerated into a sample. The impinging ions excite and liberate ionized species from the sample of interest. Those ions are then accelerated through the mass separator analyzer. The difficulty with mass spectrometric techniques is their susceptibility to strong "matrix" effects [17, 85, 86]. As the accelerated ions impinge upon the surface of the analyte, they lose energy in the material. That energy is generally imparted to scattered ionized atoms; however, the energy of ionization is material dependent and leads to preferential ionization of different elements and chemical species [87]. Inhomogeneous samples generally produce widely discordant, spatially dependent results that are more difficult to apply to the attribution process for nuclear forensics [26].

Secondary ion sources coupled with mass spectrometric techniques require sample preparation to improve homogeneity or must be paired with microscopy and matrix matched

standards to produce quantitative results. Well characterized secondary ion mass spectrometry (SIMS) analyzers have sensitivities comparable or superior to non-destructive (ND) gamma spectroscopy, especially for samples with limited radioactivity. It can generally be considered a faster form of in-field analysis relative to other MS techniques because of its higher sample throughput relative to other ionization sources. However, field deployable SIMS systems perform best when paired with complex vacuum systems, are relatively large in comparison to portable germanium detectors, and require large power sources not readily available at a post-detonation sight. Finally, samples acquired in-field immediately following detonation are likely to be highly radioactive; thus, would best be analyzed using radiation detection analysis.

The second, more promising, form of ionization, photoionization, uses tuned laser pulse systems to ablate the surface of a solid analyte. Laser ablation mass spectrometry has been successfully paired with other forms of ionization to improve sensitivity and avoid isobaric interferences. Laser ablation has also been paired with resonance ionization using multi-laser systems. Two lasers, one being an intense ablation source, the second a high-precision frequency tunable source, are offset in time such that the first laser ablates the surface and the second selectively ionizes the material(s) of interest [88]. Dual laser mass spectrometry further enhances elemental species selectivity. As laser technology continues to improve, laser ablation techniques are likely to become the primary method of surface analysis.

It is also worth mentioning that the strong ionization potential of silicate glasses (nuclear detonation debris), do cause matrix effects in laser ablation ionization [85]. Therefore, the two ionization techniques most applicable to solid sample analysis cannot provide repeatable results even from the same target sample, in some cases, without actively correcting for material dependent ionization potentials [89]. Also, both techniques are micro-analysis techniques that only probe the surface of the analyte. Provided the analytes are homogeneous throughout the solid, surface analysis is representative of the whole. Bomb debris from a nuclear blast is never homogeneous because of the highly dynamic temperature gradients

within the plasma ball. As the glass droplets cool and deposit on the ground, different chemical and elemental species solidify within the glass at different temperatures.

Mass spectrometry paired with complex ionization and radiochemical purification is more sensitive than radiation detection analysis using gamma spectroscopy without radiochemistry [25, 90]. However, the overhead to operate mass spectrometers makes it nearly infeasible to deploy at a detonation site currently. With continued research & development compact liquid and gas based MS systems paired with rapid chemical dissolution kits are likely to become the primary means of analysis for nuclear forensics. These future techniques are likely to be complemented by radiation detection in-field assay using gamma spectroscopy.

2.2.3 Radiation Detection

Radiation detection is the method by which radiation quanta are observed. Radiation detectors are used to detect the energy, location, and/or type of radiation. Like mass spectrometry, there are different techniques of radiation detection. The most common radiation detection techniques rely on the most probable forms of radioactive decay: gamma-ray, beta, alpha, and neutron emission. Of these forms of radiation emission, only the two means of decay that emit detectably discrete radiation energies are discussed: gamma-ray and alpha emission. Beta and neutron detection are vital forms of detection that complement the two spectroscopic techniques but are not as sensitive to isotopic variation. Beta decay involves three particles giving the emitted beta-ray a range of energies due to the kinematics. Neutrons are emitted with discrete energies but neutron spectroscopic detectors do not yet have sufficient energy resolution to perform neutron spectroscopy.

2.2.3.1 α Spectroscopy

Alpha particles, helium-4 ions, are emitted from heavy nuclides with atomic weights in excess of 100 atomic mass units. This process of decay is limited to heavier elements for three reasons: 1) such nuclei have nuclear potentials that allow for the tunneling process

inherent to alpha decay, 2) as the mass of the nucleus decreases and approaches 60 atomic mass units, the change in binding energy is no longer large enough for alpha decay to be energetically favorable, relative to other forms of radioactive decay, and 3) the complexity of nuclear de-excitation of spin for atomic weights in excess of 200 atomic mass units quantum mechanically favors zero momentum change particle emission. As more nucleons are packed into the core of the nucleus the nuclear and Coulomb potentials change shape. Assuming for simplicity that the alpha particle preforms within the nucleus, this free particle exists as a quantum mechanical wave within this potential. Only discrete energies or waves can fit within the nuclear potential well of any given nucleus. Changes in nuclear structure vary the nuclear potential, also varying the wave characteristics of the free alpha particle within it. The energies of emitted alpha particles are discrete and unique between different elemental isotopes; thus, alpha spectroscopy is an isotopically sensitive analysis technique.

Alpha spectroscopy is a laboratory intensive method of radiation detection. Because alpha particles are charged, they interact with all other charged particles. Though a single alpha particle from one particular energy level within the nuclear potential is mono-energetic at the moment of emission, that alpha particle must travel a substantial distance before interacting inside of an energy sensitive detector. In its travel, the emitted alpha may interact with the sample itself, with air, or with the dead-layer of the detection medium losing energy. Energy loss in alpha particles degrades the energy resolution and makes it more difficult to discern differences between radioisotopes with alpha emission energies within a hundred keV of one another. To mitigate degradation of the energy resolution, alpha spectroscopy samples must be dissolved, radiochemically purified, electrochemically deposited, and counted in vacuum. Alpha spectroscopy is one of the most sensitive methods of heavy element analysis because the process of alpha emission is almost exclusively observed in heavy elements, thus, limiting possible interferences. However, the complexities inherent to charged particle spectroscopy make this method of radiation detection less suitable as a field deployable assay technique for post-detonation debris.

2.2.3.2 Gamma-ray Spectroscopy

Gamma-ray spectroscopy is a younger technique relative to MS and didn't reach prominence until the advent of the lithium-drifted germanium detector in 1962 [91, 92, 93]. Gamma spectroscopy relies on the photo-electric conversion of gamma-rays emitted from radioactive progeny to identify the isotope. Gamma-rays come in a range of energies from 10 keV up to 10 MeV. The high energy of gamma-rays makes them highly penetrating, meaning they readily escape most materials with limited self-absorption, with some caveats regarding heavier elements.

Gamma-ray spectroscopy is a standard method of radiological material analysis most commonly used in environmental monitoring today [94]. Nuclei in metastable, energetic states with total angular momentum exceeding that of the ground state release their excess energy and momentum through the emission of electromagnetic radiation and, to a lesser extent, internal conversion electrons. Emitted waves of oscillating electric and magnetic energy readily interact with electrons through three primary forms of interaction: photoelectric effect, Compton scattering, and pair production. Gamma-rays that impart some or all of their energy to an electron can be quantized by digitally interpreting the energy of the excited or freed electron. This is done using scintillators, semiconductors, or diffractometers. Scintillators like thallium doped sodium-iodide, the most prominent gamma-ray spectrometer, are the cheapest and most portable but have limited use in Non-Destructive (ND) analysis because of their poor energy resolution. Gamma-rays interacting inside the detection medium excite electrons that produce light. The light is converted to a voltage pulse typically using a photo-multiplier tube (PMT). Electrons liberated from the surface of a charged plate within the PMT by the light emitted from the crystal passes through a cascade of charged plates "multiplying" the signal output. Variations in light emission and absorption within the crystal and the multiplication process of the PMT degrade the repeatability of the output signal given a mono-energetic gamma-ray input. Figure 2.2 illustrates the difference in energy resolution between several scintillators and High-Purity Germanium (HPGe) semiconduc-

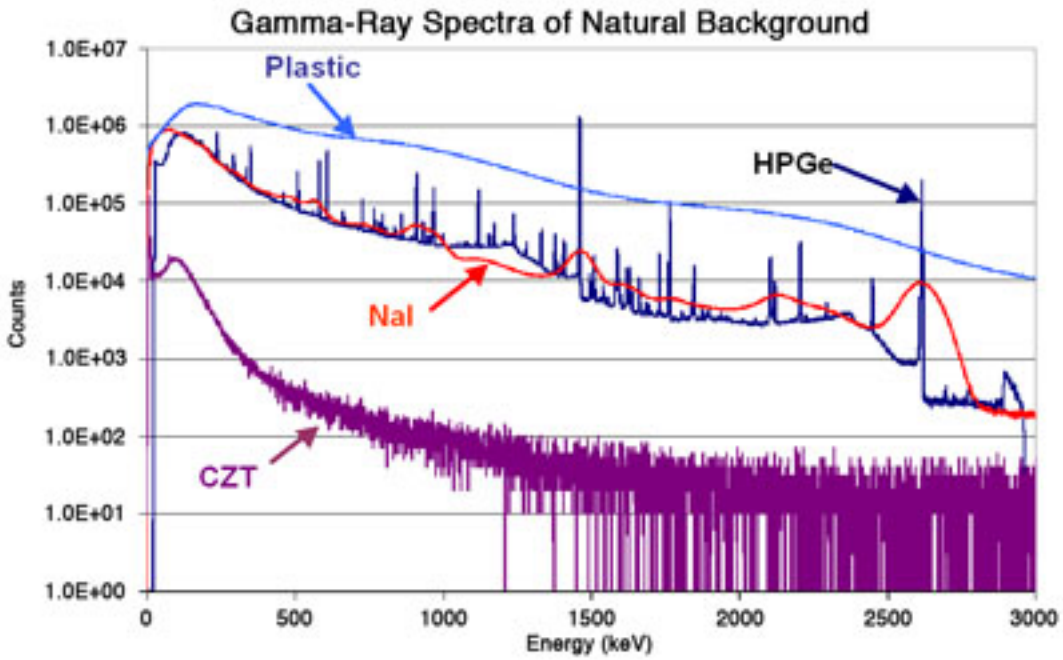

Figure 2.2: Differences in spectroscopic resolution for several gamma-ray detectors.

tor detectors. High-purity germanium, the most prominent semiconductor material used for radiation detection, provides the best energy resolution commercially available to date. Gamma-rays interacting in germanium excite electrons that move into the conduction band of the semiconductor under voltage. The current signal from the semiconductor is converted to a voltage using a simple resistor-capacitor circuit. Peak voltage is binned into a spectrum and is interpreted to be proportional to the incident energy of the interacting gamma-ray. As seen in figure 2.2, the resulting resolution is orders-of-magnitude better than alternative scintillators and semiconductors. Diffractometers used in gamma-ray spectroscopy are characterized as having efficiencies roughly ten orders-of-magnitude less than commercially available spectrometers but resolutions nearing theoretical limits [95, 96].

For the purpose of this work, the discussion will center around high-purity germanium. Germanium was used as a semiconductor during World War II. It was used as a solid state replacement for vacuum tubes by the military in radar equipment. As germanium's prominence as a transistor faded and it was replaced by silicon in the 1950's it was repurposed for radiation detection. The small 0.67 eV band-gap of germanium proved most valuable

in radiation detection where signal-to-noise depended on the number of free charge carriers that could be generated per quanta of radiation energy deposited. However, achieving crystalline germanium with an acceptable depletion depth required either removal of nearly all impurities or balancing of acceptors and receptors [97, p. 405]. In 1962 the first functional germanium detectors were fabricated and tested using lithium as a dopant to balance acceptor regions within the crystal structure. Later, a technique referred to as zone refining was used to achieve purities of part-per-trillion atoms. Zone refining is a technique where by an induction coil passes from one end of a germanium ingot to the other []. As the coil slowly migrates along the length of the ingot, the germanium in the immediate vicinity of the coil melts. Because of the higher solubility of impurities in molten germanium, impurities located adjacent to the heated region migrate into the molten section. Impurities travel along the induction zone and are discarded by segmenting the ingot at the low-purity end. The small band-gap added an additional difficulty to using germanium as a detection material. Germanium detectors had to be cooled to liquid nitrogen temperatures to limit thermal excitation of electrons into the conduction band of the semiconductor. Without cooling, current signals from radiation interactions in germanium are lost in the noise of continuous thermally induced electrical current.

The physics of how gamma-ray spectroscopy in high-purity germanium semiconductor material is done is relatively straight forward. Electromagnetic waves are absorbed by electrons in the valence electron band of the germanium semiconductor exciting said electrons with either the total energy of the photon getting absorbed through the photoelectic effect or part of the energy getting absorbed through Compton scattering. Photoelectric interactions produce current pulses proportional to the incident photon energy; it is the dominant interaction at low energies (below 100 keV). In the intermediate energy range (100 keV - 2 MeV), Compton scatter becomes the dominant interaction probability. Rather than depositing all of its energy, the photon "kinematically" scatters off the electron. Figure 2.3 illustrates the kinematics of Compton scattering.

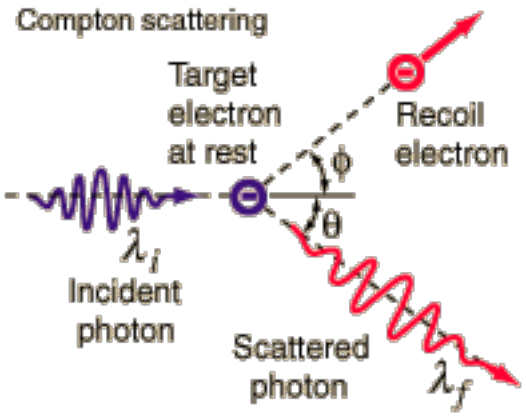

Figure 2.3: Kinematics of Compton scattering.

The mathematics of Compton scattering is derived from the laws of conservation of energy and momentum. The governing equation is provided as equation (2.2). Compton scattering interactions processed into gamma-ray spectra are not mono-energetic; it has the affect of smearing the incident gamma-ray energy across the histogram. Figure 2.4 illustrates the smearing effect of Compton scattering on gamma-ray spectra. Scattering of higher energy photons has the adverse affect of increasing the number of observed events in the lower energy region of the spectrum; thus, decreasing the signal-to-noise of gamma-rays at lower energies. No analog of this affect impacts mass spectrometric techniques making it a clear disadvantage of radiation detection assay.

$$\lambda_i - \lambda_f = \Delta\lambda = \frac{\hbar}{m_e \cdot c}\Big(1 - \cos(\theta)\Big) \tag{2.2}$$

The third interaction type, pair production, can only occur when the incident photon energy exceeds the rest mass energy of an electron and positron (1022 keV). Pair production occurs when the photon interacts with the nucleus producing a virtual Z boson which subsequently transitions into an electron and its anti-particle. Pair production cannot occur without matter. Using the conservation of energy and momentum, disintegration of a photon into an electron and positron is prohibited because the solution is indeterminate. A third body is required to constrain the problem. This third equation is the recoil of the atom

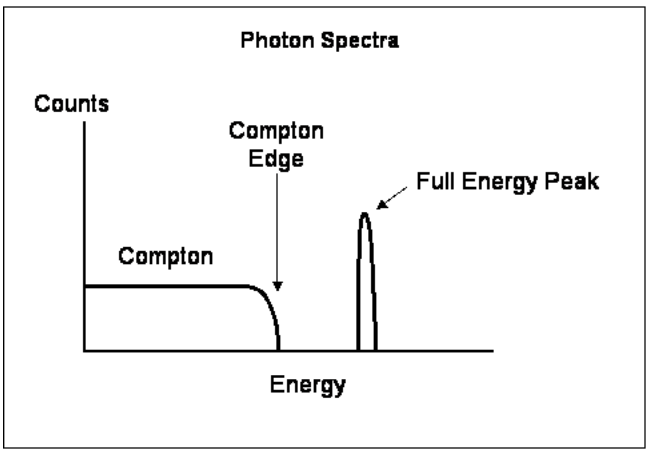

Figure 2.4: Impact of Compton scattering on gamma-ray spectra.

as a result of the pair production event. Pair production, much like Compton scattering, complicates the spectrum because of positron annihilation. Rather than producing a single mono-energetic peak, pair production events generate two peaks, the first 511 keV lower (single escape) than the full-energy peak, the second 1022 keV lower (double escape). This occurrence can be explained by considering the life of the two annihilation photons generated by the positron.

2.2.3.2.1 Radiation Detection Physics

To measure the concentration of an analyte within a sample using radiation detection, the concentration must be correlated to the the intensity of the gamma-radiation. The observation and mathematical relation of the emitted radiation intensity to concentration was derived by Bateman in the mid 1800s [98]. From Bateman's relation, models of the function shapes of the decaying nuclide were derived. These decay shape functions are models of the expected atom density within a decaying sample over time. These functions depend on a set of parameters that are unique to the isotope.

Following neutron activation of a sample, the atom density can be related to the detected gamma-ray emissions using the Bateman equations and a term referred to as the branching ratio. The branching ratio or emission probability variable, Γ_a, is an experimentally deter-

mined value that defines the likelihood that radiation, a, will be emitted per decay of fission product p. The equation for the time dependent emission rate is (2.3)

$$H_p^{(a)}(\vec{r},t) = \Gamma_a \lambda_p N_p(\vec{r},t) \tag{2.3}$$

The emission rate, $H_p^{(a)}$, of gamma-ray a is used to identify the expected interaction rate within a radiation detector. The interaction rate within the detection system is related to the emission rate by the probability the particle is emitted in the direction of the detector ($g_{\varepsilon_a}(\vec{r})$), the probability the particle reaches the detector active volume after traveling through any medium between the particle and the detector ($q_{\varepsilon_a}(\vec{r})$), and finally the probability that once within the detector volume the radiation quanta is absorbed completely (b_{ε_a}). This complex set of probabilities is commonly combined together and referred to as the absolute efficiency of the detection system. Equation (2.4) shows how the interaction rate is related to the emission rate by the various individual probabilities listed above and by the simple absolute efficiency term, ε.

$$I_p^{(a)}(\vec{r},t) = g_{\varepsilon_a}(\vec{r}) q_{\varepsilon_a}(\vec{r}) b_{\varepsilon_a} H_p^{(a)}(\vec{r},t) = \varepsilon_a(\vec{r}) H_p^{(a)}(\vec{r},t) \tag{2.4}$$

The absolute detector efficiency ε_a depends upon the radiation energy and the starting emission location of the energy quanta. The spatial dependence may be neglected by redefining the source emission local as contained within the sample volume rather than treating the sample as a collection of point sources distributed throughout the sample volume. This simplification eliminates the spatial dependence of (2.4), but complicates the process of obtaining the detection efficiency for the sample. Ignoring the spatial dependence of the source requires that any measurement of the efficiency must retain the exact spatial dimensions of the original source. The added complexities of this necessary mathematical simplification

will be discussed.

The radiation-generating source used for these experiments, simplistically, may be thought of as a point source. Generators of this type have large spatial flux gradients that cause non-uniform sample activation. Spatially variant source distributions are difficult to replicate in calibration standards and is commonly ignored. Experimentally measuring the detection efficiency is simplified by neglecting the spatial dependence of the source.

Interactions within the HPGe detector active volume are recorded using an electronics package that collects the current generated by electrons liberated from the semiconductor valence band to the conduction band and translates it to a voltage pulse that is shaped for analysis. In an ideal situation the detector response and the electronic processing of the signal could be treated as a delta function and the interaction rate would also be the count rate recorded by the equipment. Sadly, this is not realistic.

2.2.3.2.2 Radiation Counting Corrections

The observed count rate reported by a HPGe detector from radiation interactions within the crystal lattice is always lower than the true interaction rate because of several factors inherent to the experiment. These factors are the detectors absolute efficiency, sample self-shielding, pulse processing effects, the time-variant sample intensity, and coincidence effects. Each of these factors must be accounted for to extract quantitative information from the data stream. This is done using a variety of tools including Monte Carlo modeling of the neutron generator and sample, non-linear model fitting of the sample intensity and detector dead-time, and modeling and experimentation to determine the coincidence effects.

Cylindrical sources with non-zero heights absorb a portion of the radiation emitted. This effect is referred to as self-shielding. The energy dependence of the absorption probability is unique to the sample material and geometry. For gamma-ray spectroscopy, self-shielding is commonly neglected if three factors are satisfied: (1) the sample materials have low atomic numbers, (2) the material density is much smaller than light metals, and (3) the mean

chord length of the geometry has been minimized. None of these factors characterize the samples irradiated for these experiments. A variety of correction methods have been derived analytically for simple geometries [99]. More complex geometries require a different approach for estimating self-shielding. One such approach used for these experiments, involved the Monte Carlo technique.

High fidelity models of the neutron generator and detectors were developed using Monte Carlo N-Particle (MCNP6), a particle transport code provided by Oak Ridge National Laboratory and GEANT4, a particle transport code provided by CERN. The generator model was used to ascertain the space and energy distribution of the neutron flux incident on the sample from the generator to calculate the fission rates of each actinide target. The modeled neutron flux distribution was corrected using experimental measurements of activation targets and STAYSL PNNL, least-squares neutron spectral adjustment code [100]. The detector model was used to estimate the absolute and total detection efficiency, impact of self-shielding, and impact of angular correlation on the coincidence data. All modeled data was compared with measured results to validate the models.

During pulse processing, two different types of events may occur: (1) pulses from the pre-amplifier may reach the digital processing electronics while it is busy, and (2) multiple interactions may occur at nearly the same time within the detector. These two types of occurrences are referred to as the dead-time and pulse pile-up effects respectively, and each is characterized by a different outcome.

The dead-time effect causes a decrease in the number of recorded events during the processing period because the digital electronics is unable to receive any additional information. The loss of counts from this effect are mitigated by the digital electronics package by monitoring the time the system is available to receive the next event, commonly referred to as system live-time. Modern detectors have a built-in gate monitor that keeps track of live-time and reports it to the user at the end of the collection period. Treating the live-time as the acquisition period exactly corrects for counting losses for sample activities that do not vary

over the detector data collection period.

Pulse pile-up causes multiple independent radiation interactions to be recorded as a single event. The result of a pulse pile-up event is recorded as the sum of all of the simultaneous events; thus, moving recorded events higher in the spectrum. This effect is normally neglected for count-rates that do not induce differences greater than one percent between the detection assay period and the system measured live-time. The fractional difference between the measured live-time and the real elapsed time is commonly referred to as the detector dead-time.

Neither of these factors may be neglected for the experiments performed for this dissertation. Differences between the live-time and elapsed acquisition time immediately after an irradiation have been observed to be as high as 30% following irradiation of uranium-235. Correcting for these effects is further hampered because of the non-linearity of the source intensity.

The sources under investigation in the experiments performed for this dissertation can be characterized as a mixture of hundreds of decaying radioisotopes. During the most active time period immediately following an irradiation, the radioisotopes produced by fission undergo a wealth of change. The neutron rich fission fragments decay via beta, gamma-ray, and the occasional neutron emission. The time-dependent behavior of these radionuclides cannot be expressed as a simple decreasing exponential; the decay functions that govern the atom densities of the various radionuclides generated during the irradiation cycle retain additional variations from alternative production pathways causing an interesting scenario to unfold.

When the activated source returns to the face of the detector, the gamma spectrometer experiences a large in-flux of radiation. The high-intensity source drives the count-rate and the detector dead-time near their limit, saturating the pulse processing electronics with information. The high count-rate and dead-time results in losses in the total number of processed counts because the pulse train from the detector pre-amplifier delivers summed pulses

(pulse pile-up) and the gated pulse processing electronics package spends a significant percentage of the time closed (dead-time). For radionuclides with rapidly decreasing activities over the acquisition period, more of their counts are lost because the detection equipment is less available to process the early interactions due to the pulse pile-up and dead-time effects at the beginning of the acquisition.

Continuing from (2.4), the observed interaction rate, $CR_p^{(a)}$, within the detector is equivalent to the number of interactions of energy, a, multiplied by the probability the detector processes the event as shown in equation (2.5).

$$CR_p^{(a)}(t) = I_p^{(a)}(t) P_d(t) \tag{2.5}$$

The probability of processing the event, P_d, may be viewed as the detectors fractional availability. The only scenario the detector is available to process an event is if the electronics are not busy processing a previous event and if no interaction has occurred within the detector during some period, τ. The variable τ is characterized as the window of time required for the current avalanche within the HPGe semiconductor material to be integrated and is commonly referred to as the detector resolving time. When multiple events occur within a time period shorter than the detector resolving time, the set of interactions is recorded as a single summed event or pulse pile-up event.

The rate of full energy interactions that are accurately recorded (R_a) is equivalent to the product of the radionuclides activity with the detection efficiency (ε_a), the radionuclides gamma-ray branching ratio (Γ_a), and the likelihood that the detector will accurately record the event.

$$R_a(t) = \varepsilon_a \Gamma_a \lambda_p N_p(t) [1 - DT(t)] e^{-\tau I_T(t)} \tag{2.6}$$

Equation (2.6) relates the exact mathematical representation of the observed interaction rate to the true interaction rate. The functions of time on the right-hand side of the equation are the detector fractional dead-time ($DT(t)$) and the true interaction rate within the gamma spectrometer ($I_T(t)$). It is impossible to know the dead-time and interaction rate functions exactly because the resolution of the dead-time function is limited by the time resolution of the gate monitor of the digital electronics package and there is no method of counting every event that occurs within the spectrometer. The exponential term on the right hand-side is derived from the Poisson statistical behavior of radioactivity and represents the likelihood of no event occurring during the time interval, τ. This exponential term can also be related to the sum of probabilities representing the likelihood of one, two, three, etc. . . events occurring as shown in equation (2.7).

$$1 - e^{-\tau I_T(t)} = \sum_{n=1}^{\infty} \frac{(\tau I_T(t))^n e^{-\tau I_T(t)}}{n!} \tag{2.7}$$

By recognizing that the right-hand side of the above equation is the fractional count rate in the detector, it may be redefined as equation (2.8)[101]:

$$\sum_{n=1}^{\infty} \frac{(\tau I_T(t))^n e^{-\tau I_T(t)}}{n!} = \tau N_T(t) \tag{2.8}$$

Where $N_T(t)$ is the total count rate observed by the detector. The product of the true count-rate and the resolving time can never exceed one (equation (2.9)) because the detector throughput over any period of time equivalent to the resolving time cannot exceed one.

$$\tau N_T(t) \leq 1 \tag{2.9}$$

Substituting equations (2.7) and (2.8) into equation (2.6) yields equation (2.10).

$$R_a(t) = \varepsilon_a \Gamma_a \lambda_p N_p(t)[1 - DT(t)][1 - \tau N_T(t)] \tag{2.10}$$

Some liberty has been taken in deriving the above equation relative to the pulse pile-up effect. Equation (2.8) is not strictly true for time varying count rates. The exact relationship requires an averaging of the count throughput term over the resolving time as shown in equation (2.11)

$$\sum_{n=1}^{\infty} \frac{(\tau I_T(t))^n e^{-\tau I_T(t)}}{n!} = \int_t^{t+\tau} N_T(t')dt' \approx \tau N_T(t) \tag{2.11}$$

The initial expression only holds for a constant total interaction rate. However, this approximation should have little effect on the correction if the count rate does not vary drastically over the counting period.

2.2.3.2.3 Gamma-gamma coincidence

Now that gamma-spectroscopy has been introduced, a variant of this technique that is commonly used will be discussed. When counting samples composed of many radioactive substances Compton scattering and photo-peak overlap can obscure low-intensity photo-peaks. One method of drastically decreasing peak overlap is to use gamma-ray emissions that occur in cascades. Figure 2.5 is the decay scheme of ^{60}Co; notice that this particular decay scheme almost always produces a 1.17 MeV gamma-ray immediately followed by a 1.33 MeV gamma-ray. When radioisotopes decay in this manner, two separate radiation detectors can be used to observe each, near simultaneous, emission producing a 2-dimensional spectrum where each energy is binned along a separate orthogonal axis. A higher selectivity for events and squaring of the total spectrum space is achieved by plotting events that occur at almost

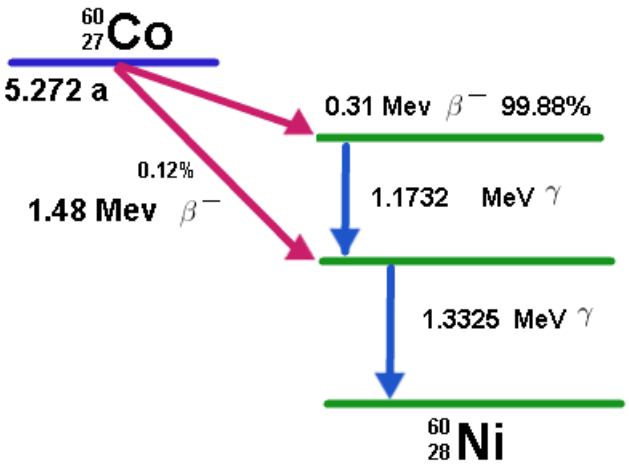

Figure 2.5: Gamma-ray emission cascade of the nickel-60 decay scheme.

the exact sametime from two different detectors i.e. events in coincidence on a 2-dimensional spectrogram. Gamma-ray cascades are, more often, unique to each radioisotope. Photo-peaks observed in coincident spectra are a more definitive means of identifying individual radioisotopes. Using two gamma lines associated with a particular decay scheme and a half-life estimate based on the coincidence rate was used in this work to identify fission product gamma-lines measured in the data.

2.3 Neutron Activation Analysis

Neutrons are one of three fermions that make up the atom. These particles are composed of three quarks, two down quarks and one up quark. Because a neutron is composed of quarks, it is classified as a hadron. Within the hadron family, particles composed of three quarks are called baryons. The combined partial charges of these quarks, -1/3 charge for down quarks and +2/3 charge for up quarks, gives the neutron its neutral charge, its very slight magnetic moment, and slightly larger mass than protons. Neutrons are unique to the the family of subatomic particles because they are the largest long-lived neutral particle: they readily interact with other baryons through the strong nuclear force without being subject to the Coulomb repulsion from protons making them an ideal probe of nuclear structure within

the nucleus. The most intense force within the nucleus is the strong nuclear force. This force is theorized to be predominantly from the interactions of neutrons and protons trading gluons within the nucleus as evidenced by the non-existence of a bound nuclear state between neutrons. Neutron activation analysis uses neutrons to excite the nuclear structure of nuclei through neutron absorption. Neutrons, absorbed by stable nuclei, destabilize the nuclear potential. Bound, unpaired neutrons oscillating within the nuclear core in an outer shell of the nucleus are not as commonly confined by gluon transmission. In an attempt to pair off, one of the down quarks in the unpaired neutron will emit a virtual negative W boson to convert to an up quark. The virtual negative W boson almost instantly disintegrates into an anti-electron neutrino and an electron. The newly converted proton now resides in an energetically unfavorable shell and must re-arrange the nucleus to pair off with another proton or reach a more energetically stable nuclear structure. An example of the natural preference for pairs can be seen in lithium nuclei.

After conversion, a previously neutral particle oscillating within the nucleus is now charged. The charged particle resides within a particular shell now induces either electric and magnetic poles based on its orbit. As the proton de-excites, transitioning to lower shells within the nucleus, the electric/magnetic poles change, generating electromagnetic waves or gamma-rays. The wavelength of these emissions are on the order of the size of the nucleus, picometers, meaning they have order MeV of energy. Emitted gamma-rays interact with electrons as discussed in section 2.2.3.2 and are subsequently used to identify and quantify the atoms activated by neutrons.

Neutron activation analysis paired with radiation detection is a fundamental method of materials analysis. Neutrons are unique because they readily interact with matter and are not affected by the Coulomb force. This means, they are unencumbered by charge repulsion and more freely interact with the nucleus relative to charged particles. Changes in the atomic structure of the nucleus i.e. addition of a neutron, excite the nuclear structure adding energy that must be dissipated. This dissipation processes almost always includes the emission of

gamma-rays that can be quantified and used for materials analysis.

2.3.1 History of NAA

After the discovery of the neutron in 1932 by Chadwick who observed the effect of alpha particles on beryllium and the subsequent generation of protons from interactions of "highly penetrating radiation" in hydrogenous media, it was quickly put to use to probe the nuclear structure of the elements. Alpha emitting radiation sources were mixed with light elements like lithium, boron, and beryllium to produce neutron sources that were used to irradiate different materials producing radiation activation by-products. Some of the earliest uses of neutrons were to measure concentrations of lanthanides by George de Hevesy and Hilde Levi in 1935 [102, 90]. At that time, it was not readily known how to separate the rare-earths chemically; thus, the application of neutrons to measure trace impurities in materials was quickly realized following its discovery. In fact, neutrons were used to discover fission by Lise Meitner and Otto Robert Frisch in 1939. Work using the neutron rapidly accelerated with the advent of the Manhattan project by Franklin Roosevelt at the bequest of Leo Szilard and Albert Einstein on recognition, "...that extremely powerful bombs of a new type may thus be constructed." During the Manhattan project it was discovered that piles of uranium could be used to sustain a chain reaction of fission. This lead to the invention of the nuclear reactor. Today, nuclear reactors are the largest sources of neutrons available. Their uses include power production, material degradation by radiation studies, and materials characterization using neutron effects on nuclear structure.

Today, neutron activation analysis is recognized as one of the primary methods of material assay using the comparator or ratio technique [90, 31, 35]. CNAA facilities like the NSL facility have been used for impurity analysis of elements with isotopes that exhibit high specific activity after bombardment with 14 MeV neutrons [103]. Numerous types of neutron sources are used from the original small alpha-neutron and accelerator nuclear fusion sources, to high energy-density nuclear reactors, GeV accelerators, and nuclear weapons. Though

NAA is one of the most sensitive forms of material assay, comparable to mass separation techniques, it is not predominantly used. The infrastructure cost requirements and regulatory limitations in relation to neutron generating devices, and limited number of trained NAA experts make this form of analysis less cost-competitive to alternatives with comparable statistical certainty.

2.3.2 History of Neutron Induced Fission Yield Measurements

Fission is a complex and violent reaction; it involves numerous physical effects like charge, shape, volume, surface area, and quantum effects like nucleon pairing and shell structure [104]. Short-comings of the Bohr liquid drop model were observed from the discovery of isomer states of actinides with order 10^{10} higher spontaneous fission rates in the late 1960s [105]. However, significant improvements in fission probability calculations have been made since the inception of the liquid drop model using more detailed dynamic calculations of the unstable pre-scission compound nuclei [106, 104]. Theoretical results from calculations using improved modeling capabilities have been affirmed from data acquired from charged particle induced fission and in some cases neutron induced fission [107]. Still more data is needed to test the predictive capabilities of current models to extend the reliability of the current nuclear data into new energy and time regimes.

One important focus of validating the predictive accuracy of these models is post-detonation nuclear forensics. Nuclear and thermo-nuclear weapons will generate a mixed neutron energy spectrum that produces detectable differences in fission product concentrations in the debris [108, 20, 15]. Because fission product concentrations in debris from different actinides vary comparably, it is necessary to minimize the uncertainty in the prediction of fission products and yields from fission induced by neutrons within the thermal to deuterium-tritium fusion produced neutron energy range. By minimizing the uncertainty in the prediction of fission product concentrations post-detonation, uncertainties in fuel characteristics of the device are decreased; thus, shortening the list of materials or material producers that either directly

assisted in producing the weapon or lost control of weapons capable nuclear material. Historically, d-t fusion produced neutron sources have been small relative to reactor sources, nominally 2-5 orders of magnitude lower in flux than a 1 MW TRIGA reactor [109]. The largest d-t neutron source, the second generation Rotating Target Neutron Source (RTNS-II) at the Livermore Laboratory, was capable of producing nominally $3{\cdot}10^{1}3$ neutrons per second at 13-15 MeV using a beam current of 150 mA [110, 111]. This source, and earlier iterations, were used to extend the measured fission yield curve down to Ni66 and up to Er169 [112, 113, 114]. D-t fusion produced neutrons have predominantly been used by Los Alamos and Lawrence Livermore National Laboratories (LANL and LLNL) to induce fission in numerous actinide materials [115, 116]. Fission yields were measured using either radiation detection then radiochemistry or the reverse and mass spectrometry: using the aforementioned process, the shortest-lived fission products examined were zirconium-97 and gadolinium-159 with half-lives of 16.8 and 18.5 hours, respectively from the Los Alamos study and antimony-130 and cesium-138 with half-lives of 39.5 and 32.2 minutes, respectively for the Livermore work. Samples were irradiated for a fixed irradiation interval before using beta, gamma, and/or neutron mutli-scaling to examine the delayed fission product radiation response [115, 116, 117]. After measuring the delayed response following fission, samples were chemically separated for counting using beta and gamma ray detection equipment. After counting, samples were studied using mass spectrometry either to support or independently measure the cumulative fission product yields initially estimated using radiation detection. Little work has been done to examine the yields for fission products at seconds at fusion neutron energies. An additional caveat to previous measurements of short-lived fission products, fission yield estimates of these fission products were acquired from gross beta and neutron counting [118]. Measurements acquired in this way are not isolated measurements of the individual isotopes, but measurements of the bulk fraction of fission product isotopes with similar decay characteristics. Meaning, these estimates may include interferences that are difficult to separate from the primary radiation signature of the radioisotope of interest.

The two most precise measurement techniques that can both examine fission products with half-lives as short as microseconds while also isolating individual radioisotope with high precision: 1) radiation detection coupled to a mass separator, and 2) radiation detection coupled to Frisch-gridded ion chambers. Facilities like SPIDER, Lohengrin, OSTIS, Miss Piggy, and others use planchets with a thin film of isotopically pure actinide material that was either electro or vapor deposited. The planchets were placed in a vacuum chamber to study either charged particle or neutron induced fission, or spontaneous fission. The technologies used to support the resources necessary to use these two high-precision techniques requires financial overhead on the order of millions of dollars. Because of personnel and budgetary constraints, this method of fission yield analysis could not be used.

A less financially limiting technique for fission product study is neutron activation analysis. CNAA provides access to short-lived fission product decay data at a modest increase in expense over standard or instrumental neutron activation analysis [118]. CNAA coupled with a low-intensity neutron source relies on repetition to achieve usable radiation counting statistics. This technique is a non-destructive assay method where an isotopically pure actinide sample is irradiated to saturate the activity of fission products with half-lives comparable to the irradiation time. The irradiated sample is then counted for a period of time roughly equal to or longer than the irradiation time. The process of irradiation followed by counting is repeated and radiation detection data acquired from each counting period are summed until the desired precision is achieved [42, 119]. Because this method examines all of the fission products without separation, the most difficult problem to overcome is gamma-ray interference between fission products that degrade the accuracy of fission yield estimates made from gamma-ray peak areas. The method used in this work to avoid analyzing gamma-ray peaks with interferences was gamma-gamma coincidence.

Gamma-gamma coincidence is a method where by two gamma-ray detectors observe nuclear transitions, unique to particular radioisotopes, by only recording data from the two detectors when an event is registered in both detectors within a small time window of each

other (usually the time window is on the order of 10s to 100s of nanoseconds). This method, coupled with CNAA for bulk fission product counting, can be used to identify interferences with gamma-ray peaks observed in the singles gamma-ray data [120].

2.3.3 Sensitivity

Neutron activation analysis is a method with comparable sensitivity to mass spectrometry [121, 90, 31]. Sensitivities on the order of nanograms per gram of sample is not unexpected using NAA, especially for materials with large neutron interaction probabilities.

Neutron activation analysis is a spectroscopic technique that must contend with interference and background affects that are far more prominent than in mass spectrometry. One of the largest advantages to gamma-ray spectroscopy is also one of its biggest disadvantages. As discussed in an earlier section gamma-rays are highly penetrating; when they interact in materials, they do not always fully deposit their energy.

2.3.4 Sample Activation

Neutron activation and decay is a dynamic process that depends on the spatial distribution of materials and the time, space, and energy dependence of the neutron source. Mathematically, this process may be expressed as (2.12).

$$R(\vec{r},t) = \int_0^\infty \left(\frac{\sum_{i=1} m_i(\vec{r},t) N_{AV} \alpha_i \sigma_i(E)}{M_i} \right) \varphi(\vec{r},\mathbf{E},t) d\mathbf{E} \tag{2.12}$$

Where R is the total fission rate with time and spatial dependence, m is the density of element i, N_{AV} is Avogadros number, α is the atom fraction of the elemental isotope, M is the molar mass, σ is the energy dependent fission cross-section, and φ is the angularly integrated flux with time, energy, and spatial dependence.

This reaction rate determines the fission fragment production rates based on an energy

dependent yield factor specific to each fission fragment pair. This factor is commonly referred to as the independent or individual fission isotope yield. These values have been measured in a variety of ways using gas jets [45, 44], ion accelerators [54], and cyclic activation [122]. The results of these experiments were dependent upon the neutron source average energy. More specifically, results are provided for actinide isotopes from ^{227}Th to ^{255}Fm at neutron energies of 0.0023, 5E5, and 1.4E7 eV. These studies were reviewed and reported in the Evaluated Nuclear Data Files [115, 107, 123, 124]. The values purported for the fission yields in the ENDF/B-VII libraries were calculated using the weighted average of all available experimental data and the results using the charge distribution model [125, 39].

The fission rate can be transformed into the production rate of any fission fragment over an irradiation period by incorporating the energy dependent yield factor as shown in (2.13)

$$G_p(\vec{r},t) = \sum_{i=1} N_i(\vec{r},t)\langle\sigma_i^p(\vec{r},t)\rangle\phi(\vec{r},t) \tag{2.13}$$

Where G is the generation rate of the fission product p, N is the atom density of actinide i, $\langle\sigma_i^p\rangle$ is the yield factor weighted flux averaged production cross-section, and ϕ is the energy integrated flux. The mathematical definitions of these terms are provided as equations (2.14a)–(2.14c). The only new term, $Y_i^{(p)}(\mathbf{E})$, is the energy dependent fractional yield of fission product p for actinide i.

$$N_i(\vec{r},t) = \frac{m_i(\vec{r},t)N_{AV}\alpha_i}{M_i} \tag{2.14a}$$

$$\langle\sigma_i^p(\vec{r},t)\rangle = \frac{\int_0^\infty \sigma_i(\mathbf{E})Y_i^{(p)}(\mathbf{E})\varphi(\vec{r},\mathbf{E},t)d\mathbf{E}}{\int_0^\infty \varphi(\vec{r},\mathbf{E},t)d\mathbf{E}} \tag{2.14b}$$

$$\phi(\vec{r},t) = \int_0^\infty \varphi(\vec{r},\mathbf{E},t)d\mathbf{E} \tag{2.14c}$$

The generation rate can now be incorporated into the Bateman's equations to determine the total atom density of a single fission product of interest. The differential equation governing the production of a single fission product is (2.15)

$$\begin{aligned}\frac{\partial N_p(\vec{r},t)}{\partial t} =& -(\lambda_p + \langle\sigma_p(\vec{r},t)\rangle\phi(\vec{r},t))N_p(\vec{r},t) + \sum_{j=1}\lambda_j N_j(\vec{r},t) \\ &+ \sum_{k=1} N_k(\vec{r},t)\langle\sigma_k^p(\vec{r},t)\rangle\phi(\vec{r},t) + G_p(\vec{r},t) \end{aligned} \tag{2.15}$$

The first term on the right is the loss rate due to radioactive decay and neutron absorption, the second term is the sum of all of the production from radioactive decay from fission product j into p, the third term is the production from nuclear reactions with fission products k that generate p, and the last term is the direct production rate from fission. The differential equation can be solved using an integrating factor. The solution is (2.16)

$$\frac{\partial N_p(\vec{r},t)}{\partial t} + \lambda_p^*(\vec{r},t)N_p(\vec{r},t) = \sum_{j=1}\lambda_j N_j(\vec{r},t) + \sum_{k=1} N_k(\vec{r},t)\langle\sigma_k^p(\vec{r},t)\rangle\phi(\vec{r},t) + G_p(\vec{r},t) \tag{2.16a}$$

$$\frac{\partial}{\partial t}\left(e^{\lambda_p^* t}N_p\right) = e^{\lambda_p^* t}\left(\sum_{j=1}\lambda_j N_j(\vec{r},t) + \sum_{k=1} N_k(\vec{r},t)\langle\sigma_k^p(\vec{r},t)\rangle\phi(\vec{r},t) + G_p(\vec{r},t)\right) \tag{2.16b}$$

$$N_p(\vec{r},t_1) = e^{-\lambda_p^* t_1}\left[\int_0^{t_1} e^{\lambda_p^* t}\left(\sum_{j=1}\lambda_j N_j(\vec{r},t) + \sum_{k=1} N_k(\vec{r},t)\langle\sigma_k^p(\vec{r},t)\langle\phi(\vec{r},t) + G_p(\vec{r},t)\right)dt + N_p(\vec{r},0)\right] \tag{2.16c}$$

Where λ_p^* represents the combined decay and absorption loss coefficient and assumes the

energy integrated flux may be treated as time-invariant as shown in equation (2.17).

$$\lambda_p^* = \lambda_p + \langle \sigma_p(\vec{r}) \rangle \phi(\vec{r}) \tag{2.17a}$$

$$\phi(\vec{r},t) = \phi(\vec{r}) \tag{2.17b}$$

Equation (2.16) can be greatly simplified by observing the differences in magnitude between different generation and loss rates. First, actinides have nucleon-nucleon binding energies that are several hundred keV below the average of their fission fragments. The underlying cause of this variation is the strong repulsive Coulombic force between all of the protons packed within large nuclei. The additional energy from the proton repulsion is mitigated by a larger concentration of neutrons that increase the nuclear strong force. Because actinides are neutron rich and upon fission do not release all of their excess neutrons immediately, their fission products are neutron rich meaning the dominant mode of decay associated with fission products is beta decay ($\lambda_j^{(\beta)}$). In most cases, this fact simplifies the first summation of the above equation by reducing it to one term; a decaying parent isotope along the same isobar of a fission product isotope. An example is provided in figure 2.6. Other, more complicated, scenarios include at most two terms in the first summation of equation (2.16). This is a result of the second most predominant mode of fission product decay, neutron emission ($\lambda_j^{(n)}$). Fission product nuclides with large contributions from this mode of decay have two terms in the first summation of the previous equation.

The second summation may be completely neglected because the atom densities of each individual fission product k are on the order of at most several hundred thousand atoms, the cross-section is commonly not known for short-lived fission products, and the cross-sections for threshold reactions like proton knock-out (n,p) or double neutron knock-out $(n,2n)$ are commonly on the order of a barn or milli-barns. It may be assumed that the

Figure 2.6: Neutron rich isobar chain of atomic weight 99. An example of an isobar chain where beta decay is the primary mode of atomic transition.

contributions to the production rate of a single fission fragment from exotic nuclear reactions with other fragments would be orders of magnitude smaller than the primary sources of generation (fission generation and parent nuclide decay). The equations incorporating these simplifications are provided for the two different cases of isotope generation((2.18a)–(2.18b)).

$$N_p(\vec{r},t_1) = e^{-\lambda_p t_1}\left[\int_0^{t_1} e^{\lambda_p t}\big(\lambda_j^{(\beta)} N_j(\vec{r},t) + G_p(\vec{r},t)\big)dt + N_p(\vec{r},0)\right] \tag{2.18a}$$

$$N_p(\vec{r},t_1) = e^{-\lambda_p t_1}\left[\int_0^{t_1} e^{\lambda_p t}\big(\lambda_j^{(\beta)} N_j(\vec{r},t) + \lambda_j^{(n)} N_j(\vec{r},t) + G_p(\vec{r},t)\big)dt + N_p(\vec{r},0)\right] \tag{2.18b}$$

Treating the t_1 variable as the end of irradiation (EOI) where the generation rate G_p becomes zero, the atom density $N_p(\vec{r},t_1)$ becomes the initial condition of a similar equation. The discontinuity of the generation rate during a controlled irradiation forces the solution of the time dependent atom density to be discontinuous at t_1. The atom density after the EOI may be derived from (2.15) by setting $G_p = 0$ and applying the same assumptions used to derive (2.18a)–(2.18b). The differential form of the EOI atom density is provided in (2.19a)–(2.19b).

$$\frac{\partial N_p(\vec{r},t)}{\partial t} = -\lambda_p N_p(\vec{r},t) + \lambda_j^{(\beta)} N_j(\vec{r},t) \tag{2.19a}$$

$$\frac{\partial N_p(\vec{r},t)}{\partial t} = -\lambda_p N_p(\vec{r},t) + \lambda_j^{(\beta)} N_j(\vec{r},t) + \lambda_j^{(n)} N_j(\vec{r},t) \tag{2.19b}$$

The solutions to (2.19a)–(2.19b) are (2.20a)–(2.20b).

$$N_p(\vec{r},t_2) = e^{-\lambda_p t_2}\left[\int_{t_1}^{t_2} e^{\lambda_p t}\lambda_j^{(\beta)}N_j(\vec{r},t)dt + e^{\lambda_p t_1}N_p(\vec{r},t_1)\right] \tag{2.20a}$$

$$N_p(\vec{r},t_2) = e^{-\lambda_p t_2}\left[\int_{t_1}^{t_2} e^{\lambda_p t}\left(\lambda_j^{(\beta)}N_j(\vec{r},t) + \lambda_j^{(n)}N_j(\vec{r},t)\right)dt + e^{\lambda_p t_1}N_p(\vec{r},t_1)\right] \tag{2.20b}$$

Thus far, explicit solutions to the time dependent atom densities have remained elusive. This is only a formality caused by a lack of boundary conditions and physical constraints. Referring to figure 2.6, the beta decay chain is finite. For all intents and purposes of this study, ^{99}Kr has no production rate contributions from parent isotope beta or neutron decay. The production probability of the parent isotope of ^{99}Kr is most likely non-zero, but is assumed to be nearly zero. Also, the initial sample material may be assumed to contain zero ^{99}Kr (K9) at any time before irradiation. This assumption may be justified in observing the particularly short half-life of ^{99}Kr. Therefore, equation (2.19a) simplifies to equation (2.21).

$$N_{K9}(\vec{r},t) = e^{-\lambda_{K9} t_1}\left[\int_{0}^{t_1} e^{\lambda_{K9} t}G_{K9}(\vec{r},t)dt\right] \tag{2.21}$$

The first set of experiments used high-purity sample materials composed of a single actinide isotope, ^{232}Th (T02). The half-life of this material is on the order of tens of billions of years. The microscopic fission cross-section for 14 MeV neutrons is slightly less than one barn. Also, the flux is controlled by an electronics system that monitors and sustains the deuteron beam current. The neutron output from the source does not vary drastically over time and may be assumed constant. Using these assumptions and solving for the time-

dependent atom density of ^{232}Th using(2.15) yields (2.22a)–(2.22b).

$$\frac{\partial N_{T02}(\vec{r},t)}{\partial t} = -\big(\lambda_{T02} + \langle\sigma_f^{T02}\rangle\phi(\vec{r})\big)N_{T02}(\vec{r},t) \tag{2.22a}$$

$$N_{T02}(\vec{r},t_1) = N_{T02}(\vec{r},t)e^{-\left(\lambda_{T02}+\langle\sigma_f^{T02}\rangle\phi(\vec{r})\right)t} \tag{2.22b}$$

The decay rate during irradiation is so small that it would take nominally 30,000 years of constant irradiation to lose one percent of the initial starting material. The irradiation time used in these experiments was on the order of seconds; therefore, the atom density of the target material is assumed constant (2.23).

$$N_{T02}(\vec{r},t_1) = N_{T02}(\vec{r},t)e^{-\left(\lambda_{T02}+\langle\sigma_f^{T02}\rangle\phi(\vec{r})\right)t} \approx N_{T02}(\vec{r},0) \quad \forall t < 10000a \tag{2.23}$$

Inserting (2.23) into equation (2.21) yields equation (2.24).

$$N_{K9}(\vec{r},t) = e^{-\lambda_{K9}t_1}\left[\int_0^{t_1} e^{\lambda_{K9}t}N_{T02}(\vec{r},0)\langle\sigma_f^{T02}\rangle\phi(\vec{r})dt\right] \tag{2.24}$$

The final solution for the time dependent atom density of ^{99}Kr during irradiation becomes (2.25).

$$N_{K9}(\vec{r},t_1) = N_{T02}(\vec{r},0)\langle\sigma_f^{T02}\rangle\phi(\vec{r})\frac{1-e^{\lambda_{K9}t_1}}{\lambda_{K9}} \tag{2.25}$$

The post-irradiation atom density may be determined using (2.20a) and the results of (2.25). The post-irradiation atom density of ^{99}Kr is (2.26).

$$N_{K9}(\vec{r},t_2) = e^{-\lambda_{K9}t_2}\left[N_{T02}(\vec{r},0)\langle\sigma_f^{T02}\rangle\phi(\vec{r})\frac{1-e^{\lambda_{K9}t_1}}{\lambda_{K9}}\right] \tag{2.26}$$

The process of searching for the decay shape of more complex decay schemes like ^{99}Zr can easily be continued from equations (2.25) and (2.26). The last and final simplification to the above equation is focused on the microscopic cross-section (2.14b). Because the source is a fusion neutron generator, the flux energy distribution is strongly peaked around 14 MeV. Also, the fission cross-section and yield fraction terms on the left-hand side of (2.14b) do not vary drastically around this energy. Therefore, both the cross-section and the yield factor may be approximated as constants. Applying this approximation to (2.14b) yields (2.27).

$$\langle\sigma_i^p(\vec{r},t)\rangle = \frac{\int_0^\infty \sigma_i(\mathbf{E})Y_i^{(p)}(\mathbf{E})\varphi(\vec{r},\mathbf{E},t)d\mathbf{E}}{\int_0^\infty \varphi(\vec{r},\mathbf{E},t)d\mathbf{E}} \approx \sigma_i Y_i^{(p)} \tag{2.27}$$

The final solution to the time dependent atom density of ^{99}Kr is (2.28).

$$N_{K9}(\vec{r},t) = \begin{cases} N_{T02}(\vec{r},0)\langle\sigma_f^{T02}\rangle\phi(\vec{r})\frac{1-e^{\lambda_{K9}t_1}}{\lambda_{K9}} & t_1 \geq t \geq 0 \\ e^{-\lambda_{K9}t_2}\left[N_{T02}(\vec{r},0)\langle\sigma_f^{T02}\rangle\phi(\vec{r})\frac{1-e^{\lambda_{K9}t_1}}{\lambda_{K9}}\right] & t \geq t_1 \end{cases} \tag{2.28}$$

All of the assumptions used to derive the expected decay schemes for the isotopes along isobars are listed in table 2.1.

2.4 Closing

Thus far, a history of nuclear forensics and the difficulties associated with it, neutron activation analysis and coincident gamma-spectroscopy, and models of radioactive decay and radiation detection have been presented. These methods are the foundations of the method used in the experiments conducted for this dissertation. Both the gamma-ray singles and

	Assumptions
1	There are only two dominant forms of fission product decay: (1) beta, and (2) neutron emission.
2	Exotic nuclide production and loss reactions like (n, p) and $(n, 2n)$ are negligibly small in comparison to the primary production and loss mechanisms, fission and radioactive decay.
3	Parent nuclides along isobars not listed in the Chart of the Nuclides have half-lives that are negligibly small, their decay into the daughter may be treated as instantaneous.
4	The target material is well characterized and impurities with detrimental effects to the measurements are negligible.
5	The starting target material inventory does not include any fission products.
6	The neutron source is stable over short irradiation times and may be approximated as time independent.
7	The neutron source energy distribution is peaked at the deuterium-tritium fusion energy and the fission cross-section and energy dependent yield factors may be approximated as constant at this energy.

Table 2.1: A list of assumptions used to derive the time-dependent atom density of the fission fragments.

coincident data were acquired simultaneously using advanced electronics equipment while performing multiple controlled sample irradiations to preferentially saturate the activity of fission products with half-lives on the order of seconds. An introduction to the facility and experimental validation of the pneumatic system and detection equipment is provided in the next chapter.

CHAPTER III

Pneumatic System Testing

3.1 Introduction

The University of Michigan Neutron Science Laboratory (UofM-NSL) was selected as an ideal location to perform 14 MeV fission yield studies because of the already in place pneumatic system and largest commercially available fusion neutron source. However, this facility was originally designed to perform single sample irradiations followed by counting. This approach has been used in the past to measure fission products with minute to hour half-lives but would not be useful in observing short-lived fission products. To retain the current infrastructure and to avoid costly modifications to the facility, the cyclic neutron activation analysis approach was selected. The primary alternative to cyclic neutron activation analysis would have been to redesign the facility to use the gas-jet technique. This would have required a complete facility overhaul and lengthy revisions to the Nuclear Regulatory Commission licensing to accomplish installation of such a system.

Several modifications were needed to prepare the UofM-NSL facility for cyclic sample activation. First, the pneumatic system tubing was modified to minimize the sample transit distance and number of tubing bends. This was accomplished by rerouting the system to transfer samples directly from the irradiation enclosure to the installed detection system. Figure 3.1 illustrates how the system was modified to accommodate this change. Second, the control system software and hardware was modified to automate the cyclic irradiation

of samples and to provide sample transfer timing information. A programming "for" loop was added to the control system software. This loop took input from the system user to define the irradiation and count time of each cycle and how many cycles to perform before stopping. The hardware modification involved replacing an analog-to-digital voltage monitor that recorded the voltage output from two infrared optical sensors. These optical sensors were placed at each end of the pneumatic system; one near the end of the tubing inside the irradiation enclosure and the other just above the counting end station. The original ADC operated at a 10 sample per second rate. This sampling rate was far below the total time (approximately 10 milliseconds) it took the rabbit capsule to cross the infrared beam of the optical sensors. The original ADC commonly failed to record the voltage change from the optical sensors produced by the pneumatic capsule. It was replaced with a new ADC with a 10000 sample per second rate and the control system was reprogrammed to both use the ADC to keep track of the position of the sample and to record the irradiation time, sample transit times to and from the generator and detector, and count timing with 100 microsecond precision.

This facility was comprised of a Thermo-Scientific D711 accelerator based deuterium-tritium (D-T) fusion neutron generator, a pneumatic transfer system, and a lead shielded box with four ports: one small vertical port at the top for the pneumatically transferred target, and three other ports, one on bottom and two along a set of parallel sides, for three high-purity germanium detectors.

The NSL facility was modified to measure fission product half-lives, gamma-ray branching ratios, and independent/cumulative fission yields with half-lives as short as a half second. Before embarking on costly, time consuming work and contaminating high-quality actinide foils, it was necessary to test the NSL facility using a benchmark.

Lithium-carbonate(Li_2CO_3), heat sealed in polyethylene, was cyclically irradiated to produce nitrogen-16 (^{16}N) from the $^{16}O(n, p)^{16}N$ reaction and gamma-rays emitted from the activated target were used to measure the stability of the radiation detectors, repeatability

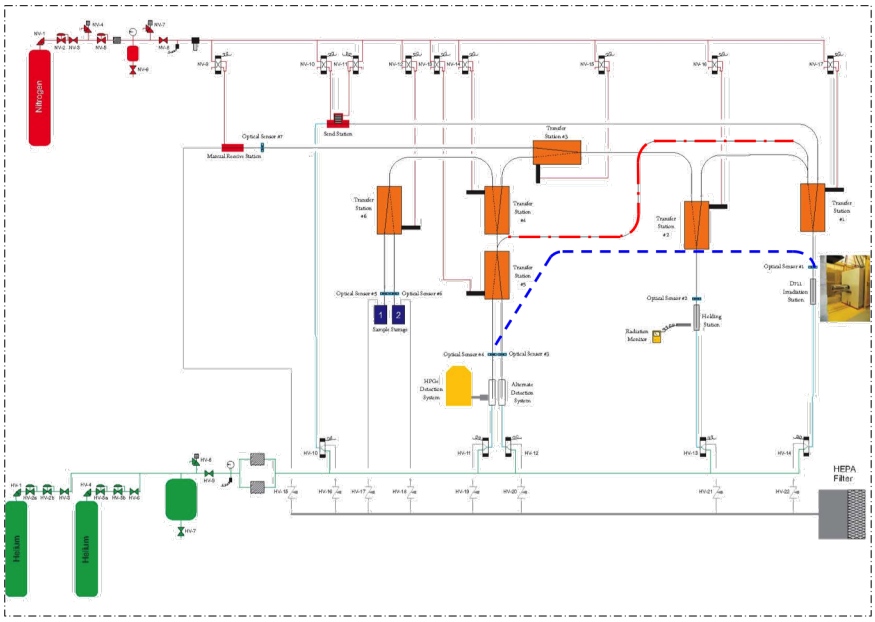

Figure 3.1: Original and adjusted pneumatic system. The red and blue dashed lines indicate adjustments that were made to simplify the original pneumatic system in the summers of 2013 and 2015, respectively.

of the pneumatic system, and cycle-to-cycle variability in the neutron generator output. ^{16}N was selected because the length of the half-life is comparable to that of many of the fission products the NSL facility has been developed to measure (7.108 seconds), sample material ideal for generating a mono-isotopic gamma-ray spectrum was readily available, and the half-life measurement would resolve any concern regarding measurement bias from background interference in previous measurements listed in the nuclear data sheets [126, 127]. Results of this work quantified sources of systematic variability from the NSL equipment, contributed to the measurement of ^{16}N, and provided a foundation to qualify the capabilities of the NSL facility in support of nuclear forensics research.

Prior to the four experiments performed from 1964 to 1970 used to calculate the currently published half-life value of ^{16}N, the half-life was consistently measured to be 3% higher [126]. The third publication of the four published from 1964 to 1970 [128] lead the authors to conclude that there were, potentially, additional sources of background activation by-product that had biased the results of all measurements before 1966. This discrepancy has

yet to be resolved. The half-life on the order of seconds and opportunity to resolve a historic question regarding bias made the examination of the half-life of ^{16}N an ideal candidate for benchmarking the performance of the NSL facility.

3.2 Experiment

A mass of 0.47 grams of Li_2CO_3 powder was compressed inside a volume of 0.03 cubic inches and heat sealed inside a polyethylene target using a hand vice and ceramic inductively heated oven. The target was composed of two separate parts: (1) a cylindrical body with a bulletized cavity and (2) a plug. Li_2CO_3 powder was added to the internal encapsulation body and the plug was inserted into the top of the capsule. Once the target had been weighed, it was placed inside the steel press shown in figure 3.2 and the vice was tightened by hand and placed in an oven at 140°C for three hours. After heat treatment, the target was removed from the furnace and left to cool in air before removal from the press and installation in a pneumatic capsule shown in figure 3.3.

The FIRST capsule containing the target was loaded into the FIRST detector end station and armed by opening the compressed gas cylinders. Helium gas (99.5% purity) was used as the flow gas to move the capsule through the pneumatic system. Helium was selected to minimize ejection of activated air into the lead box from the end station and increasing the number of external nitrogen-16 decay counts.

Once the FIRST capsule was loaded, the D711 Thermo-Scientific D-T neutron generator was brought to power at standard operating conditions of 160 kV accelerating potential and 1.5 mA current of deuterons. A ten minute background count of the sample was taken from all three detectors once the generator's output had reached stability. After verifying there were no peaks in the high-energy region that would interfere with the full energy, single, and/or double escape peaks of the 6128 keV gamma-ray line of ^{16}N, the pneumatic system and DSPEC Pro multichannel analyzers were prepared for the CNAA experiment.

The control software monitors two control system components: an ADAM module (M#

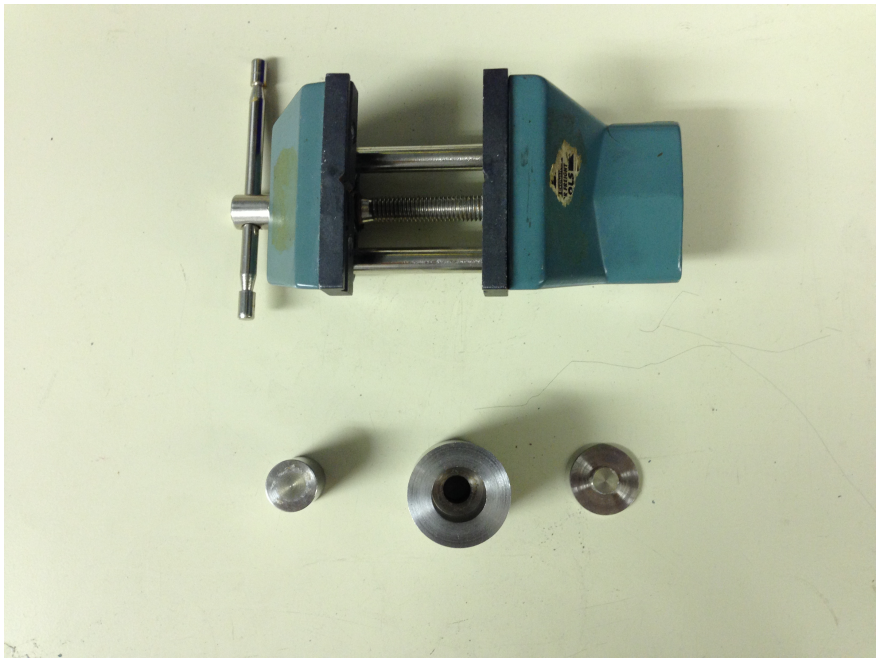

Figure 3.2: Steel press used to heat seal the capsule. The press was composed of an anvil (left) body (center) and cap (right). The hand vice displayed at the top of the photo was used to hold the anvil and cap in place while the sample was heated in an induction coil ceramic oven.

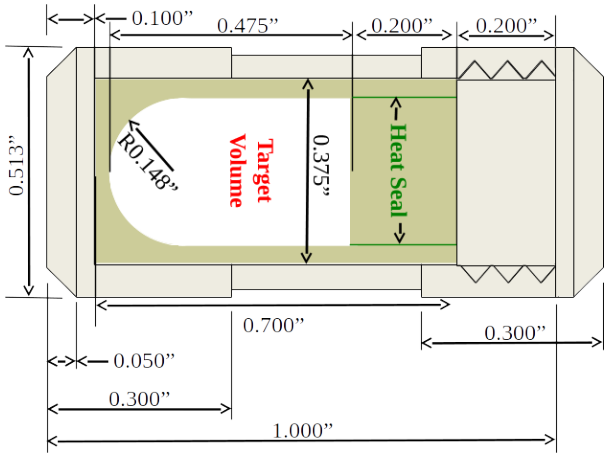

Figure 3.3: Internal target (darker shade) and FIRST capsule used to cyclically irradiate the target material. Final dimensions of the FIRST capsule and internal target were all within 0.01” of the listed dimensions. The end closest to the target volume was the end nearest the generator during irradiations and vice versa during counting.

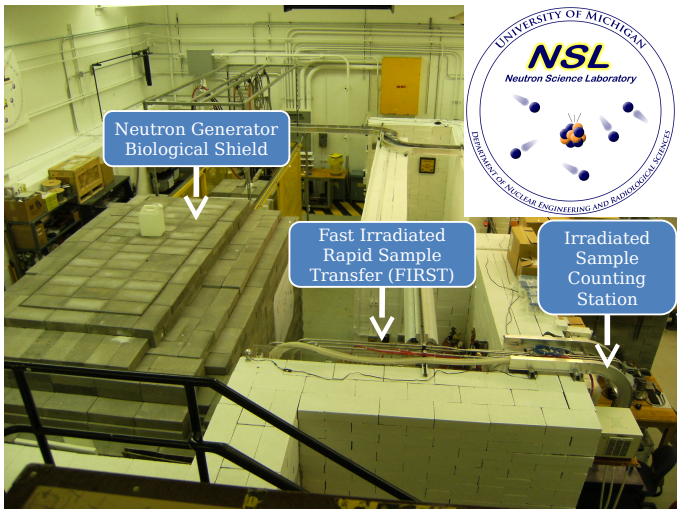

Figure 3.4: Photograph of the University of Michigan's Neutron Science Laboratory facility. The pneumatic system tubing, generator shielding, and detection end station are visible.

ADAM-4522) which actuates the helium control valves, and an analog-to-digital voltage monitor from National Instruments (NI) (M# USB-6008). The voltage monitor was directly connected to two laser optical sensors. One optical sensor was located 13.25" from the neutron generator inside the generator enclosure, the second was located 31.5" above the pneumatic end station sitting above the radiation detector. An annotated photograph of the facility is provided in figure 3.4.

Timing data for each cycle were recorded in a text file starting with a clock formatted time-stamp representing the moment the helium valve was opened. This time stamp was followed by three additional values: (1) the transit time to the generator, (2) transit time from the generator, and (3) the irradiation time. Timing uncertainty in the pneumatic system were all assumed to be 0.1 milliseconds based on the NI voltage monitor sample rate.

Three HPGe detectors were used to acquire data from the irradiated sample. Figure 3.5 is a photograph of the HPGe detectors with the end station sitting above the vertical detector (vert). Each detector was connected to a separate DSPEC Pro data acquisition system operating in list-mode [129]. List-mode acquisition is characterized as a list of time-stamped channel numbers. The real-time clock value was reported to an accuracy of 200-nanosecond

from the start of acquisition. Every 10 milliseconds (when the real-time clock rolled over 50000), an additional set of information was written to the buffer: (1) a 30-bit integer value indicating the number of times the real-time clock had rolled over since start of acquisition, (2) a second 30-bit integer value indicating the number of times the live-time clock had rolled over, (3) the value of the real-time clock at the moment the fourth value was written to the buffer, and (4) the clock value recorded by the computer on receiving the buffer data from the DSPEC Pro. Using the computer generated clock value and the difference between the recorded time-stamp value of each event and the third value indicating the position of the real-time clock within the DSPEC Pro, the moment of each count was correlated to the time of acquisition with an accuracy of 200 nanoseconds. Variation in the clock response within the computer acquiring data was found to be much higher than the resolution of the internal clock of the DSPEC Pro. After examining the clock response within the data acquisition computer the maximum accuracy of the individual events was found to be comparable to the 0.1 millisecond resolution of the NI instrument.

The irradiation time was set to 25 seconds, the count time to 95 seconds, and the number of cycles to 50 in the control software. The irradiation time was selected to exceed 90% saturation of the ^{16}N activation product. The count time was selected to limit the residual ^{16}N activity upon re-irradiation to below 0.01%. Additional cycles beyond 50 could have been performed; however, wear on the capsule increased the the transit time beyond the 500 millisecond threshold. After list-mode data acquisition was stopped from all three germanium detectors, an additional count of the sample was taken. The final count was made to ensure no activation contaminants were present in the high-energy region around the ^{16}N 6.1 and 7.1 MeV gamma-ray emissions. No activation contaminants were observed after 20 minutes of counting post irradiation.

Figure 3.5: HPGe detectors in the lead shield used to acquire data from the experiment. The end station tubing enters through a small hole between the sliding lead doors. Within the lead box are three detectors. Two of the detectors lie roughly along the two cardinal directions and are aptly named east (left in photo) and west. The third detector, named vert, is coupled to the end station using an acrylic spacer. The neutron generator lies several feet north of the detectors behind 2 inches of polyethylene, six feet of concrete, 2 inches of borated polyethylene, 4 inches of lead, and an 1/8" of copper.

3.3 Data and Analysis

List-mode data acquired from a DSPEC Pro consist of a list of channel numbers and time-stamps accurate to 0.1 milliseconds with live-time clock values reported every 10 milliseconds. Timing information from the pneumatic system was used to find one event for each cycle within the list of recorded channel numbers closest to the time when the sample was returned to the detectors. The first event of each cycle was used to parse the next 95 seconds of count data into 190 500 millisecond spectra. Microphonic vibrations from helium passing through the detector end station produced spurious counts in the detectors. To avoid contaminating the measurement results, the first 500 millisecond spectrum was ignored. As mentioned in the experimental section, the list-mode data stream is effectively a continouos stream of channel values and time-stamps interspersed with header outputs that include the live-time clock. To calculate the various parameters used to examine the repeatability of the NSL facility, several parameters were needed from the data stream in addition to the counting spectra. These parameters were: count-rate, live-time, and real-time. Real-time was calculated by evaluating the difference between the time-stamps of the last and first count recorded in the spectrum. Live-time was measured by evaluating the difference between the last and first header outputs from the data stream within the range of the last and first recorded count and dead-time was simply the difference between these values. Real-time and live-time were recorded for each spectrum from each cycle. While evaluating the half-life of ^{16}N, the spectra from each cycle were combined. Real-time, live-time, and count-rate for the final summed set of spectra had to be carefully tabulated for the dead-time and pile-up count-loss corrections. The real-time and live-time were summed together as the spectra were combined and the total sum of counts divided by the sum of live-times was used as the average count-rate in all three HPGe detectors. The dead-time, however, could not simply be the difference in the summed real-time and live-time. The difference in summed real-time and live-time had to be averaged over the number of cycles to produce a dead-time that

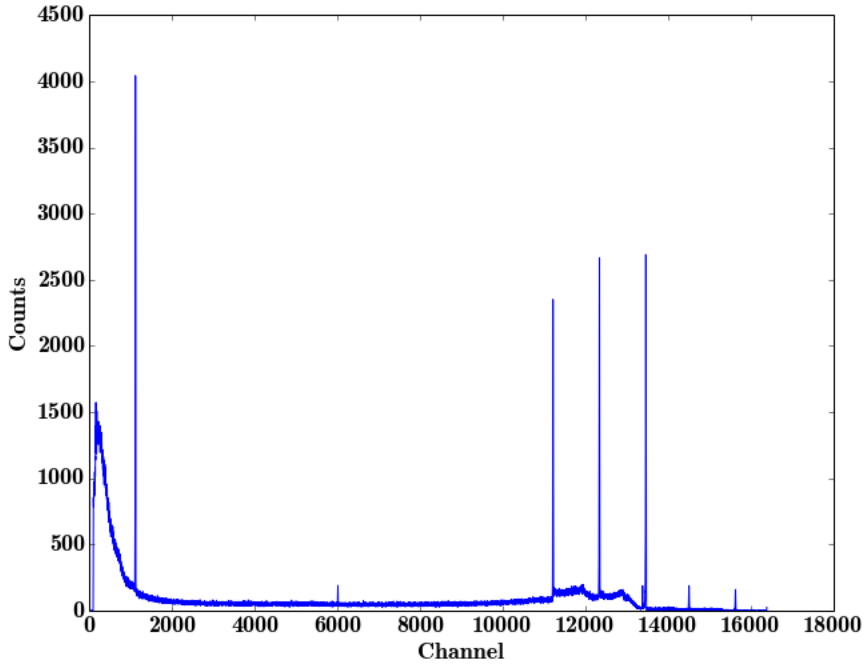

Figure 3.6: Gamma-ray spectrum acquired from the west detector 0.5 seconds to 50 seconds after irradiation. The full-energy, single and double escape peaks of the 7.1 and 6.1 MeV, the 2741 keV, and the 511 keV gamma-ray lines are visible scanning the spectrum from right to left.

accurately reflected the average dead-time of each 500 millisecond timeslice.

The first two results examined were the variability in detector response induced by variations in sample positioning and generator intensity. These affects were examined using the total number of counts measured from each detector during the first 50 seconds of counting. Figure 3.6 is the spectrum acquired from 0.5 seconds to 50 seconds after irradiation from detector west. The third result examined the variation in irradiation and transit timing of the pneumatic capsule from timing information. These results were assumed to be normally distributed about a mean and the standard deviation was calculated as the square-root of the sum of squared differences between the mean and measured values divided by the square-root of the number of cycles minus one.

The fourth result examined was the half-life of ^{16}N. Data acquired during the first 75 seconds, over ten half-lives of ^{16}N, were used to make this measurement. This result was determined after selecting three regions of interest (ROI) spanning the channel ranges under

the full energy, single, and double escape peaks of the 6128 keV gamma-ray line. The sum of counts in the specified ROIs were recorded from each 500 millisecond long spectrum and summed together across cycles to produce one set of 149 peak area sums for fitting. The half-life was measured using a linearized χ^2 minimization technique [130, 131]. The value of the half-life was varied from 4 seconds to 9 seconds in 0.001 second increments. For each 500 millisecond spectrum, the sum of peak areas was corrected for dead-time and pulse pile-up using a predefined value of the half-life using equation (3.1) where C_i' is the corrected peak area, C_i is the uncorrected peak area, $\lambda = \ln(2)/T_{1/2}$ is the decay constant, LT was the average live-time recorded from the set of summed spectra spanning the set of cycles, DT was the average dead-time, α was the pile-up rejection constant (400 nanoseconds), and CR was the total sum of counts from all of the spectra divided by the sum of live-times, or average count-rate.

$$C_i' = \frac{C_i}{1 - e^{-\lambda LT}} \cdot \frac{e^{\lambda DT} - 1}{\lambda DT} \cdot e^{\alpha \cdot CR} \tag{3.1}$$

After correcting for decay during counting, dead-time, and pulse pile-up, the peak areas were applied to equation (3.2) where A is a scaling constant that normalizes the exponential curve to fit the data and λ contains the value of the half-life.

$$C_i' = A \cdot e^{-\lambda t_i} \tag{3.2}$$

The scaling constant (A) was determined for each increment of the half-life using equation (3.3). Once the scaling constant was determined, the χ^2 value was measured for the pre-defined half-life value using equation (3.4).

$$A = \frac{\sum_{i=1}^{149} \frac{C_i' \cdot e^{-\lambda t_i}}{\sigma_{C_i'}^2}}{\sum_{i=1}^{149} \frac{2 \cdot e^{-\lambda t_i}}{\sigma_{C_i'}^2}} \tag{3.3}$$

$$\chi^2 = \sum_{i=1}^{149} \frac{(C_i' - A \cdot e^{-\lambda t_i})^2}{\sigma_{C_i'}^2} \tag{3.4}$$

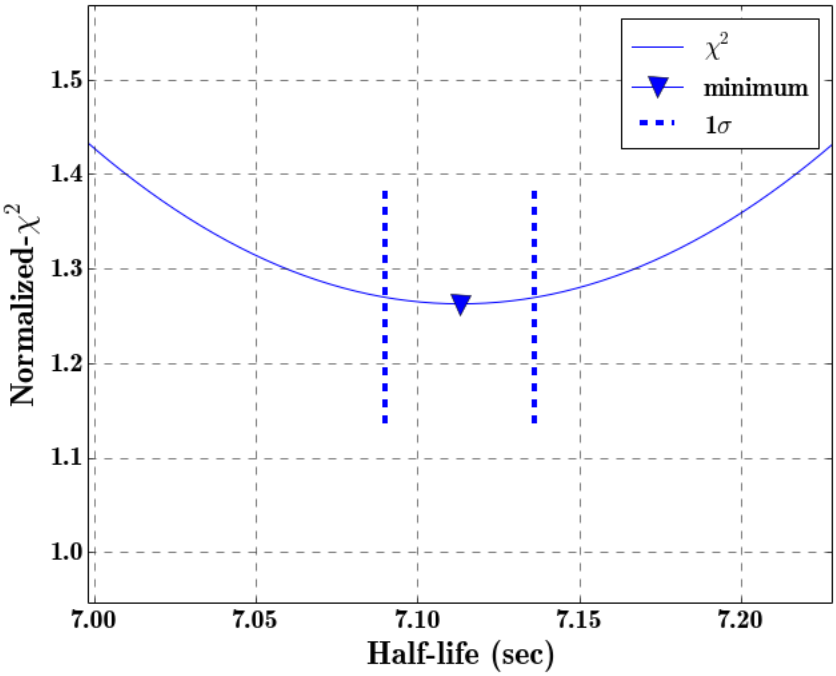

Figure 3.7: Normalized-χ^2 parabola for the half-life measurement produced from data acquired from the west detector.

The calculation of normalized-χ^2 was repeated for each subsequent value of the half-life to map a parabola in normalized-χ^2 space as shown in figure 3.7. The ordinate associated with the minimum is the best estimate of the half-life and the ordinate associated with the minimum normalized-χ^2 value plus one divided by the difference of the number of degrees of freedom minus the number of free parameters is the uncertainty.

3.4 Results & Discussion

The primary objective of this experiment was to examine the systematic variability in the CNAA system. The first possible source of variability examined was the positioning of the target upon return from irradiation. This was measured by comparing the ratio of the total sum of counts measured from 0.5 to 50 seconds between the three detectors. Provided the sample returned to the same place each time, the ratio of the total counts spanning the same counting period for each detector ratio should be constant regardless of the neutron generator's intensity.

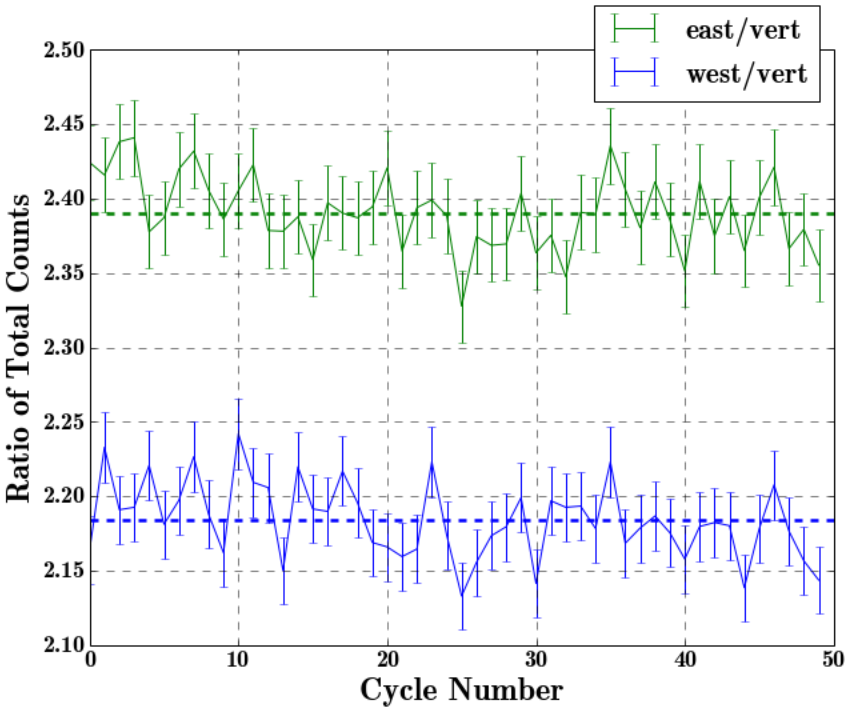

Figure 3.8: Ratio of total counts measured from 0.5 to 50 seconds from each cycle between detectors east and west to detector vert. The target was roughly centered between east and west. The averages for each set are plotted as dotted lines.

The measured ratios as a function of cycle are presented in figure 3.8, and table 3.1 provides the mean and standard deviation calculated using inverse-variance weighting and the normalized-χ^2 values. The uncertainty was measured as the square-root of the total number of counts. Figure 3.8 illustrates that the variability associated with the counting geometry along the vertical axis relative to the horizontal axis is insignificant. The large normalized-χ^2 value measured from the ratio of counts from the two horizontal detectors indicates there is additional variation in the target position that affects the statistical precision of the ratio beyond the standard Poisson statistical analysis. This additional variation is likely caused by the mismatch in the outer diameter (0.53") of pneumatic capsule and the inner diameter of the pneumatic system tubing (0.51") of 0.02". Nevertheless, the sample positioning was determined to be repeatable, but exhibited additional random variation in the horizontal positioning. The impact on the statistical certainty of the measurement can be estimated from the square-root of normalized-χ^2 minus one; thus, a normalized-χ^2 of 1.793 indicates

Detector Ratio	Mean (1-σ)	Normalized-χ^2
west/vert	2.1836(33)	1.160
east/vert	2.3905(35)	0.9779
west/east	0.9133(11)	1.793

Table 3.1: Mean, standard deviation, and normalized-χ^2 values for each measured ratio using only Poisson statistics.

Detector	Mean (1-σ)	Normalized-χ^2
east	31469(25)	2.807
west	28746(35)	2.787
vert	13162(16)	0.854

Table 3.2: Total counts measured 0.5 to 50 seconds after irradiation for each cycle.

that the standard deviation is roughly 34% larger than the estimate produced using only Poisson statistics.

After estimating the statistical impact of the counting geometry, the total measured counts were examined cycle-by-cycle to measure the variation relative to the inverse-variance weighted mean. The total number of counts from both horizontal detectors measured from 0.5 to 50 seconds after sample return are provided in figure 3.9. The large normalized-χ^2 values from table 3.2 for the two horizontal detectors is a combination of the observed variation in the horizontal positioning of the target and generator intensity. The estimated increase in standard deviation needed to achieve a normalized-χ^2 equivalent to one was 67%. Using this estimate and the previous estimate, added variation from generator intensity is roughly equivalent to variation induced by target positioning.

The next source of variation examined was the transit and irradiation timing. Figures 3.10 and 3.11 are the irradiation time and the transit times between optical sensors observed from each cycle using the ADC. The irradiation timing has been shown to be highly repeatable (see figure 3.10). The standard deviation was measured to be less than one millisecond and is assumed to have had a negligible impact on the activation process.

Figure 3.11 illustrates the transit time from the generator to the detector is slightly slower and variable than transit to the generator. A likely explanation for why this occurs

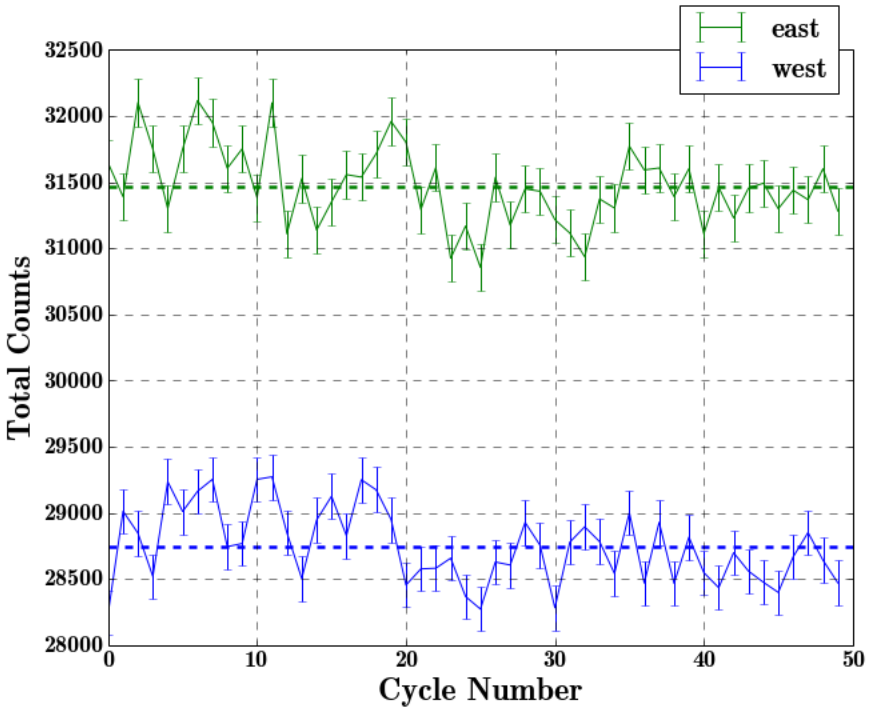

Figure 3.9: Total counts measured from the two horizontal HPGe detectors during the period 0.5 to 50 seconds after irradiation for each cycle. The averages for each set are plotted as dotted lines.

can be inferred from figure 3.3. Because the center-of-mass of the pneumatic capsule is skewed away from the heat sealed end of the internal encapsulation, the capsule travels more naturally through the tubing when moving toward the generator, but during return it rattles through the tubing as the capsule attempts to rotate about the axis perpendicular to the capsule's cylindrical axis. The additional frictional losses along the walls of the FIRST system tubing result in additional variation and a slight delay in the return time from the generator. In addition to a delay transit from the generator, there is one cycle with a transit time nearly twice the peak of the distribution in figure 3.11. The last cycle's return time exceeded 400 milliseconds. During pneumatic system testing, it has been observed that wear on the capsules from multiple cycles rounds and tapers the ends of the pneumatic capsule decreasing the outer diameter of the capsule. From experience, a FIRST capsule lifetime should be limited to at most 50 cycles before replacing it. Finally, the half-life was measured from each detector by adding subsequent cycles together. The final results

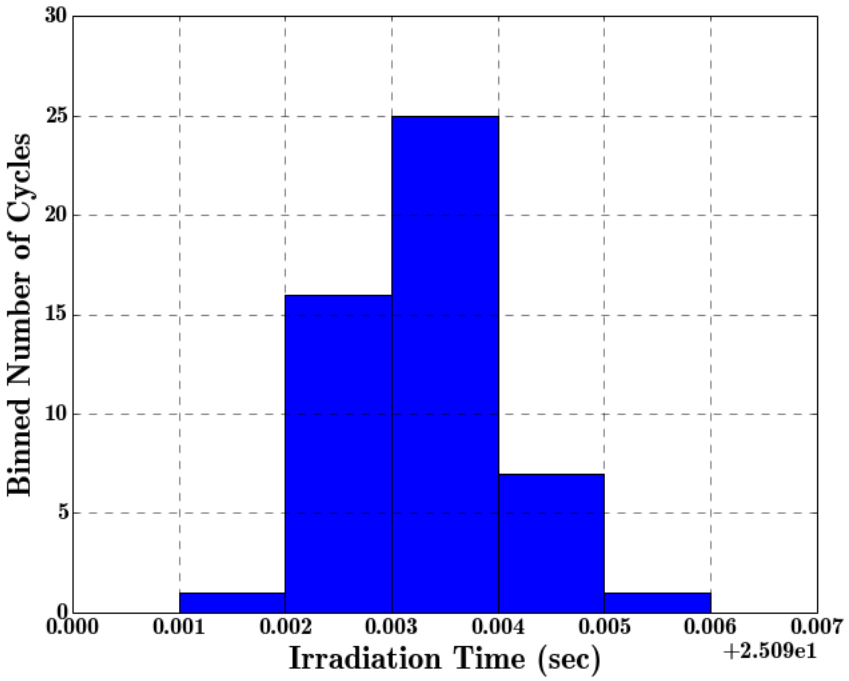

Figure 3.10: Irradiation time measured using the optical sensors relative to the 25 second time set by the control software.

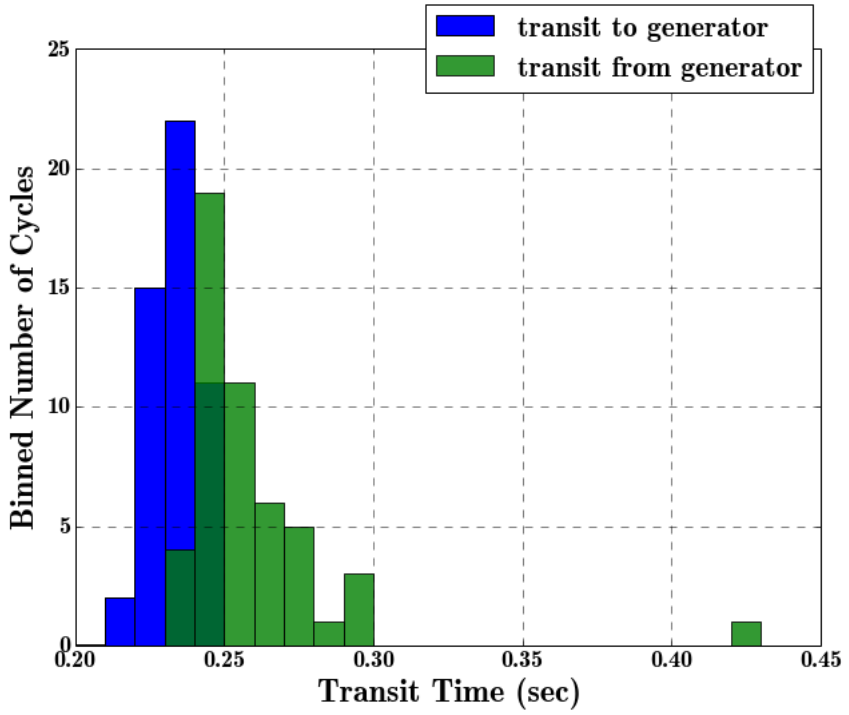

Figure 3.11: Measured transit time to and from the neutron generator.

Detector	Half-life (sec)	1-σ (sec)	Normalized-χ^2	Residual R^2
west	7.113	0.023	1.263	0.9993
east	7.092	0.022	1.022	0.9996
vert	7.147	0.039	1.272	0.9981

Table 3.3: Measured half-life results from each detector acquired from 40 seconds of counting using a 1 second delay and 0.5 second counting bins.

Citation	Half-life (sec)	1-σ (sec)
[132]	7.14	0.02
[133]	7.16	0.04
[128]	7.10	0.03
[134]	7.13	0.04

Table 3.4: Historical half-life results and associated works.

from each detector, provided in table 3.3, were combined using inverse-variance weighting to produce the following estimate: 7.108(15) seconds. In contrast to the references in the Nuclear Data Sheets provided in table 3.4, this value was not determined using a single channel analyzer summing counts above a predefined threshold. Rather, this measurement was determined by summing the counts from the full energy, single, and double escape peaks of the 6128 keV gamma-ray line and is not affected by any additional sources of activity in the high-energy region of the spectra. This fact coupled with the negligible background count-rate in the ROIs suggests the final estimate agrees well with the previous measurements available from the Nuclear Data Sheets and affirms their result are not statistically precise enough to be sensistive to small, minor variations in background.

3.5 Closing

The UofM-NSL has successfully examined the systematic uncertainties of the various mechanical components that comprise the CNAA system. The counting geometry was found to have negligible variation in the vertical direction, but exhibited appreciable variation in the horizontal direction due to the larger inner diameter of the pneumatic tubing relative to the outer diameter of the rabbit capsule. The systematic uncertainty between cycles was

estimated to increase the standard deviation of the Poisson statistics by 34%.

In addition to the increased variation resulting from random variation of the capsule position in the horizontal direction, variation in the neutron generator's output was estimated to increase the standard deviation of the Poisson statistcs by an additional 33%. The transit timing and repeatability of the irradiation time was also examined and found to have a negligible impact on the systematic variation relative to variation in sample positioning and generator output. Gain stability of the radiation detectors was found to be only slightly larger than the Poisson statistical certainty of the centroid and the measured half-life from each detector for ^{16}N agreed with the published values. The final value measured by combining the results from each detector using inverse-variance weighting was 7.108(15) seconds; thus, verifying the past four published measurements.

CHAPTER IV

Detector & Generator Characterization

4.1 Introduction

After characterizing and quantifying systematic uncertainties inherent to the pneumatic system, an experiment was designed to expand the capabilities of the three-crystal detection system to include gamma-gamma coincidence. Two significant adjustments were made to the detection system: 1) a new data acquisition (DAQ) system on loan from Pacific Northwest National Laboratory was installed and 2) an aluminum centering jig was installed to maintain a repeatable counting geometry for the three crystals. With these two adjustments, it was necessary to re-characterize the detector response and optimize the new capability of gamma-gamma coincidence afforded by the new DAQ. After optimizing the new DAQ equipment for the detection system, a set of activation targets were irradiated using the pneumatic system and neutron generator to characterize the neutron flux-energy distribution using both MCNP6 and STAYSL PNNL [135, 100]. Historically, neutron induced fission yield measurements have not included detailed characterization of the neutron source spectrum [136, 137, 51]. More recent studies have highlighted how crucial it is to understand and fully characterize the neutron source used for these types of measurements [138, 139, 140]. The lack of neutron flux characterization in previous fission yield studies limits the sensitivity of systematic interpolation methods for energy dependent fission yield predictions [141]. One example of this limitation is most clearly presented in the 1993 fission yield review by

England and Rider where fission yield information from each actinide was related to one of three crude neutron energy spectra labeled either thermal, fast, or 14 MeV [124]. More recent reviews have not explicitly segregated fission yield studies into the same simplified three group structure, but have treated each study independently, drawing theoretical model comparisons for individual experiments [141]. Neutron energy spectra for the three labels are approximately known but can vary significantly between facilities. Measurements predating the 1980s of 14 MeV fission yield measurements have not regularly used spectral- adjustment neutron dosimetry tools, like STAYSL PNNL [100], or full Monte Carlo neutron simulations to characterize the neutron energy distribution [135, 142]. The impact of neutron thermalization on 14 MeV neutron induced fission yield studies is important because of the slowing down and room return of neutrons scattering within the facility. The contribution of thermal and epithermal fission to the total fission for fissionable isotopes like thorium-232 and uranium-238 is small. However, for fissile isotopes, isotopes of interest to nuclear forensics, with thermal and epithermal fission cross-sections three or four orders of magnitude larger than their 14 MeV fission cross-section, the fission rate contribution from scattered neutrons becomes order of a percent or, in some cases order 10% of the total fission rate. Neglecting to characterize the source neutron spectrum limits the ability of reviewers to deconvolve the contribution to the fission yield distribution from down-scattered neutrons or at the very least provide a better estimate of the fission cross-section weighted average neutron energy such that experiments are no longer binned in a simple three bin energy structure as they were in England and Rider's review [124].

4.2 Background

Neutron source characterization is a challenging process. The most common and precise means of estimating the neutron energy spectrum has been to use time-of-flight techniques. Since the time-of-flight technique is not applicable to irradiations where the target and source are in close proximity, an alternative method was needed. The alternative to time-

of-flight used in this work was to irradiate materials with well-known energy-dependent activation cross-sections and then deconvolve the neutron spectrum using linear least squares to adjust an estimate of the neutron energy spectrum generated from MCNP6 to minimize the chi-square of the difference between the measured reaction rate and the one predicted using the simulated neutron source of each reaction from the activation targets [100, 143]. STAYSL PNNL is a software package designed to perform this linear least squares process and propagate the uncertainty estimates of the neutron energy spectrum and reaction cross-sections. In addition to providing the best estimate of the neutron spectrum, based on the simulation output, STAYSL PNNL provides a calculation of the energy-integrated product of the source flux and fission cross-section, and covariance matrices for the flux and cross-sections i.e. an estimate of the fission rate, for thorium-232, uranium-238, and uranium-235 and the means to carefully evaluate their uncertainty. A comparison of hand-calculations of the fission rate to that reported from STAYSL PNNL is presented to illustrate the large difference in predicted fission rates with and without accounting for neutron down scatter for actinides with large thermal fission cross-sections. In analyzing the short-lived fission product data, there are several sources of error. These sources of error in order of largest to smallest are the: total number of fissions, gamma-ray self-shielding correction factor, detection efficiency, dead-time and pulse pile-up correction factors, sample mass, cycling correction factor, gamma-ray branching ratios, irradiation time, and isotope half-life. This papers focus is to illustrate the reliability of this new fission product analysis system while also identifying the uncertainty in the efficiency and total number of fissions.

4.3 Experiment

A gamma-gamma coincidence detector was constructed for this experimental campaign and characterized using a multi-gamma standard and the Monte Carlo simulation toolkit, GEANT4, provided by CERN [142]. The system was used to acquire data from four activation targets that were irradiated to characterize the neutron energy spectrum. The contribu-

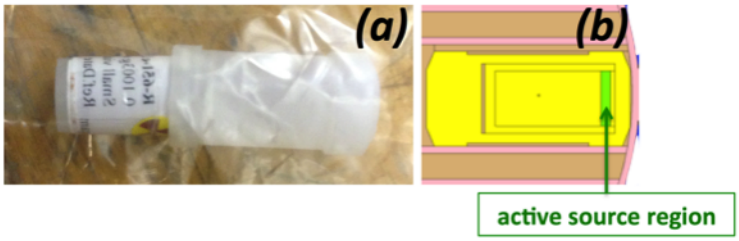

Figure 4.1: (a) Calibration standard r-651-c13 and the pneumatic capsule shell and (b) MCNP6 CAD rendering of complete capsule in the irradiation end station.

tion from thermal and epithermal neutron induced fission to the fission rate of each actinide target were estimated using STAYSL PNNL neutron dosimetry and MCNP6 neutron simulation software. A detailed example of a similar source characterization is provided in [143]. The work performed at UofM-NSL involved the use of a pneumatic transfer system to shuttle polyethylene capsules containing samples to be activated between a gamma-ray spectrometer composed of three high-purity germanium (HPGe) detectors and a D711 Thermo-Scientific accelerator driven deuterium-tritium fusion neutron generator. A photo of a polyethylene rabbit capsule and the calibration standard used for this work are presented in figure 4.1a, figure 4.1b is a CAD rendered cross-section of the capsule inside the irradiation end-station. The internal and external capsules were designed as separate pieces to allow for more cyclic irradiations by replacing worn external rabbit capsules as needed. Rabbit capsules were irradiated such that the active sample region was placed closest to the generator head as shown in figure 4.2a, figure 4.2b and c present photos of the generator and irradiation end station.

The three-crystal spectrometer was modeled using GEANT4 to estimate the full-energy peak and total efficiency as a function of incident gamma-ray energy and to estimate the impact of angular correlation on the measured coincidences. Figure 4.3a is a GEANT4 CAD rendering of the three-crystal spectrometer and figure 4.3b is a photo of it inside the shielded enclosure. Capsules were counted with the center of the active source region placed 63.5 millimeters from the face of each detector can.

Calibration standard r-651-c13 from PNNL was delivered to the UofM-NSL along with

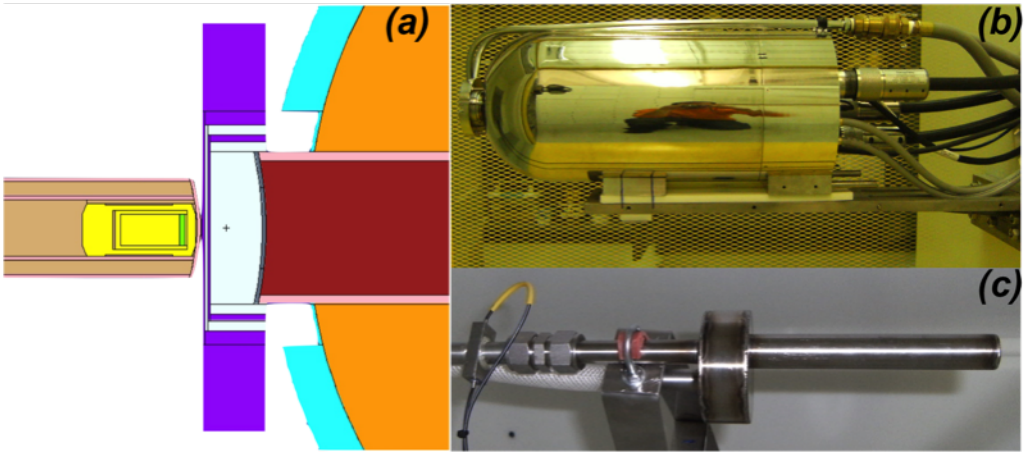

Figure 4.2: (a) CAD rendering of the generator and end station from MCNP6, photos of (b) the Thermo-Scientific D711 deuterium-tritium fusion neutron generator and (c) the irradiated sample end station.

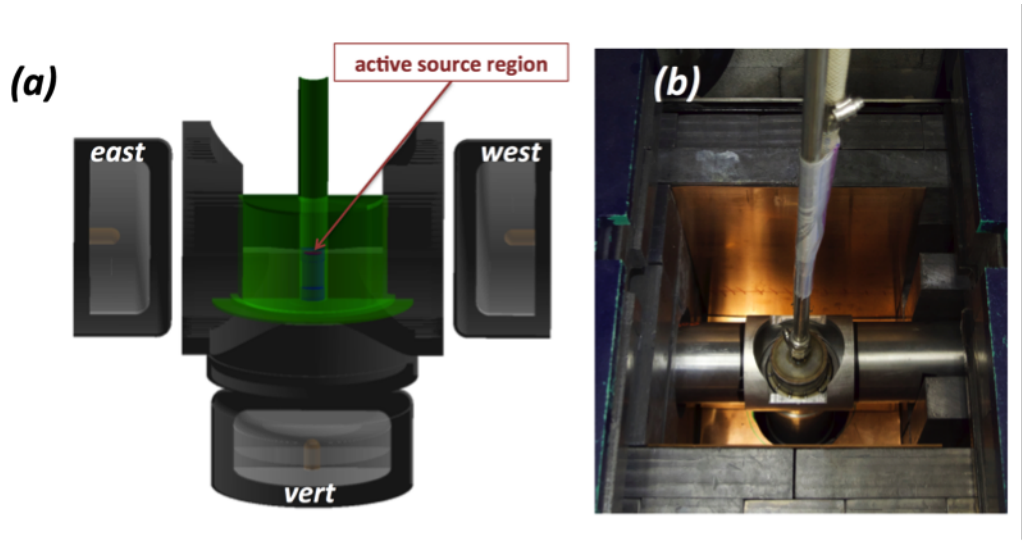

Figure 4.3: (a) GEANT4 CAD rendering of the counting end station and detection system and (b) a photo of the assembled detection system, aluminum alignment device, and pneumatic counting system.

Nuclide	Energy (keV)	Branching Ratio (%)	Emission Rate (γ/sec)	Uncertainty (3-σ)
Cd-109	88.034	3.70	254.46	7.63
Co-57	122.061	85.60	141.40	4.24
Co-57	136.474	10.68	17.64	0.53
Ce-139	165.858	80.00	70.13	2.10
Sn-113	391.698	64.97	156.67	4.70
Cs-137	661.657	85.10	1488.35	44.65
Y-88	898.042	93.70	388.68	11.66
Co-60	1173.228	99.85	1928.52	57.86
Co-60	1332.492	99.98	1931.41	57.94
Y-88	1836.063	99.20	411.46	12.34

Table 4.1: A list of radionuclides contained in calibration standard r-651-c13, their gamma-line energies and branching ratios, and source emission rates at start of counting, 17:04 2/19/15 (EST) are also provided.

an XIA Pixie-4 digitizer for DAQ. The calibration standard was produced by drying an aliquot 0.1004 mL of Eckert & Ziegler source number 1725-53 on a circular piece of 8.7mm diameter Whatman ashless filter paper. Table 4.1 is the list of radionuclides and their respective gamma-lines of interest. A National Instruments PCI-e crate and XIA Pixie-4 digitizer module were used for DAQ [144]. The calibration standard was placed inside of a pneumatic capsule and lowered down into the counting end-station of the Fast Irradiated Rabbit Sample Transfer (FIRST) pneumatic system. The gain was adjusted for each detector using the Pixie-4 module to align the ten gamma-lines from the standard. By gain matching the detectors, data from each of them could be combined by summing the spectra together. Figure 4.4 is a plot of the spectrum from each detector acquired over a four-day calibration count.

After calibrating the three-crystal spectrometer, samples of scandium-oxide, cobalt-oxide, zirconium-fluoride, and aluminum-oxide were irradiated in their respective order separately with a D711 Thermo-Scientific deuterium tritium fusion neutron generator at closest proximity to the neutron generator. Each sample was irradiated for four hours, then counted overnight before starting the next irradiation. The irradiation times, transit time from the neutron generator to the three-crystal spectrometer, sample masses, and purity are reported

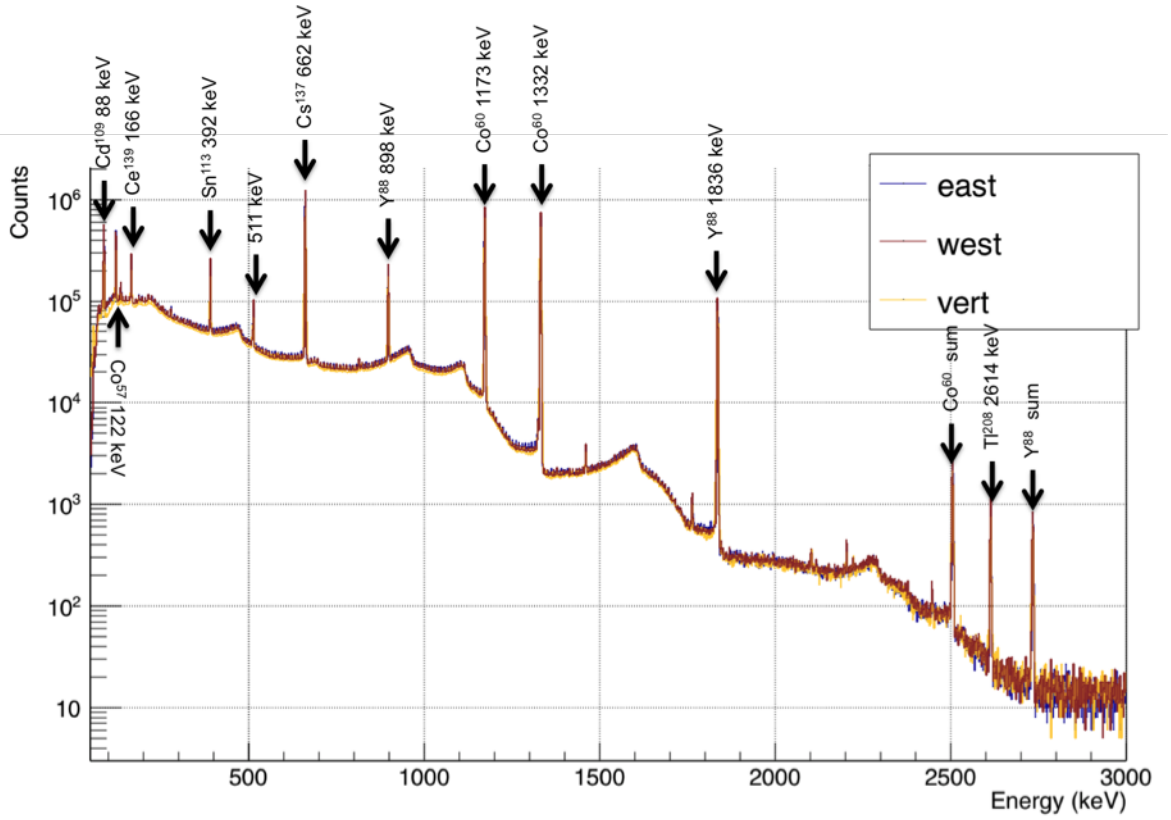

Figure 4.4: Gamma-ray spectra acquired starting on 2/19/15 from the three separate crystals in the spectrometer using the calibration standard (live counting time 313174, real counting time 322418).

Sample	Purity	Irrad. Time (sec)	Transit time from generator to detector (sec)	Mass (g)
Sc2O3	99.999%	14399.1133	0.1988	0.0653
CoO	99.999%	14399.0953	0.2187	0.2040
ZrF4	99.998%	14399.1141	0.2106	0.0677
Al2O3	99.99%	14399.2919	0.3072	0.0320
uncertainty for values are +/-1 in the last decimal place				

Table 4.2: Irradiated sample information.

for each sample in table 4.2. All count data were acquired in list-mode with coincidence counting enabled. Figure 4.5 shows the spectra acquired during the first 10 minutes of counting for each sample. Figure 4.6a presents a 2-dimensional density plot of the coincidence data acquired from manganese-56 generated during irradiation of cobalt-oxide and figure 4.6b presents the complete coincidence plane acquired from the east-west detector pair while counting the calibration standard.

Following the final irradiation of aluminum oxide, a second four-day calibration count was taken to ensure that no change in the calibration was observed.

4.4 Data & Techniques

Activation samples were transferred a distance of approximately 8 meters in 250 milliseconds. For exact irradiation and transfer times, the reader is referred to table 4.2. Calibration of HPGe detectors is a relatively straight forward process using a multi-gamma standard with exception to the correction factors; the most important factors are dead time, pulse pile-up, and true-coincidence summing (TCS) [135, 142]. Dead time was accounted for using gated internal counters inside the DAQ system [145, 146]. Corrections for dead time and pulse pile-up were performed on individual peak areas from gamma spectra post-counting [147]. The final correction, TCS, is painstakingly tedious. TCS occurs when a single radioisotope emits two or more gamma-rays close enough in time that they can be recorded as a single pulse [148]. This process depends on the full-energy peak (FEP) and total efficiencies to

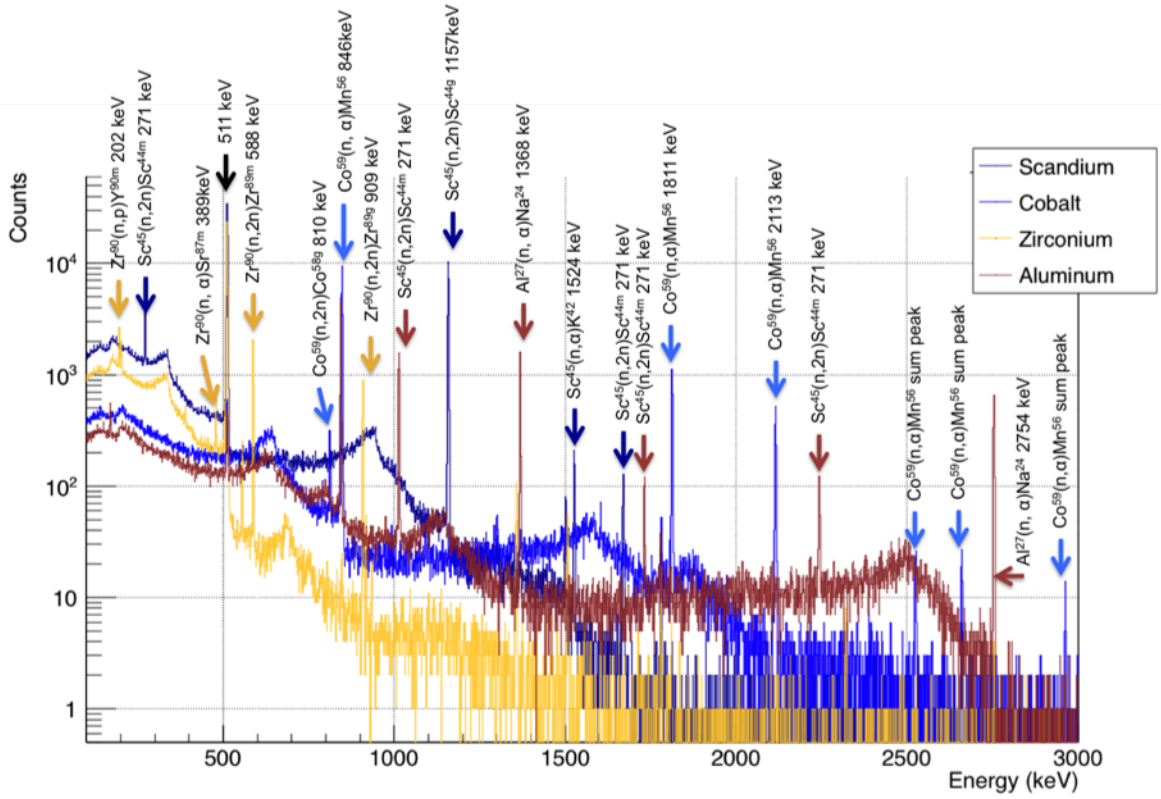

Figure 4.5: First 10 minutes of acquired gamma spectra immediately following the irradiation from east detector. Prominent peaks are labeled for convenience.

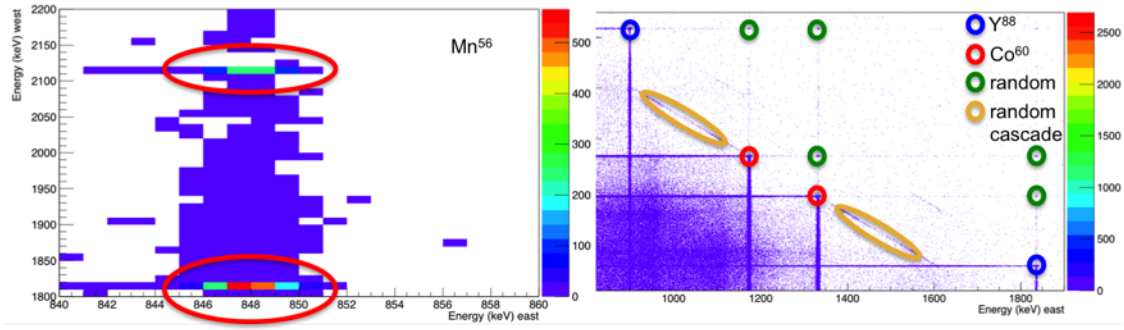

Figure 4.6: Coincidence data acquired from (left) the irradiated cobalt target between detectors east and west and (right) the calibration standard.

account for loss of recorded FEP events from individual gammas from a cascade that are lost after summing with other FEPs or Compton scattered gamma-rays from the cascade [94]. The impact of TCS on gamma spectra peak areas can be analytically resolved using the total efficiency; however, determining the total efficiency of an HPGe detector across the entire calibrated energy range using mono-energetic gamma-ray sources is cost prohibitive and time consuming [149]. This process has been significantly simplified at the expense of precision with the advent of Monte Carlo radiation transport simulation tool kits like MCNP6 and GEANT4. A model of the three-crystal spectrometer was developed using the CERN GEANT4 simulation package to estimate and compare the measured and simulated FEP efficiencies for the radionuclides contained within the calibration standard. The model was adjusted by changing the detector crystal to end cap distance and germanium dead-layer thickness to improve agreement between the measured and modeled FEP distributions until the simulated values fell within 10% of the measurement. The adjustments to the model are discussed and reasons supporting the changes are presented.

All data from the three-crystal spectrometer were acquired using the XIA Pixie-4 digital DAQ system. Events recorded in the spectrometer were saved as time-stamped 14-bit channel values using a 75 MHz clock. Coincident events were recorded within the data stream simultaneously using a different four bit flags. For a detailed description of the data stream the reader is referred to the Pixie-4 User's Manual [144]. List-mode data recorded from the calibration standard and the counting period of each sample following irradiation were parsed using C++ and the CERN ROOT data analysis framework [150]. Each event was placed into one of seven "ROOT" trees and each event was composed of four pieces of information: channel number, time since start of counting, time since the last set of TTL signals from the optical sensors, and total dead-time since start of counting. Singles events within each crystal were recorded in separate files. Coincident events were dissected and added to the respective singles files and recorded separately in either the doubles or triple coincidence file. In total, each list-mode record was separated into eight total files: three single event files for

each crystal, three double-coincidence files for coincidences between east-west, east-vert, and west-vert detector pairs, one triple coincidence file, and one additional file for recording TTL pulses from the optical sensors for timing purposes. An analysis script was written to process the singles list-mode data into both 2-dimensional temporal distributions of events over time and 1-dimensional gamma spectra for peak area analysis. This script used the TSpectrum class of ROOT to identify peak locations and fit the peaks with a linear background and a Gaussian peak [151, 152]. Constrained minimization was used for each peak fit and the peak parameters and covariance matrix were used to determine the peak centroid for the energy calibration, peak width for the energy resolution, and area and corresponding uncertainty for full-energy peak efficiency. A second script was written to estimate peak areas in the double coincidence gamma spectra by fitting a Gaussian peak plus a constant to the timing distribution (see figure 4.9 and/or 4.6 for examples) of an isolated energy-energy region of the coincidence plot that encapsulated the 2-dimensional coincidence peak (see figure 4.6). Peak areas from the coincidence data were compared with the singles data using the singles-to-double coincidence ratio to determine the activity of the Co60 and Y88 radioisotopes in the standard and compared with the activity reported by Eckert & Zeigler. The singles-to-doubles coincidence ratios were first corrected for the angular correlation anisotropy of the gamma-ray cascades of Co60 and Y88 using GEANT4 to estimate the correction factors. After determining the calibration, a GEANT4 simulation was conducted for each gamma-line from the standard to estimate the full-energy and total efficiency. The total efficiency was used to adjust the measured efficiency by accounting for TCS before comparing the full-energy peak efficiencies of the measured and modeled data. This process was repeated multiple times, varying the distance between the crystal and aluminum end cap and the crystal dead-layer until all results were within 10%. This was done to develop a measurement informed simulation model of the spectrometer. List-mode data from the irradiated scandium-oxide, cobalt-oxide, zirconium-fluoride, and aluminum-oxide were also parsed using the same singles spectra analysis script to measure the end-of-irradiation (EOI) activity

of various activation products. The EOI activity of the activation products were analyzed using a simple hand calculation to estimate the total neutron intensity using their 14.5 MeV cross-section as measured from [153]. The distribution of fluence estimates were collected in table 4.8 and compared against the STAYSL PNNL fluence estimate generated from the reaction rate ($\sigma\phi$) values and the MCNP6 neutron energy spectrum simulation. The source for the MCNP6 simulation was generated using the continuous slowing down approximation for deuterons in titanium. The source can be characterized as a software generated set of MCNP distributions for energy and angle dependence of the deuteron-triton fusion reaction. This source was providedu by PNNL and is the same source developed by Rick Wittman and John Hayes [143].

4.5 Results

4.5.1 Detector Efficiency

List-mode data from each crystal were processed using the ROOT analysis script for singles. Figure 4.7 presents the energy resolution and efficiency calibrations for each spectrometer after model optimization and correction for TCS of Co60 and Y88. The FEP efficiency for detector vert is noticeably lower than the other two, especially in the low energy region; this difference is the result of the thick steel bottom of the counting end station. This design asymmetry increased the total material induced attenuation of gamma-rays emitted from the source, negatively impacting the efficiency matching of the geometry. For a visual depiction of this plate, the reader is referred to figure 4.3a. The green circular disk above detector vert, is a 1.3 mm thick layer of stainless steel whereas the walls of the counting end station are only 0.9 mm. Table 4.3 and 4.4 are the values and uncertainties of the fit parameters for the calibrations of each crystal. The functions used to fit the calibration data are provided in the text. The function, provided below, was used to fit the energy resolution data where A is a scalar, x is the energy of the incident gamma-ray in keV, and B is a constant [154].

Detector	A	B
east	0.0392(22)	1.300(26)
west	0.0269(23)	1.302(32)
vert	0.0315(33)	1.081(40)

Table 4.3: Fitting parameters and uncertainties for the energy resolution calibrations.

$$A\sqrt{(x)} + B \tag{4.1}$$

A modified asymmetric sigmoidal function was used to fit the FEP efficiency data where A is a scaling parameter, x is the energy in keV, and w2 and w3 are shaping constants.

$$\frac{A\left(1 - \frac{1}{1+x^{-w3}}\right)}{e^{\frac{-ln(x)+\mu}{w2}} + 1} \tag{4.2}$$

Figure 4.8 contains the full-energy peak efficiency differences between the measured and modeled results before and after optimization. The vendor specified gap of 3 mm for the distance from detector crystal to end cap and 0.5 μm for the dead-layer yielded an over-estimate of the FEP efficiency relative to the measured efficiency. The crystal to end-cap distance was increased for east and west to 4 and 5 millimeters, respectively. The dead-layer for east and vert were changed from 0.5 μm to 0.7 and 0.4, respectively. Generally, the poorest known dimension for HPGe detectors after construction is the distance between the end-cap and the crystal and the dead-layer; it is commonly the starting place for adjusting simulation models to match measured data. More work could be done to further improve the model by taking multiple calibration measurements at varied distances and with different absorbers placed between the source and detectors to identify dead-layer thickness and crystal size; however, radiographs of the crystals would be required for such work and were not available for these detectors [155, 149]. It is likely with a more detailed analysis the source of the asymmetry in the low energy region of the comparison in figure 4.8 could be resolved. The modeled efficiencies matched within 5% for gamma-ray energies above 350 keV.

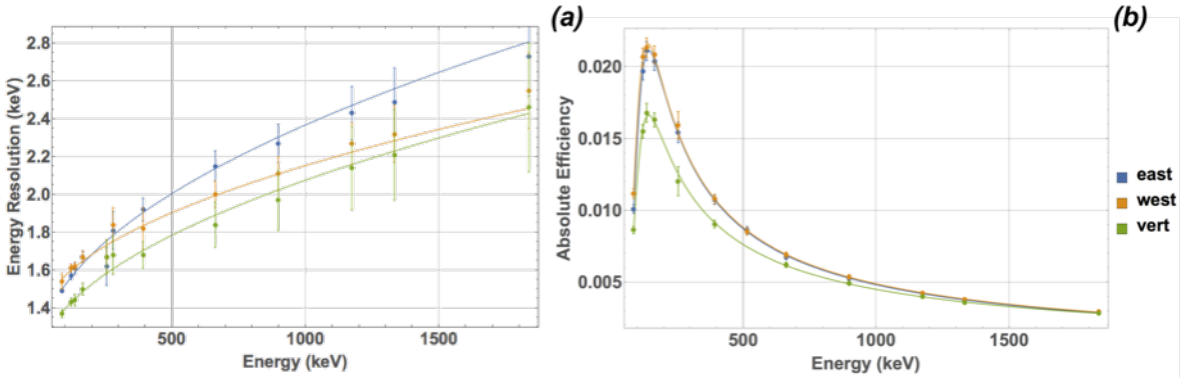

Figure 4.7: (a) Energy resolution (b) and efficiency calibrations for east, west, and vert detectors.

Detector	A	μ	w2	w3
east	1.80(21)	4.663(20)	0.183(11)	0.857(18)
west	1.73(21)	4.636(21)	0.183(13)	0.849(18)
vert	0.879(113)	4.631(24)	0.190(15)	0.763(19)

Table 4.4: Fitting parameters and uncertianties for asymmetric sigmoidal efficiency calibrations.

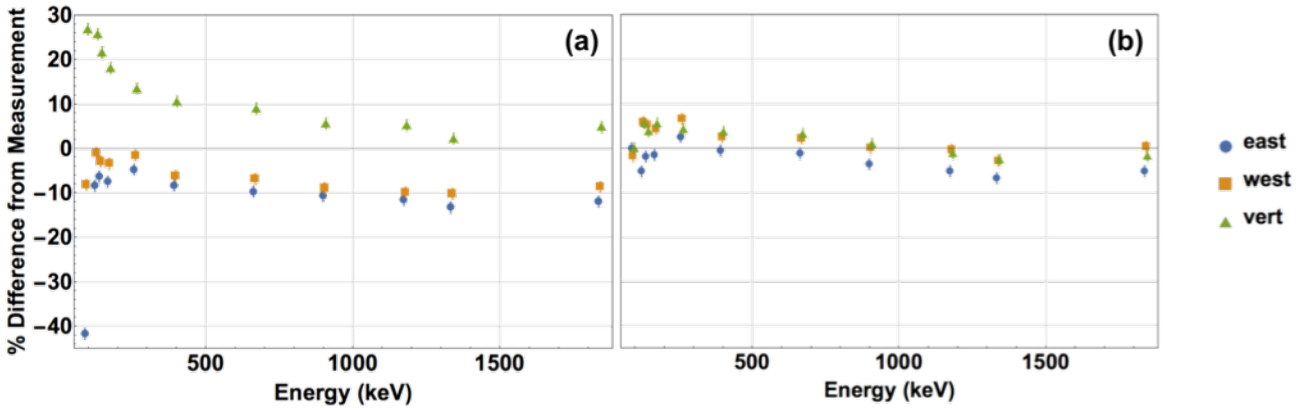

Figure 4.8: Percent difference between the FEP efficiency measured using the r-651-c13 calibration standard and modeled using the GEANT4 simulation for (a) before and (b) after optimization.

4.5.2 Coincidence Timing

Figure 4.9 shows the coincidence timing distributions from all measured events from the standard and fit using a single Gaussian and a constant background to illustrate the maximum timing resolution of the system. There are several oscillations at the top of the timing distributions presented in figure 4.9; these oscillations represent different physical phenomena. Coincidence timing distributions can be broken into three regions: a uniformly distributed random coincidence region, two delayed or time-walk affected coincidence regions to the left and right of the central Gaussian, and a central Gaussian encompassing truly coincident events. The effect of time-walk is illustrated in figure 4.10 [65]. The fit parameters and uncertainties for the timing distributions are shown in table 4.5 and the fitting equation, a Gaussian with a constant parameter is provided below; A is the scaling factor, x is the time difference, A is the centroid, σ is the Gaussian width, and, B is the constant scalar.

$$Ae^{-\frac{x-\mu}{2\sigma^2}} + B \tag{4.3}$$

Singles-to-double coincidence ratios were tabulated for cobalt-60 and yttrium-88 for each crystal pair and compared against the value provided in the source certification. The estimated activities of these radionuclides and their percent difference from the standard calibration certificate are provided in table 4.6. The measured result are well within 1-σ of the certified value provided in table 4.1. Gamma-gamma coincidence exhibits anisotropy in emission intensity as a result of the conservation of angular momentum. Estimates of the angular correction factors and TCS were produced using GEANT4 and used in table 4.6 to correct the singles-to-doubles coincidence ratios. The comparison listed in table 4.6 indicates that the modeling resource used for this work was reliable. Table 4.7 presents the simulated and measured angular correlation correction factors (θ_{CF}) for Co60 and Y88. Two simulations were performed, one assuming isotropic emission of the secondary gamma-ray, the second using rejection sampling from the normalized angular correlation function [156].

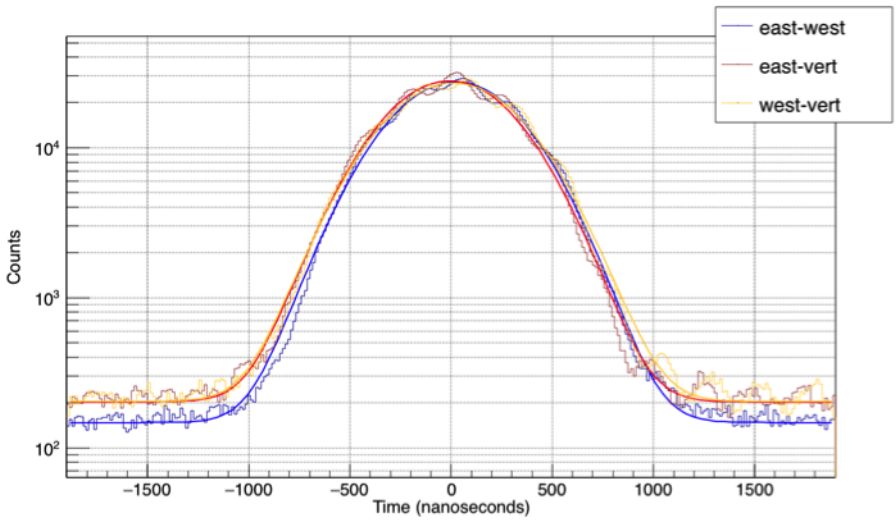

Figure 4.9: Coincidence timing distributions for the three detectors operated in pairs.

Detector Pair	A	x	σ(nsec)	B
east-west	2.4670E5(25)	22.56(25)	298.03(19)	1264.1(87)
east-vert	2.5270E5(25)	-5.73(25)	298.72(19)	1756(10)
west-vert	2.4400E5(24)	15.34(26)	310.34(19)	1763(10)

Table 4.5: Fitting parameters and uncertainties for timing distributions.

The comparison of the singles-to-doubles ratio to the certified activities and the magnitude of the estimated angular correlation correction factors indicate the coincidence detection system data is reliable. It was important to rigorously review the calibration of the three-crystal spectrometer before performing any cyclic activation experiments or counting activation targets for spectral deconvolution to identify and eliminate any systematic errors in the counting system.

4.6 Determination of Neutron Flux

After vetting the energy, resolution, and efficiency calibration, data recorded from the irradiated samples were parsed. Peak areas collected from the spectra were analyzed to determine the $\sigma\phi$ value and a hand-calculation of the total neutron intensity. Table 4.8 lists the reaction rate values for all of the reactions used to estimate the neutron intensity. The

	Co-60		Y-88	
Detector Pair	Meas. (γ/sec)	% Diff. from Cert.	Meas. (γ/sec)	% Diff. from Cert.
east-west	1925(14)(72)	-0.16	421(7)(18)	2.28
east-vert	1932(15)(75)	0.21	412(7)(14)	0.16
west-vert	1930(21)(76)	0.10	405(7)(17)	-1.46

**uncertainties listed are provided as 0% and 3% error in the true-coincidence summing and angular correlation correction factors i.e. 1925(14)(72) means 1925+/-14 assuming no error in the modeled correction factors and 1925+/-72 assuming 3% error in the correction factors

Table 4.6: Percent difference in the activity measured using the singles-to-doubles ratio relative to the standard certificate.

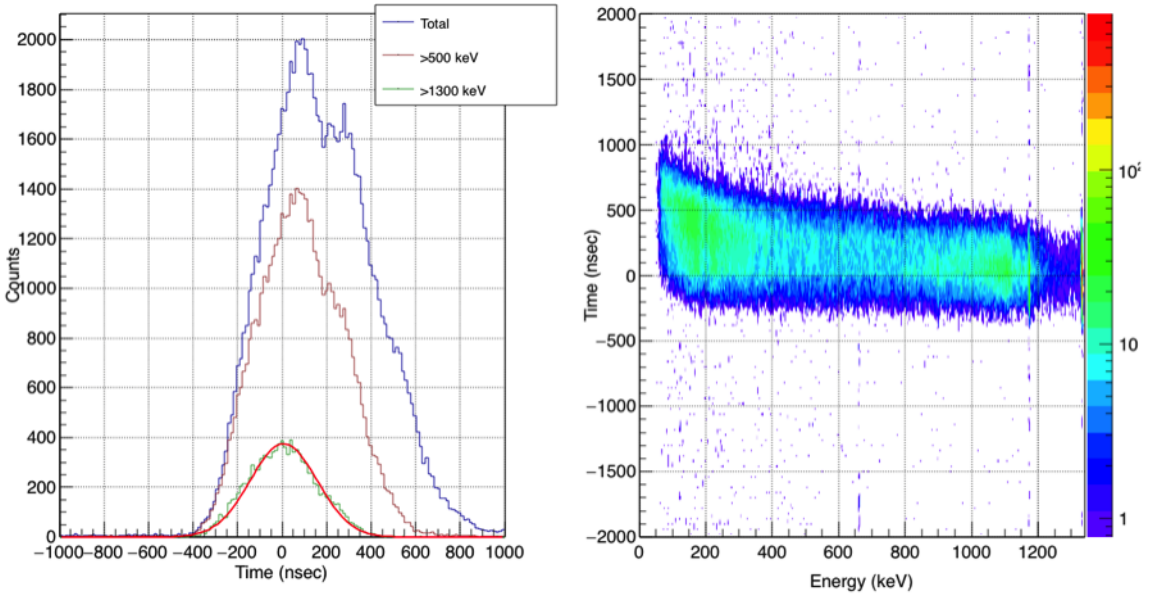

Figure 4.10: Plot illustrating the affect of time-walk on the coincident events recorded from cobalt-60. The figure on the left illustrates the contribution of time-walk from different energy regions. The "Total" timing distribution includes all events from the figure on the right, ">500 keV" and ">1300 keV" are all events greater than the listed energy.

	Co-60		Y-88	
Detector Pair	θ_{CF} (simulated)	θ_{CF} (measured)	θ_{CF} (simulated)	θ_{CF} (measured)
east-west	1.082	1.082(24)	0.953	0.928 (25)
east-vert	0.968	0.966(22)	1.070	1.073(29)
west-vert	0.928	0.927 (21)	1.013	1.027(28)

Table 4.7: Comparison of simulated and measured angular correlation correction factors.

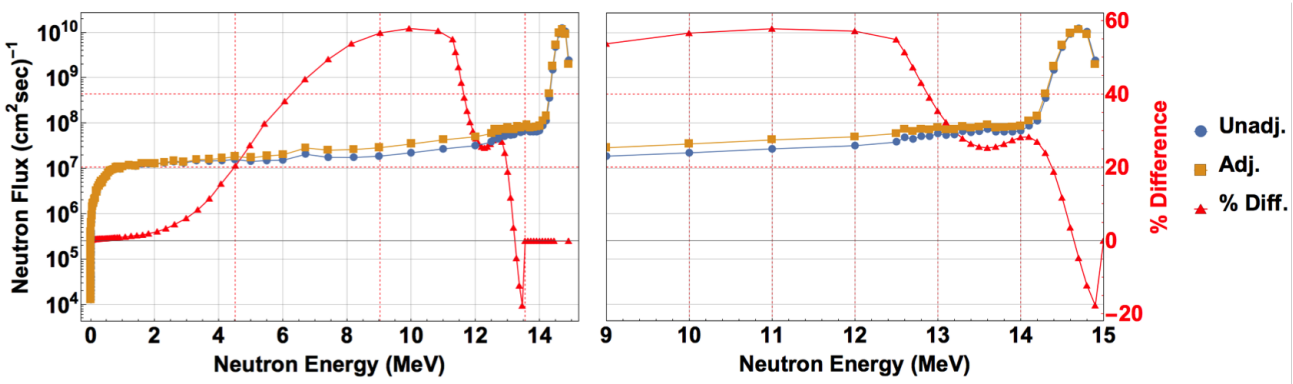

Figure 4.11: Adjusted and unadjusted neutron flux from MCNP6 and percent difference for (a) the complete energy range and (b) the 14.5 MeV peak.

uncertainties in the reaction rate values were tabulated using the standard error propagation formula assuming no correlation between the variables including error from the peak area, FEP efficiency, branching ratio, decay constant, irradiation time, and sample mass. The average neutron intensity and standard deviation were determined to be 2.956E8(174)n/cm^2/s using the 14.5 MeV cross-section and inverse variance weighting of the hand tabulated values in the right most column of table 4.8. After calculating the neutron intensity using a single cross-section, the MCNP6 simulated neutron spectrum and $\sigma\phi$ values highlighted in table 4.8 were used to generate a STAYSL PNNL input deck. Figure 4.11 shows a plot of the unadjusted, adjusted, and percent adjustment of the MCNP6 simulated neutron spectrum to minimize the chi-square difference in measured and simulated reaction rate values. The reduced chi-square of this analysis was 1.011. Table 4.9 shows the tabulated fission rates for thorium-232, uranium-235, and uranium-238 from STAYSL PNNL compared against hand-tabulated estimates. The fission rates for the two fissionable isotopes, thorium-232 and uranium-238, trend as expected with uranium-238 having a slightly worse comparison because of the lower fission threshold. The fission rate estimate for the fissile target, uranium-235, also exhibits the large expected difference of 26.7% lower than the value estimated by STAYSL PNNL because the single cross-section estimate neglects to include the fission contribution from scattered neutrons in the thermal and epithermal range.

The final calibration count was compared against the original calibration to observe any

Reaction	14.5 MeV Cross-Section (barns)	$\sigma\phi$ reaction rate	Flux Estimate $(\text{cm}^2 \cdot \text{s})^{-1}$
Sc45(n,γ)Sc46	-	7.202E-18(186)**	-
Sc45(n, α)K42	5.82E-2(48)	1.899E-17(27)	3.265E8(162)
Sc45(n, 2n)Sc44m	1.21E-1(5)	4.055E-17(53)	3.384E8(93)
Sc45(n, 2n)Sc44g	1.75E-1(9)	5.066E-17(43)	2.889E8(25)@
Co59(n, 2n)Co58g	2.51E-1(21)	7.146E-17(18)**	2.845E8(7073)@
Co59(n, α)Mn56	3.20E-2(9)	8.655E-18(61)**	2.715E8(47)
Co59(n, p)Fe59	4.84E-2(17)	1.300E-17(28)	2.682E8(79)
Zr90(n, α)Sr87m	4.55E-3(19)	1.036E-18(10)	2.623E8(168)
Zr90(n, p)Y90m	1.23E-2(5)	3.559E-18(49)	2.924E8(74)
Zr90(n, 2n)Zr89g	6.87E-1(98)	2.033E-16(15)**	2.852E8(238)@
Al27(n, p)Mg27	7.41E-2(25)	2.235E-17(32)**	3.020E8(72)
Al27(n, α)Na24	1.13E-1(1)	3.721E-17(35) **	3.356E8(44)
Average (1σ)	–	–	2.956E8(174)

**input to STAYSL PNNL
@special calculation includes ingrowth of isomer uncertainty is listed using standard ENDF formatting the values in parenthesis succeeding each value is the uncertainty starting from the last significant figure i.e. 5.78E-2(48) means 5.78E-2 +/- 4.8E-3

Table 4.8: List of reaction rates, 14.5 MeV cross-sections used to estimate flux, and the flux estimate.

Actinide	$\sigma\phi$ (STAYSL)	$\sigma\phi$ (Est.)	% Diff.
Th-232	1.190E-16(111)	1.156E-16	-2.87
U-238	3.671E-16(259)	3.500E-16	-4.65
U-235	8.471E-16(894)	6.208E-16	-26.7
Flux Estimates	2.923E8(136)**	2.956E8(174)	–

**STAYSL PNNL estimate of flux above 9 MeV, total flux, including thermal flux was estimated at 3.396E8(137)

Table 4.9: Estimated fission rates for thorium-232, uranium-238, and uranium-235 irradiated at the UofM-NSL acquired from STAYSL PNNL.

systematic changes over the experiment. Differences on the order of approximately 0.1% were observed in the energy, energy resolution, and efficiency calibrations, well below the statistical precision of the certified standard.

4.7 Closing

A new three-crystal HPGe spectrometer for short-lived fission product studies has been successfully calibrated and tested for stability for both singles and coincident gamma-ray data acquisition. The array was found to be stable across the experimental campaign and reliable using the singles-to-doubles coincidence ratio. Using the GEANT4 measurement informed simulation model for angular correlation and TCS corrections and the raw coincident data, the activities of Co60 and Y88 were estimated and compared to the standard calibration certificate. The activities measured in this way were well within 2σ of the certificate value. The neutron intensity and neutron energy spectrum have been estimated using neutron dosimetry techniques and neutron activation analysis. Four sample materials were irradiated and counted using the three-crystal spectrometer to estimate the total neutron intensity and neutron energy spectrum using STAYSL PNNL. Even with such limited thermal contamination, the fission rate contribution from the epithermal to thermal range was 26.4%; with such a large discrepancy between the fission rate calculated from the product of the flux and the flux weighted average energy cross-section and the estimate provided by STAYSL PNNL, it is clear why it becomes so critical to characterize the neutron source at 14 MeV for fission yield studies. The increase in the fission rate comes from lower energy neutron contamination; thus, measured fission yields using this source are not purely 14.5 MeV neutron induced fission events. The measured fission yield distribution becomes a convolution of the 14.5 MeV distribution and other lower energy neutron induced fissions. Using the information gathered from this characterization, list-mode data acquired from cyclic neutron activation of thorium-232, uranium-238, and uranium-235 will be analyzed using singles and coincident data to measure independent and cumulative fission yields of

fission products with half-lives on the order of seconds.

CHAPTER V

Fission Product Yield Measurements

5.1 Introduction

Fission yields and the fission process have been under investigation since the discovery of fission by Lise Meitner and Otto Frisch in 1935 [157]. From the original fission yield curves measured using radiochemical assay, to the highest precision measurements performed using ISOL, SPIDER, LOHENGRIN, OSTIS, Miss Piggy, and TITAN [158, 159, 53, 160, 47, 161], nuclear fission and the fission process have continued to provided new insights into the shell structure of the nucleus, prolate and oblate nuclei, the interstellar r-process, and the nuclear structure of multi-fermion systems [162, 106, 163, 104, 164, 165]. Even with over 84 years of study, a complete model of fission capable of accurately predicting the independent yields of all the fission products, including isomers, has yet to be completed. The most current and accurate model is the Bohr liquid drop model expanded to include: assumptions about charge distribution, random neck rupture, multi-modal fission (symmetric and asymmetric break-up), shell structure, nucleon pairing, and nuclear shape effects [141, 166, 167]. This complex, energy-dependent model requires further development and is in need of more accurate fission yield estimates from experimental observations for comparison.

Improvements in fission yield data not only support improvements in the fundamental understanding of the fission process, but also have real- world engineering applications. Fission yield measurements have been found to be a primary source of uncertainty in fission

pulse decay heat calculations [168], differences in fission yields have been observed and used to discriminate between different actinides for nuclear forensics [169], and fission yields are important to reactor fuel inventory, medical isotope production, and neutron dosimetry modeling calculations [170, 171, 172].

An experiment was designed to produce bulk fission product spectra emphasizing radioisotopes with half-lives on the other of seconds to support the nuclear forensics mission in expediting the analysis of post-detonation nuclear material, . Equipment at the University of Michigan was used to examine these short-lived fission products, leveraging heavily on the existing nuclear data to identify observed fission products from their temporal behavior and coincident gamma-lines. Measurement results obtained from bromine, krypton, and xenon fission products were compared against published fission yields from ENDF VII.1 to determine the validity of the data, and several newly-measured fission yields are presented.

5.2 Experiment

Three separate actinide targets—^{232}Th, ^{238}U, and ^{235}U—were heat sealed in polyethylene and cyclically irradiated using a D711 Thermo-Scientific deuterium-tritium fusion neutron generator and a pneumatic shuttle system to measure the fission yields of fission products with half-lives greater than 0.5 seconds. These targets were selected because they posed the smallest contamination hazard, were readily available, and are relevant to nuclear forensics. Three coaxial high-purity germanium (HPGe) detectors were used to acquire data in list-mode in coincidence using an XIA Pixie-4 digital data acquisition system to study the delayed gamma emissions of short-lived fission progeny from the fissioned actinide targets. All three 40% relative efficiency HPGe detectors were of the same dimension (within 0.1 mm). The detectors were 84.5 mm diameter cylinders that were 32 mm deep with a bevel radius of 8 mm. The cold fingers were 8.8 mm in diameter and extended 16.3 mm into the detectors. All three detectors were placed 3.03 inches from the center of the active source region shown in Fig. 4.3. The full-energy peak and total detection efficiencies were studied

using the GEANT4 radiation transport simulation C++ framework and an Eckert & Zeigler calibration standard. Detection performance was benchmarked by matching the modeled and measured efficiencies. Sensitivity of the coincidence array was studied by comparing the measured and modeled angular correlation correction factors for ^{88}Y and ^{60}Co. The angular correlation correction factors were found to be in good agreement (see Ref. [2]). The precision of the coincidence timing and the impact of "time-walk" were also observed; the timing resolution between coincident events was found to be $\approx$ 170 nanoseconds and the full-width at half-maximum of all coincident events was $\approx$700 nanoseconds (see Ref. [2]). For a detailed description of the detector, generator, and pneumatic transfer system, the reader is referred to Refs. [173, 174, 2].

To prepare the ^{232}Th target, about half a gram of ^{232}Th-nitrate was dissolved in 8M nitric acid and passed through a column of Dowex-1 resin. The lead, bismuth, and radium daughter decay products remained in solution while ^{232}Th was captured on the column [175]. Five column volumes of 0.1M nitric acid were then passed through the column to strip the cleaned ^{232}Th. The cleaned ^{232}Th nitrate in solution was boiled down at 95°C overnight and then calcined at 500°C for four hours. The final target mass after separation was 0.1199 grams. The cleaned ^{232}Th oxide yield was a factor of 4 lower ($\approx$ 20% yield) than anticipated but was large enough to conduct the measurement.

Each target was placed in a small polyethylene cup after cleaning the polyethylene using Alconox soap, rinsing with deionized water, rinsing with acetone, and air-drying in a clean container covered with a sheet of filter paper. Fig. 5.1 is a photo of two of the irradiated targets, two other colored powders for additional contrast, and a pneumatic capsule. The polyethylene cup is a 17.78 mm tall cylinder with a diameter of 9.45 mm, a 1.27 mm deep recess, and a diameter of 8.33 mm at the top. Targets were added to the recess, and a 0.635 mm thick 8.33 mm diameter plug was placed over the powder and pushed into the body of the polyethylene cup. The assembled internal encapsulation was inserted into a stainless steel press. The press was locked under high pressure and heated to 140°C for three hours,

and then set out to air cool for 24 hours [174, 2]. After cooling, the heat-sealed internal encapsulation was inserted into a pneumatic rabbit capsule for CNAA. Figures depicting the irradiation and capsule geometries can be found in Refs [174, 2].

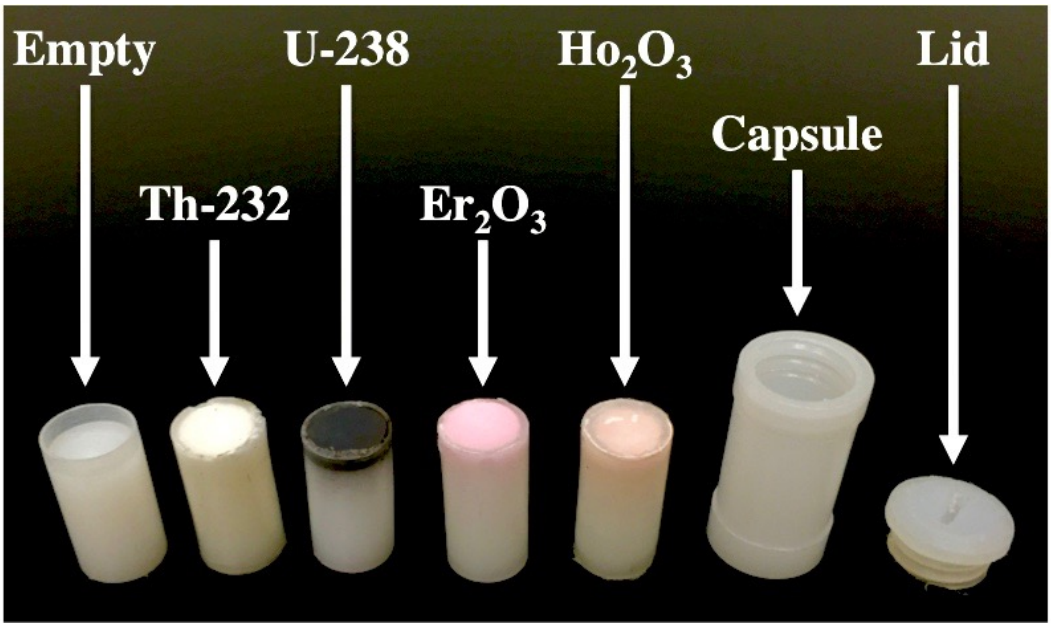

Figure 5.1: Photo of an empty internal encapsulation (left), two of the irradiated target materials (^{232}Th and ^{238}U), two additional colored powders for contrast (Er_2O_3 and Ho_2O_3), and a cyclic pneumatic capsule and lid (right).

Each cyclic irradiation entailed sending the target from the radiation detectors to the face of the neutron generator for a 5 second irradiation. At the end of the irradiation interval, the target was sent back to the radiation detection system using pressurized helium gas for a count period of 200 seconds before re-irradiation. For additional information about the heat sealing process and cyclic irradiation of targets, the reader is referred to [173, 174, 2].

Each target was irradiated over 200 times to produce $\approx 10^8$ fissions in each target as was done in Ref. [176]. Additional cycles were performed on the ^{232}Th target to approach 10^8 fissions but were cut short to focus on the uranium targets. Tab. 5.1 provides target and irradiation information.

The irradiation time was found to be consistent for the uranium experiments but was much broader for ^{232}Th (see Fig. 5.2a). The broadened irradiation time and bimodal transit

Table 5.1: Target information and irradiation history. The number of cycles, average irradiation times, count times, and estimated total fissions are provided.

Target	Type	Purity	Mass (grams)	Number of Cycles	Irrad. Time (sec)	Count Time (sec)	Total Fissions $\times 10^8$
^{232}Th	oxide-powder	99.99%	0.1199	326	5.0949(41)	207.16(26)	0.541(50)
^{238}U	metal	99.95%	0.2083	249	5.0898(9)	206.76(11)	2.48(17)
^{235}U	metal	99.5%	0.2113	201	5.0893(15)	206.75(6)	4.64(50)

time distributions (Figs. 5.2b and 5.2c) for the ^{232}Th experiment are the result of the loss of pressure in one of the two helium feed cylinders to the pneumatic system during the experiment. Both feed cylinders are located inside the irradiation control area and could not be changed out during generator operation. Because the system was still operational and the irradiation and transit times were still within the acceptable margin of operation, the experiment was not stopped. ^{232}Th was irradiated first to identify any possible issues with the system before irradiating the high-quality uranium targets. Based on the significant decrease in the spread of irradiation, transit, and count times shown in Figs. 5.2a—5.2d observed from the uranium targets, the initial testing with ^{232}Th was successful.

The transit from the shielded radiation detection end station of the pneumatic system to the irradiation position (Fig. 5.2c) in contact with the fusion neutron generator was more consistent than the return time (Fig. 5.2d); however, the minimum return time was kept below 0.5 seconds to ensure detection of the short-lived fission products. Only 4 cycles performed during the ^{232}Th target irradiation fell beyond this threshold.

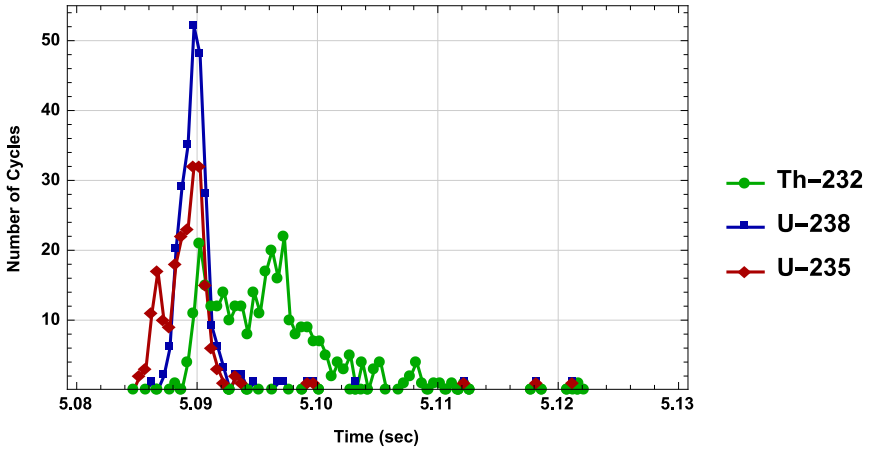

(a) Timing distributions of the irradiation time.

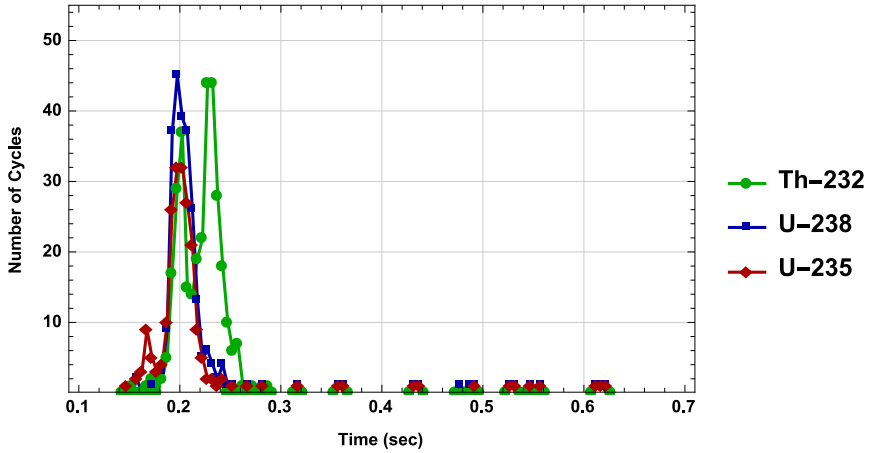

(b) Timing distribution of the capsule transit from the radiation detectors to the neutron generator.

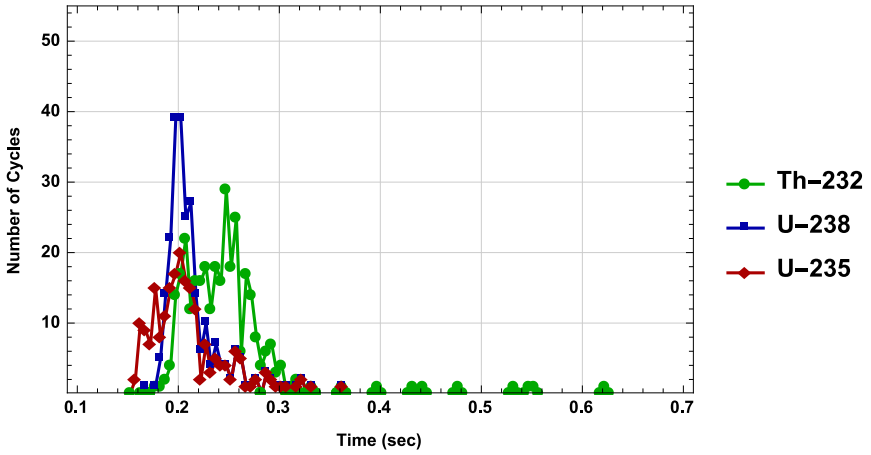

(c) Timing distributions of the capsule transit from the neutron generator to the detector.

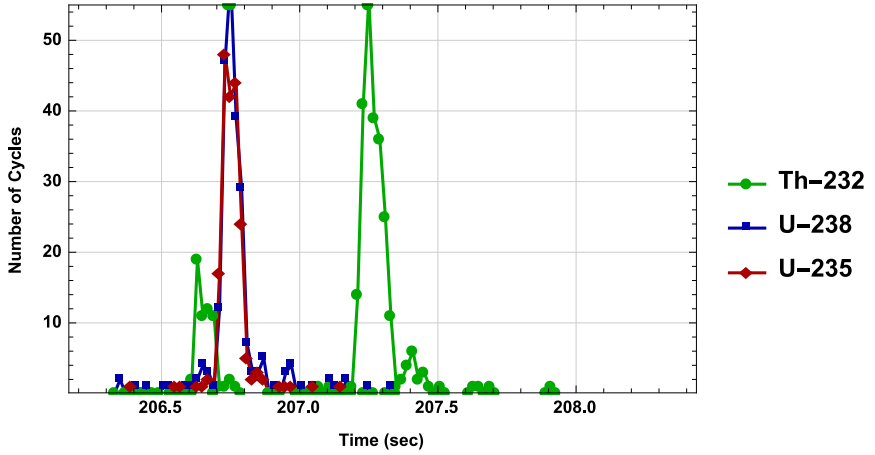

(d) Timing distribution in the counting period following each 5-second irradiation.

Figure 5.2: Timing distributions measured from the experiment.

The detection system were characterized just before and throughout the experiment using a calibration standard prepared by Pacific Northwest National Laboratory that exactly matched the counting geometry of the actinide targets. The calibration standard was produced after drying 0.1004 mL of Eckert & Ziegler mutli-gamma standard on an 8.33 mm diameter piece of Whatman ashless filter paper. The energy, resolution, full-energy peak efficiency, and coincident timing of the three HPGe detectors that made-up the detection system did not change throughout the experiment. Two of the three HPGe detectors were placed horizontally and uniaxially centered about the target. The third was placed vertically, centered between the two detectors facing the target. Fig. 4.3a shows the GEANT4 modeled cross-section of the three HPGe detectors, and Fig. 4.3b is a photo of the detection system. The neutron generator output was measured throughout the experimental campaign using four activation targets: scandium-oxide, cobalt-oxide, zirconium-fluoride, and aluminum-oxide. Data from these targets were used in conjunction with STAYSL PNNL (see Ref. [177, 2]) neutron spectrum unfolding software to determine the neutron flux energy-intensity distribution and total number of fissions from the actinide targets. The MCNP6 and STAYSL adjusted flux are presented in Fig. 4.11. The total flux above 9 MeV was measured to be $2.96(17) \times 10^8$ neutrons per cm^2·second. A detailed description of the detector and neutron generator characterization are provided in Ref. [2].

5.3 Data & Analysis

List-mode data acquired from the three-crystal spectrometer using the XIA Pixie-4 module consisted of a continuous stream of recorded events and the timing of each event relative to a 75 MHz clock. The stream of events were parsed into eight files: three single event files, one for each detector, three coincident event files (one for each detector pair), a triple coincidence event file, and one timing file containing events recorded from voltage pulses generated by optical position sensors located at each end of the pneumatic system that were triggered by the pneumatic capsule's movement. Each event parsed from the raw list-mode

stream contained three pieces of information: the event channel, time since the start of acquisition, and total dead-time since start of acquisition. The time since end-of-irradiation was estimated by treating the moment the count-rate in all three detectors promptly exceeded 1000 counts per second as the start of counting. The time difference measured from the optical sensors was subtracted from the start-of-count time to estimate the end-of-irradiation time. Dead-time for each cycle starting from the start of acquisition was calculated as the difference in the dead-time clock within the counting interval and the dead-time at start of acquisition. Dead-time was averaged across all cycles to estimate the dead-time in the aggregated 200-second count window. The three dead-time effects were: 1) dead-time from trapezoidal shaping of pre-amplifier pulses, 2) dead-time from pauses in data acquisition due to gate-lock from coincident events, and 3) dead-time from data write-lock while the buffer was transferred to the computer hard-drive.

After processing the raw list-mode data, both single and coincident gamma data from each target were examined using heat maps of the temporal distributions of the singles data and coincident planes to identify short-lived gamma-lines and infer their identity from available nuclear data. Fig. 5.3 shows the time-sliced singles gamma spectra acquired using a 1050-1150 keV energy and 0-60 second time window.

After identifying a region of interest (ROI), the coincidence plane was examined to identify coincident gamma-lines. Fig. 5.4 is the coincidence slice obtained from the 1118 keV gamma of ^{90}Kr using a 12 keV window spanning 1112-1124 keV and 0.5-160 seconds of the counting window. Fig. 5.4a is the 1-dimensional spectrum from all events shown in Fig. 5.4b. Fig. 5.4b shows a selection of the 2-dimensional coincidence distribution spanning 0 to 600 keV on the x-axis and 1112-1124 keV on the y-axis. The prominent coincidences are labeled in Fig. 5.4.

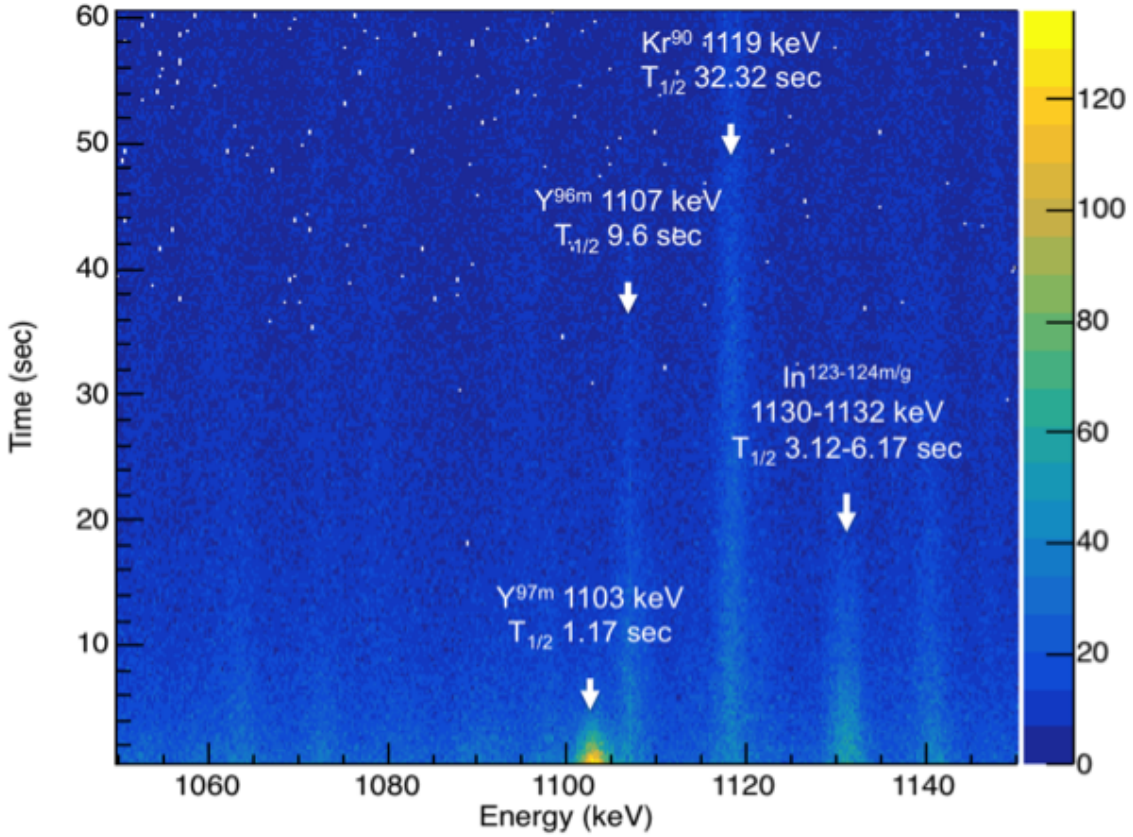

Figure 5.3: Temporal distribution for 1050-1150 keV and 0-60 seconds using 250 millisecond time bins obtained from the cyclic irradiation of ^{235}U. Gamma-lines for metastable ^{96}Y and -97, ^{90}Kr, and the ground and metastable (m/g) states of indium-124 are visible.

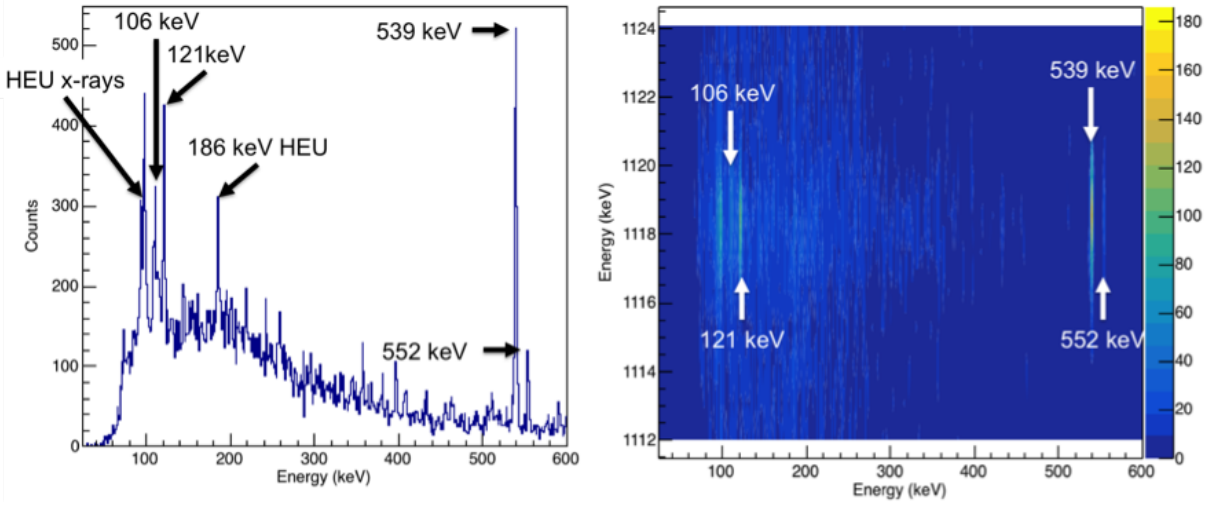

Figure 5.4: Coincidence plane projection slice spectrum (left) and 2-dimensional coincidence plane (right) obtained using an energy range of 1112-1124 keV and a time range of 0.5-160 seconds from the cyclic irradiation of ^{235}U.

5.3.1 Peak Area Corrections

5.3.1.1 Gamma Self-shielding

Gamma self-shielding or self-attenuation is the effect whereby gammas emitted from the target are lost due to interactions inside the target material [178]. The impact of this correction on the low-density ^{232}Th-oxide powder target was small, but self-shielding was a significant factor for the metal uranium targets. Fig. 5.5 is the self-shielding correction factor for the uranium metal targets as a function of incident gamma energy for each detector. Self-shielding correction factors for the points shown in Fig. 5.5 were obtained from the ratios of two simulated detection efficiencies. The first simulation used polyethylene as the active source region (see Fig. 4.3), and the second used uranium metal. Two of the three HPGe detectors, east and west, counted the metal foils perpendicular to the foil face, increasing the total target self-shielding as shown in Fig. 5.5.

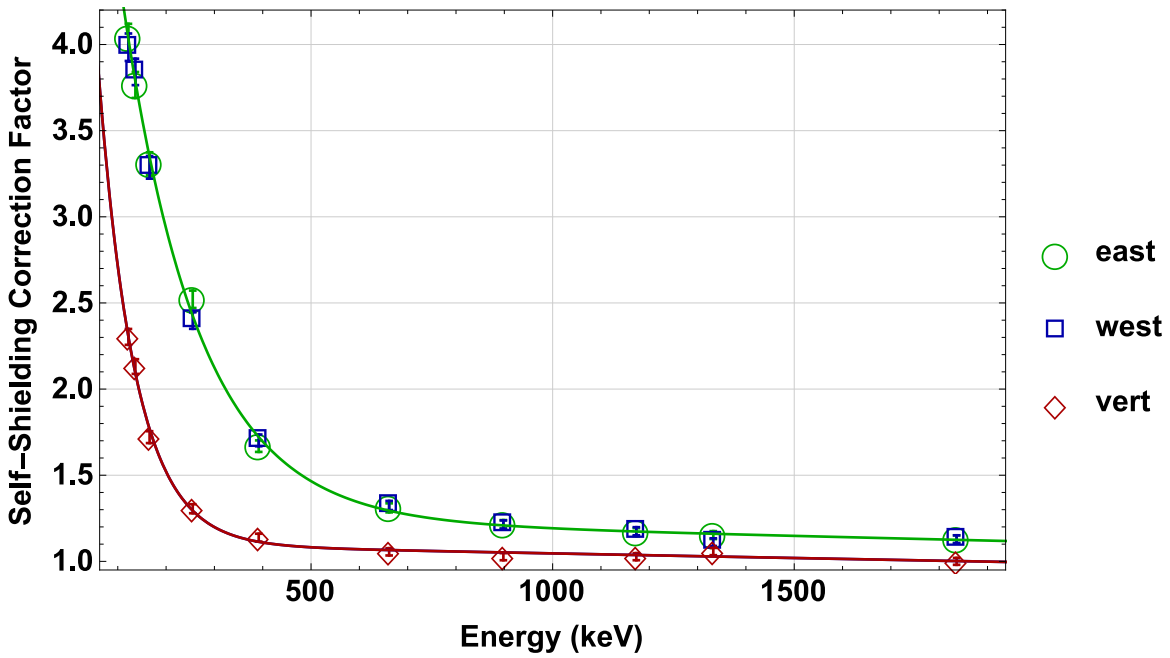

Figure 5.5: Self-attenuation correction factor as a function of gamma energy by detector. The residual-χ^2 of the fitted function for detectors east, west, and vert were 1.2, 1.2, and 1.3 respectively.

5.3.1.2 Dead-time

Dead-time correction techniques are well established and rely on internal gate monitors to determine how often a detector is unavailable to process an event. In this experiment, an internal gate monitor was provided by the Pixie-4 module; however, there was some concern about its accuracy at high dead-time. Due to this concern, a more precise, independent correction technique was used. Peak areas from the 186 and 205 keV gamma-lines of ^{235}U were polled every 1 and 5 seconds, respectively, throughout the 200-second counting window. These two peak areas were corrected for self-shielding by multiplying by the self-shielding correction factor for their respective energies, then they were used to estimate the mass of ^{235}U. The ratio of the known mass divided by the measured estimate was used as the dead-time correction factor. The estimated mass as a function of time from the two ^{235}U gamma-lines is shown in Fig. 5.6. The residual-χ^2 for each fit is provided with the notation $N|\chi^2|$.

The measured mass from 150 to 200 seconds of the 200-second counting period was ≈5% below the mass listed in Tab. 5.1. The dead-time reported by the XIA Pixie-4 gate monitor at this time was 4.9%, in good agreement with the 5% deviation from the true mass. The agreement between the estimated dead-time using the mass ratio and that of the XIA Pixie-4 module in the 150 to 200 second counting window indicates that the self-shielding correction factor derived from the modeled detection system was reliable and quite accurate. Using this technique a dead-time correction factor as a function of the ratio of live-time divided by real-time reported by the XIA Pixie-4 module was developed. Fig. 5.7 is the dead-time correction factor as a function of the ratio of live-time divided by real-time reported by the XIA Pixie-4 module used in this experiment. The dead-time correction factor was determined using the fit shown in Fig. 5.7 for each time-sliced spectrum and then multiplied by the peak areas estimated from said spectrum to get the true peak area.

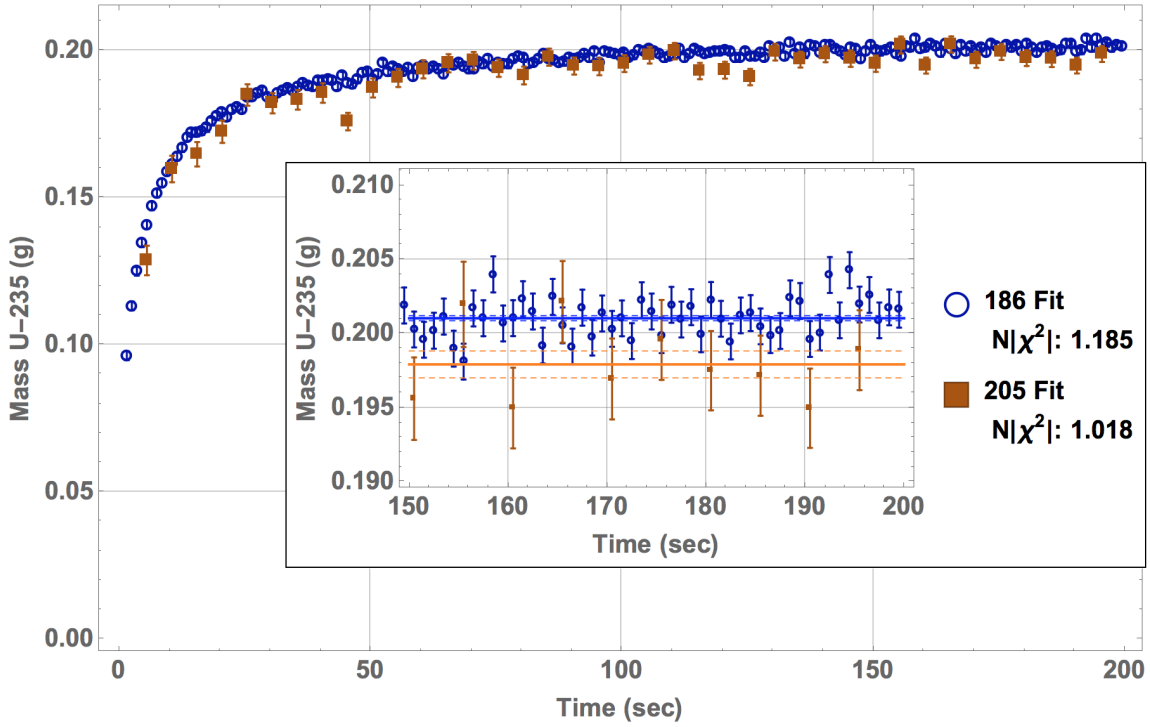

Figure 5.6: Mass of ^{235}U estimated using the 186 and 205 keV gamma-lines corrected for self-shielding and not corrected for dead-time.

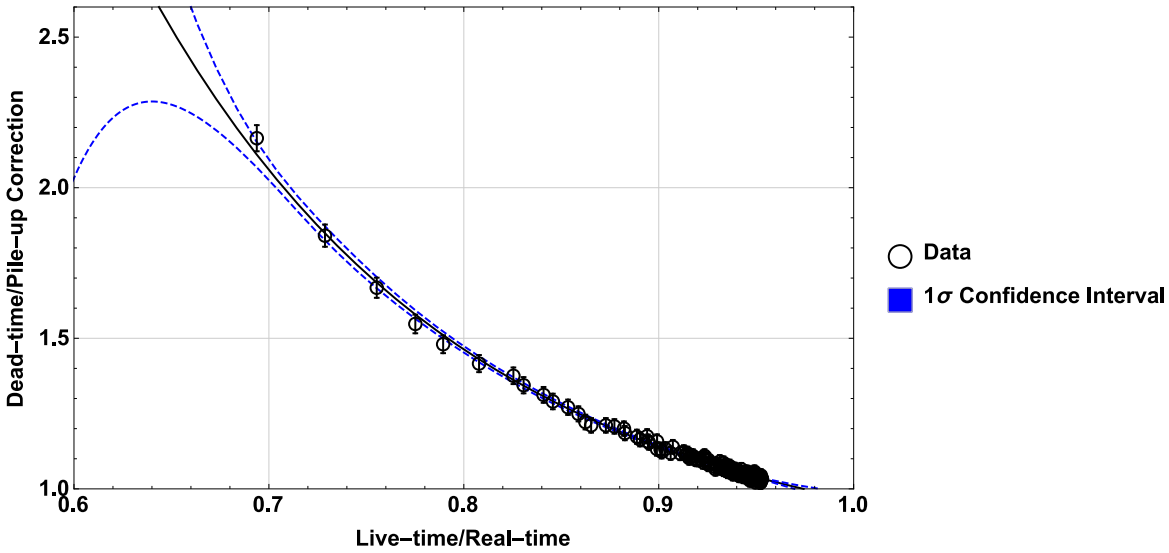

Figure 5.7: Dead-time correction function from the 186 and 205 keV gamma-lines from ^{235}U as a function of the ratio of live-time divided by real-time reported by the XIA Pixie-4 module.

5.3.2 Isotope Identification

After identifying the prominent coincidences and correcting the peak areas obtained from the time-sliced singles spectra, an estimate of the half-life was made by fitting a simple exponential function to peak areas extracted from the ROI and corrected for gamma self-shielding and count-losses from dead-time and pulse pile-up. The half-life estimate from the corrected peak areas and energies of the prominent coincidences were used to identify the radioisotope using the java-based nuclear information software (JANIS 4.0) provided by the Nuclear Energy Agnecy [179, 180] and Nudat 2.0 provided by the National Nuclear Data Center at Brookhaven National Laboratory [180]. For example, the 1118.7 keV gamma-line had four prominent coincident lines: 106, 121, 539, and 552 keV emissions of ^{90}Kr (see Fig. 5.4). Based on the fit to the 10 peak areas extracted using 20-second time bins along the 200-second counting window, the half-life was found to be 29.76(79) seconds. Using these five coincident gamma-lines and the half-life estimate, the gamma-line was identified as ^{90}Kr.

After identifying the gamma-line, peak areas were re-extracted from the 200 second counting range using time bin widths equal to the smaller of two values: one half the best published estimate of the half-life or 10 seconds. For example, the half-life of ^{90}Kr is 32.32 seconds [181]; thus, half the half-life is 16.16 seconds: 16.16 seconds is larger than 10 seconds, meaning 10 second time bins were used to extract peak areas from the data. Peak areas were only extracted from a window within the 200-second counting range starting 0.5 second post-irradiation and no longer than five times the half-life. For example, because 10-second time bins were used for ^{90}Kr, the total number of peak areas extracted from the data were ((5*32.32-0.5)/10)=16. An estimate of the fission yield was derived from each peak area, corrected for residual carry-over activity (see Ref. [182]) from previous cycles, efficiency, time-dependent decay (using the irradiation time and best estimate of the half-life derived from ENDF/B-VII.1), gamma branching ratio, target fissions, self-shielding, and dead-time. True-coincidence summing corrections were not applied to the peak areas; the summing

correction factor for ^{88}Y and ^{60}Co were found to be small relative to the other major sources of uncertainty (see Ref. [2]). Fig. 5.8 illustrates the fission yield estimate generated from each peak area acquired from the 1118.7 keV peak of ^{90}Kr.

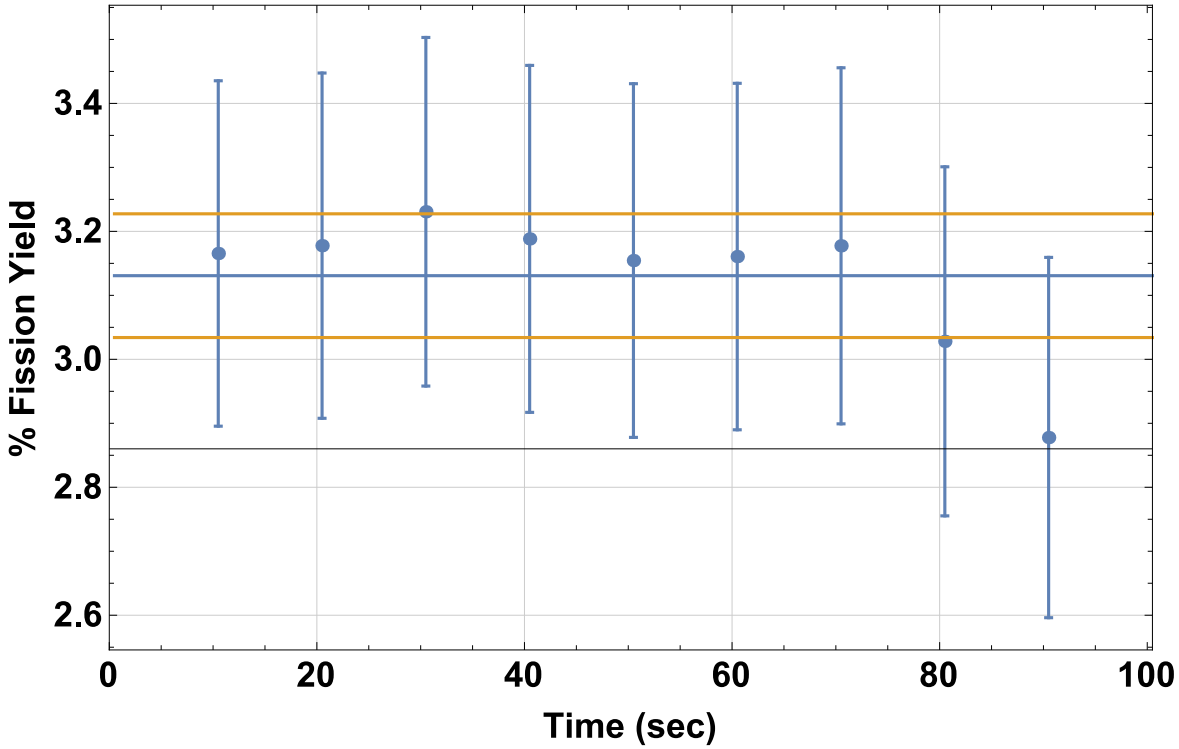

Figure 5.8: Fission yield estimates over-time from the 1118 keV gamma-line of ^{90}Kr. After 90 seconds, peak fit chi-squared, centroid, and peak width vary significantly. Error bars are 1σ and include the uncertainty from the half-life, branching ratio, irradiation time, dead-time, and counting statistics, the largest source of error being the branching ratio.

Uncertainty is a critical part of each fission yield estimate. Referencing the equivalence relation between the first-order Bateman (D_1) equation and the peak area (C) listed as equation (5.3) [182, 183, 147, 184], there are several sources of uncertainty in the estimate of the fission yield (Y_1). These sources of uncertainty are the detector efficiencies of each HPGe detector (east, west, and vert) ($\varepsilon_e + \varepsilon_w + \varepsilon_v$), half-life ($T_{1/2}$), branching ratio ($\Gamma$), irradiation time ($\tau$), counting time ($\Delta$), target mass ($m$), self-shielding ($CF_{SS}$), dead-time ($CF_{DT}$), and fission rate ($\sigma_f \phi$). The detector efficiency was measured using an external NIST traceable standard that was fabricated to exactly match the counting geometry of the irradiated actinide targets. The design tolerance was 10-thousandths of an inch for a counting geometry

where the detectors were 3.03 inches from the target: uncertainty from geometric differences in standard and targets were ignored. The uncertainty quoted by Eckert & Zeigler for the gamma-lines in the multi-gamma standard was 3.1% at 3σ. This uncertainty is not correlated with any other source of error. The irradiation time was measured using the internal clock of a National Instruments DAQ [174, 2] and was assumed to not be correlated with any of the other variables. The half-life and branching ratio were taken from ENDF/B-VII.1 [185] and assumed to have no correlation with this measurement. Count-time was measured from the internal clock of the XIA Pixie-4 module and was also assumed to have no correlation. The target was was measured using a calibrated Mettler and Toledo mass balance scale and was not correlated with any other source of uncertainty. The self-shielding correction factor was verified using the ^{235}U mass measurements and generated from a simulation model. Because the dead-time correction factor was generated by from the self-shielding corrected ^{235}U gamma-lines, these two corrections are weakly correlated: if the self-shielding correction were to increase the dead-time correction factor would decrease. Because these correction factors are inversely-correlated, accounting for their correlation would decrease the estimated uncertainty. The correlation was not included, increasing the overall reported uncertainty. The fission rate is correlated with the detector efficiencies. If the efficiencies of the three detectors were to increase, this would have decreased the measured activity of the activation materials used to correct the MCNP predicted neutron spectrum using STAYSL PNNL. A decrease in the measured activity would have decreased the estimated flux; thus, decreasing the estimated fission rate. The inverse-correlation between these two variables was also ignored.

Tab. 5.3 provides the list of uncertainties and their percent magnitude. The largest sources of uncertainty were the half-lives, self-shielding correction factor, and fission rates. Uncertainty in the half-life is based on the current state of the nuclear data provided in the Evaluated Nuclear Data Files. The self-shielding correction factor was validated to be within 1% of the true correction factor using the 186 and 205 keV gamma-lines of ^{235}U. The

correction factor magnitude at 186 keV was approximately 3.1. This multiplicative factor generated a maximum additional uncertainty of 3.1% at 186 keV. Below 186 keV, the self-shielding correction factor was purely modeled. Given the magnitude of the uncertainty at 186 keV, the uncertainty below 186 keV was expected to increase to its maximum model predicted value of 4.5% at 100 keV rapidly. The uncertainty in the self-shielding correction factor was doubled because of its model based origins to ensure the quoted uncertainty was not smaller than the true uncertainty. The doubling of the self-shielding uncertainty was also done to encapsulate any unaccounted for sources of error up to 5%.

The flux and cross-section weighted average neutron energies for each actinide were 14.24, 14.14, and 10.96 MeV for ^{232}Th, ^{238}U, and ^{235}U, respectively. The flux covariance matrix used for the uncertainty quantification is shown in Fig. 5.9. This covariance matrix was generated using the Gaussian formalism referenced in Ref. [177]. The user defined inputs for the covariance estimate of the flux were FCVX=0.03, FCHN=1, and the error distribution provided in table 5.2. The cross-section covariance matrix for ^{235}U was provided by the International Reactor Dosimetry and Fusion File [186, 187] and is shown in Fig. 5.10. The uncertainty in the fission rate of ^{232}Th was dominated by the uncertainty in the cross-section. The fission threshold of ^{232}Th helped improve the overall uncertainty but the larger error in the cross-sections overwhelmingly dominated the uncertainty. In the case of ^{235}U the uncertainty was dominated by the uncertainty in the flux. The weak definitive characterization of the thermal neutron flux degraded the uncertainty in the fission rate of ^{235}U.

Table 5.2: STAYSL PNNL error distribution estimate for Gaussian formalism based flux covariance matrix generation.

Energy Range	%Uncertainty
0—0.1 keV	80%
0.135—15 keV	50%
19 keV—14.1 MeV	20%
14.1—20 MeV	10%

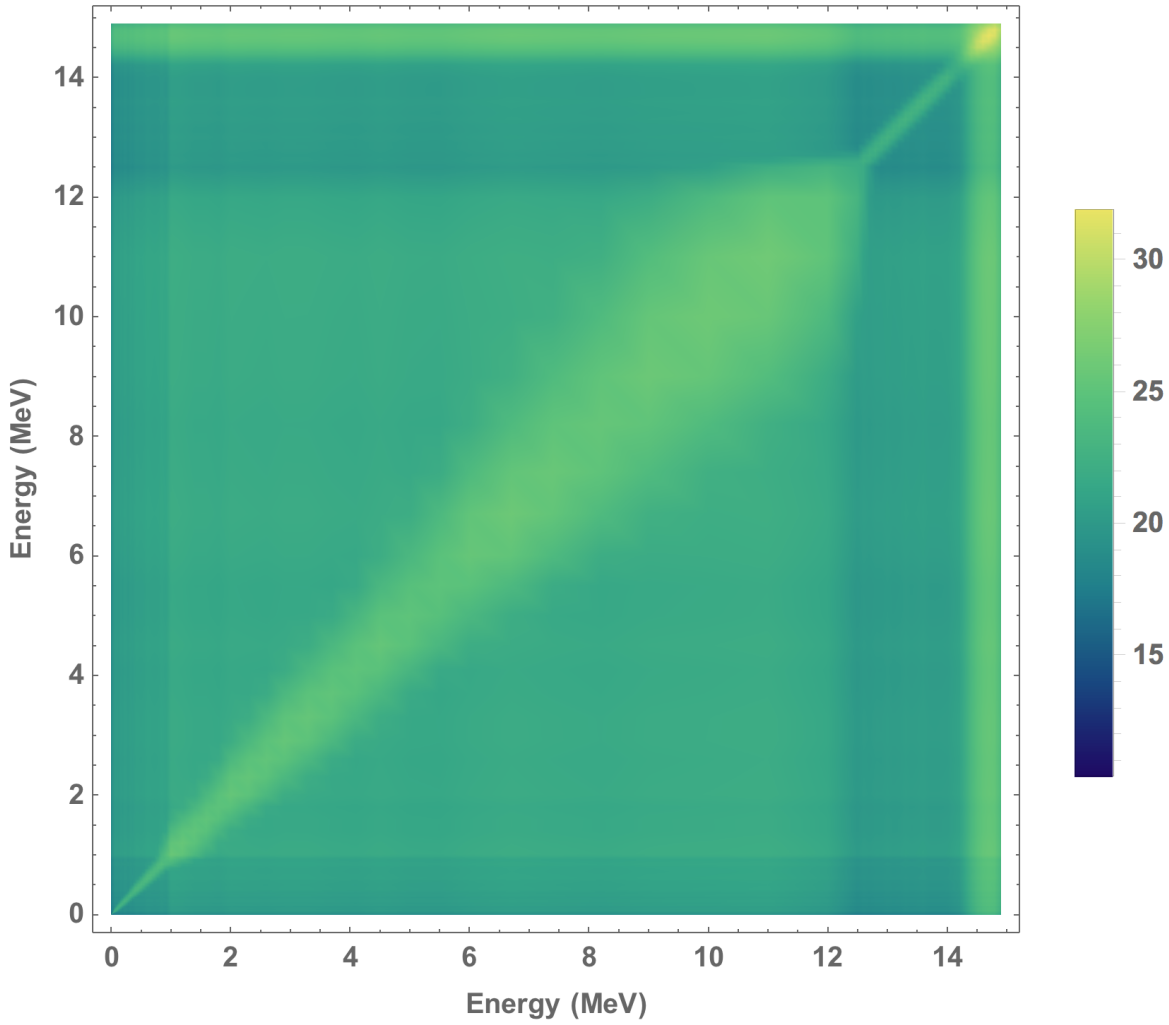

Figure 5.9: Density distribution of the flux covariance matrix. The logarithm of flux was used to emphasize the correlation of the 14 MeV peak with the lower energy range.

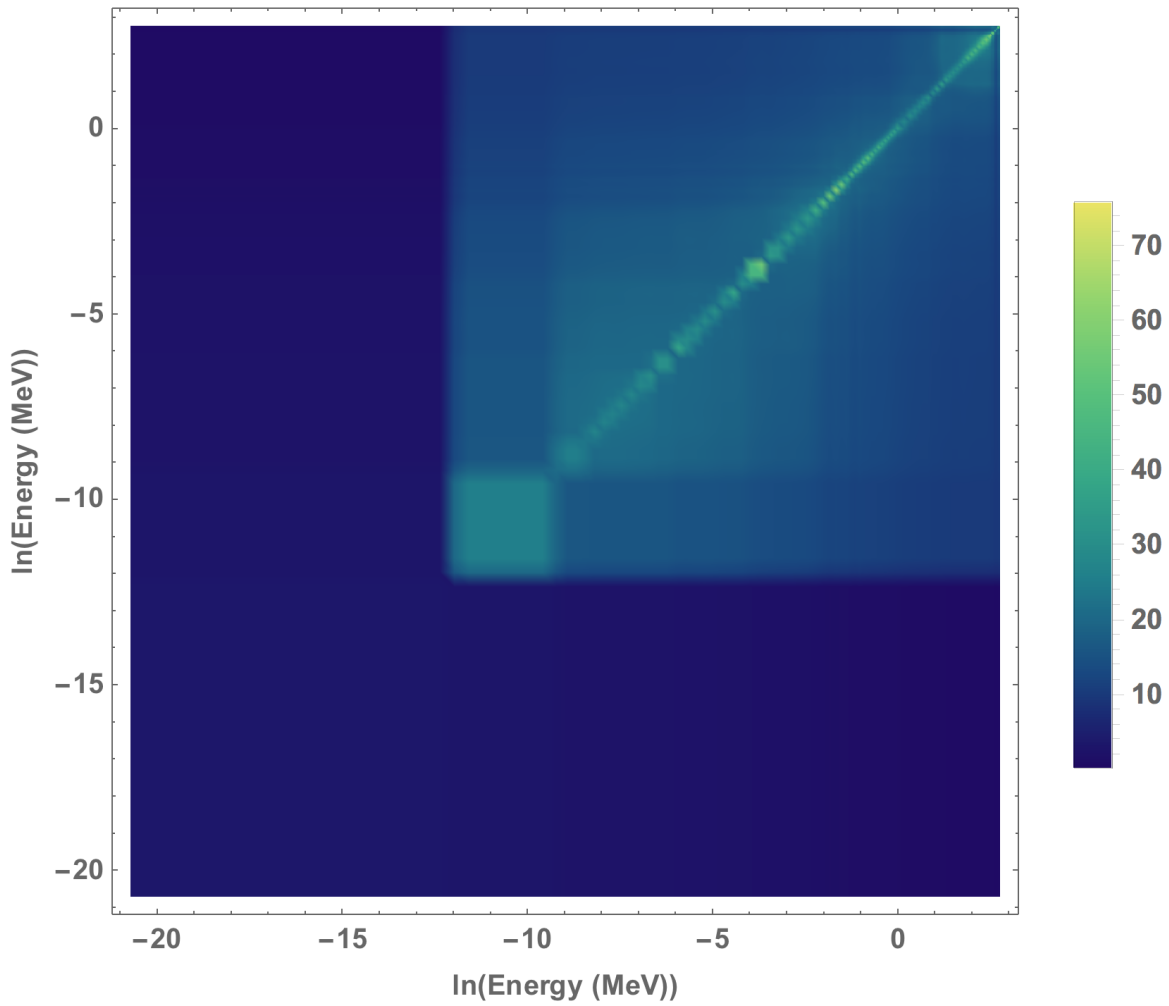

Figure 5.10: Density distribution of the cross-section covariance matrix for ^{235}U. The covariance uncertainties were multiplied by 10^{54} or $10^{27} \cdot 10^{27}$ i.e. millibarns squared.

Table 5.3: Sources of uncertainty in the fission yield measurements. The CF_{SS} uncertainty reached a maximum of 10% below 250 keV. The fission rate uncertainty for ^{235}U is elevated because of additional fissions at lower energy. The uncertainty for the fission rates was determined from the product of the cross-section and flux covariance matrices.

Source	1σ % Uncertainty	Description
$\varepsilon_e + \varepsilon_w + \varepsilon_v$	1.1%	Eckert & Ziegler [2]
$T_{1/2}$	∼1—10%	ENDF/B-VII.1 [185]
Γ	∼0.1—5%	ENDF/B-VII.1 [185]
τ	0.1≫	National Instruments [2, 174]
Δ	0.1>	XIA Pixie-4 [2, 174]
m	0.1>	Mettler & Toledo scale
CF_{SS}	∼1-10%	GEANT4
CF_{DT}	∼0.5-2%	^{235}U mass ratio
$\sigma_f\phi$ ^{232}Th	9.23%	STAYSL PNNL [177, 2]
$\sigma_f\phi$ ^{238}U	7.03%	STAYSL PNNL [177, 2]
$\sigma_f\phi$ ^{235}U	10.75%	STAYSL PNNL [177, 2]

$$\frac{\ln(2)\cdot C\cdot CF_{SS}\cdot CF_{DT}}{(\varepsilon_e+\varepsilon_w+\varepsilon_v)\cdot\Gamma\cdot\sigma_f\phi\cdot N_A\cdot m\cdot T_{1/2}} \tag{5.1}$$

$$= Y_1\cdot\int_t^{t+\Delta} D_1(\tau,f)df \tag{5.2}$$

$$= Y_1\cdot(1-e^{-\lambda\tau})\cdot(1-e^{-\lambda\Delta})\cdot e^{-\lambda t} \tag{5.3}$$

In some circumstances, the parent isotope of an identified fission product had a half-life comparable to the daughter. In such circumstances, the second-order Bateman (D_2) equation was needed to measure the cumulative yield of the parent (Y_1) and independent yield of the daughter (Y_2). The derivation of the second-order Bateman equation can be made using the law of radioactive decay and is found in Ref. [**?**]. One such example is ^{144}La. ^{144}La has a 40.8 second half-life and its parent barium-144 has a 11.5 second half-life [188]. The feeding of ^{144}La from barium-144 decay was clearly visible in the extracted peak areas spanning the counting time, as shown in Fig. 5.11. For cases like that shown in Fig. 5.11, the D_2 equation was needed to accurately fit the data.

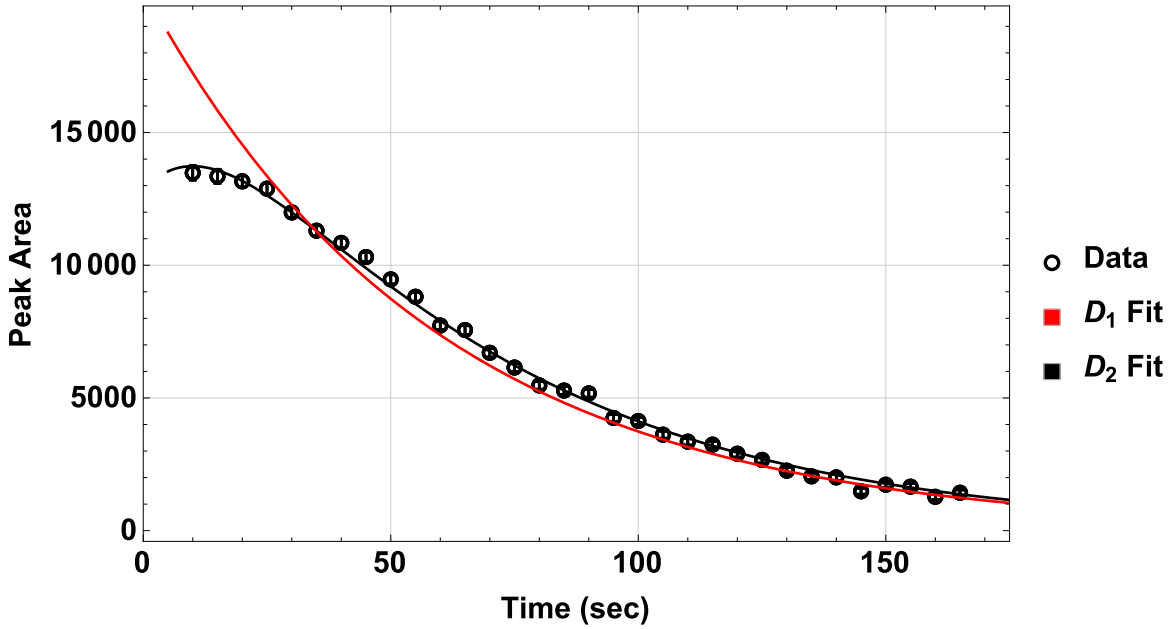

Figure 5.11: Peak areas from the 397 keV gamma-line of ^{144}La, corrected for dead-time and self-shielding and fit using the D_1 equation (red) and the D_2 equation (black). Deviation at early times is indicative of in-growth from a parent radionuclide with a half-life comparable to 10 seconds.

$$\frac{\ln(2) \cdot C \cdot CF_{SS} \cdot CF_{DT}}{(\varepsilon_e + \varepsilon_w + \varepsilon_v) \cdot \Gamma \cdot \sigma_f \phi \cdot N_A \cdot m \cdot T_{1/2}} = \int_t^{t+\Delta} D_2(Y_1, Y_2, \tau, f) df \tag{5.4}$$

Both Eq. (5.3) and (5.4) were taken from references [182, 183, 147, 184] and modified for fission yield measurement.

5.4 Results

A total of 29 fission products were measured from each target. Agreement between the measured values and those published in the ENDF/B-VII.1 varied: Of the 101 measurements made, 62 fell within one-sigma of ENDF/B-VII.1, 82 within 2σ, and 94 within 4σ. It is important to note that many of the short-lived fission products presented in Tab. 5.6—5.8

have never before been measured using 14.3(3) MeV neutron-induced fission. A standard deviation of ≈300 keV was estimated from STAYSL PNNL adjusted MCNP simulations, the angular spread of neutron energies due to the deuterium-tritium fusion reaction kinematics within the neutron generator, and from other, similar source characterizations listed in the Experimental Nuclear Reaction Database (EXFOR) [189]. The energy and neutron spectrum are referenced from [173] and [2]. The majority of fission yield measurements conducted with neutrons at this energy were performed on long-lived radionuclides, as discussed in Sec. **??**. Many of the fission yield values from ENDF/B-VII.1 [185] and provided in Tab. 5.6—5.8 are not from measurements. They were produced by extrapolating from long-lived fission product fission yield measurements using the charge distribution model [**?** 112, 114, 190, 191]. This model assumes that the yields along the isobar chains are Gaussian; indeed, Wahl and others describe the assumptions from this model in detail [192, 191]. Deviation from this model can be treated one of several ways: 1) the nuclear data used to derive the fission yield estimate must be reviewed, 2) misidentification or interference has contaminated the results, and 3) provided the other two are false, the fission yield deviates from the accepted theoretical model of the fission distribution. Each of these assumptions is valid, and many of the radionuclides provided in Tab. 5.6—5.8 are not as well-known as many of the longer-lived radioisotopes. Gamma-lines, free of interference, were selected for each measurement. As described, available searchable data sets within JANIS 4.0 and Nudat 2.0 were used to identify radioisotopes from the coincidence plane and rule out interferences. Each measurement is discussed and relevant information is included to assist the reader in comparing the results with the literature.

5.4.1 Arsenic and Selenium

Measurements of these radionuclides fell within 2σ of the ENDF/B-VII.1 predictions for all targets. The largest discrepancy between the measurement and ENDF/B-VII.1 was the estimate of the yield for ^{84}As from ^{232}Th. The yield measurements, taken over-time,

showed excellent agreement and indicated no signs of interference from the gamma-gamma coincidence plane. Fig. 5.12 illustrates the estimated fission yield from the 1454.55 keV gamma-line of ^{84}As over time from the ^{232}Th data and Fig. 5.13 is the temporal measurement of the fission yield of ^{84}As from all three actinides. Fission yield measurements from ^{232}Th of ^{86,87,88}Br; ^{89,90,92}Kr; ^{94,95}Sr; ^{138,139}Xe; ^{140}Cs; and ^{144}La all agreed to within 10% of the ENDF/B-VII.1 values. Based on this agreement, the true fission yield of ^{84}As from 14.3 MeV neutron-induced fission has been suggested to be a factor of two higher than the ENDF/B-VII.1 estimate of 0.46(29)% . The new suggested fission yield is 0.99(8)%.

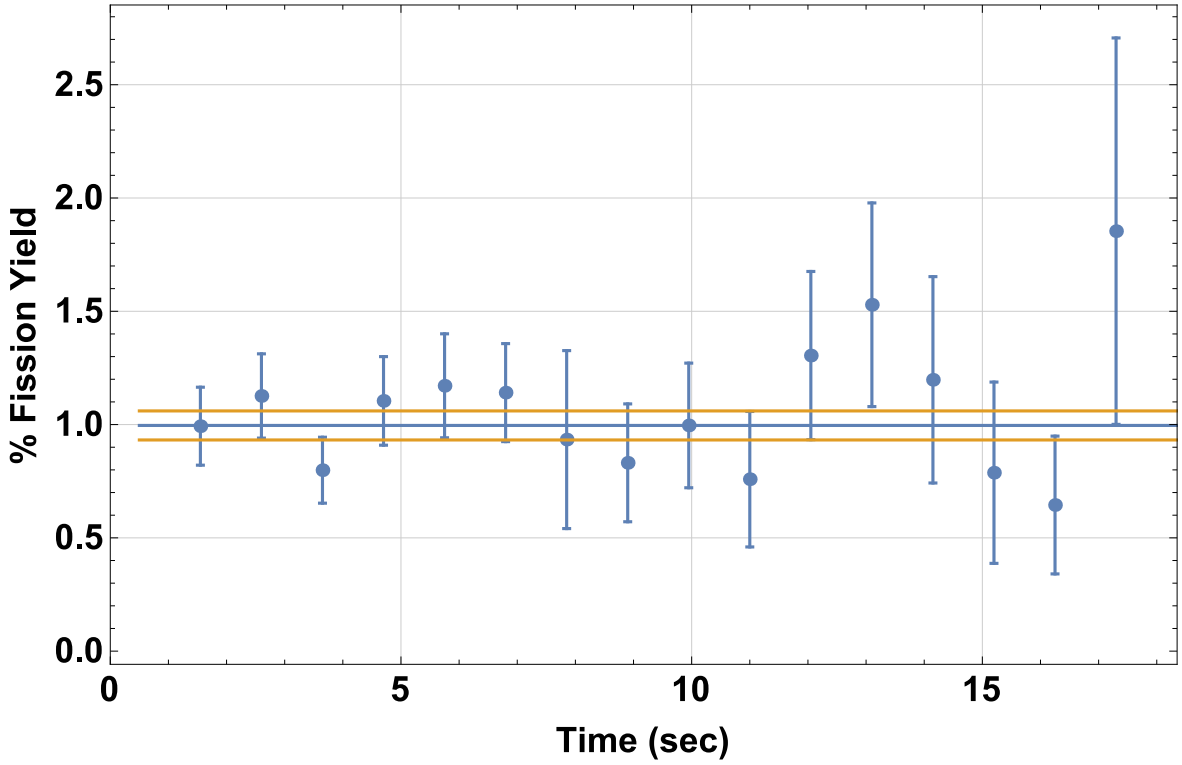

Figure 5.12: Fission yield estimate of ^{84}As over time acquired from ^{232}Th using the 1454.55 keV gamma-line. The blue line centered between the two orange lines is the fitted estimate, and the two orange lines are the 1σ prediction window. This particular estimate used an even finer time-binning structure to emphasize the temporal agreement.

Estimates of the fission yield made for ^{86}Se from the 2441.1 keV gamma-line and using the D_2 equation fitted to the 1564.6 keV gamma-line of ^{86}Br were within 2σ of each other for all the targets. Provided the gamma branching ratios and half-life are correct, and that the agreement between ENDF/B-VII.1 and the measured values for bromine, krypton, strontium,

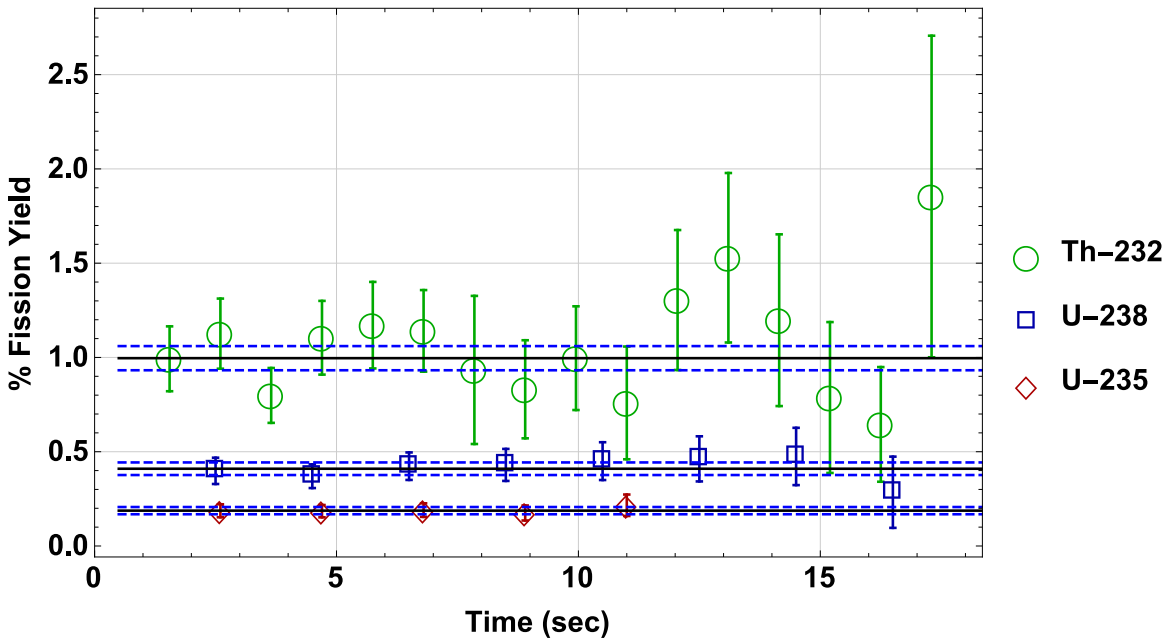

Figure 5.13: Fission yield estimate of ^{84}As over time acquired from the different actinide targets using the 1454.55 keV gamma-line. The black center-line of each target is the fission yield estimate and the dashed blue lines are the 1σ prediction window.

xenon, and some of the longer-lived lanthanides are indicative of a reliable analysis, a new fission yield for ^{86}Se has been made for each target. The suggested values from this work are 2.26(10)%, 0.60(3)%, and 0.37(2)% for ^{232}Th, ^{238}U, and ^{235}U, respectively. Fig. 5.14 shows the estimated fission yield from the 2441.1 keV gamma-line of ^{86}Se over time from the ^{232}Th data and Fig. 5.15 is the temporal measurement of the fission yield of ^{86}Se from all three actinides. Though the 2441.1 keV gamma-line of ^{86}Se is higher than the last efficiency calibration point at 1836 keV from ^{88}Y, the efficiency was assumed to be linear in log-log space beyond 1836 keV [154]. The uncertainty for the efficiency at 2441.1 keV was $\approx$2% (factor of two larger) because of the extrapolation. The measurement of the fission yield of ^{86}Se made from the 1564.6 keV gamma-line of ^{86}Br, however, was within the calibrated energy range and agreed well with the measurement from 2441.1 keV.

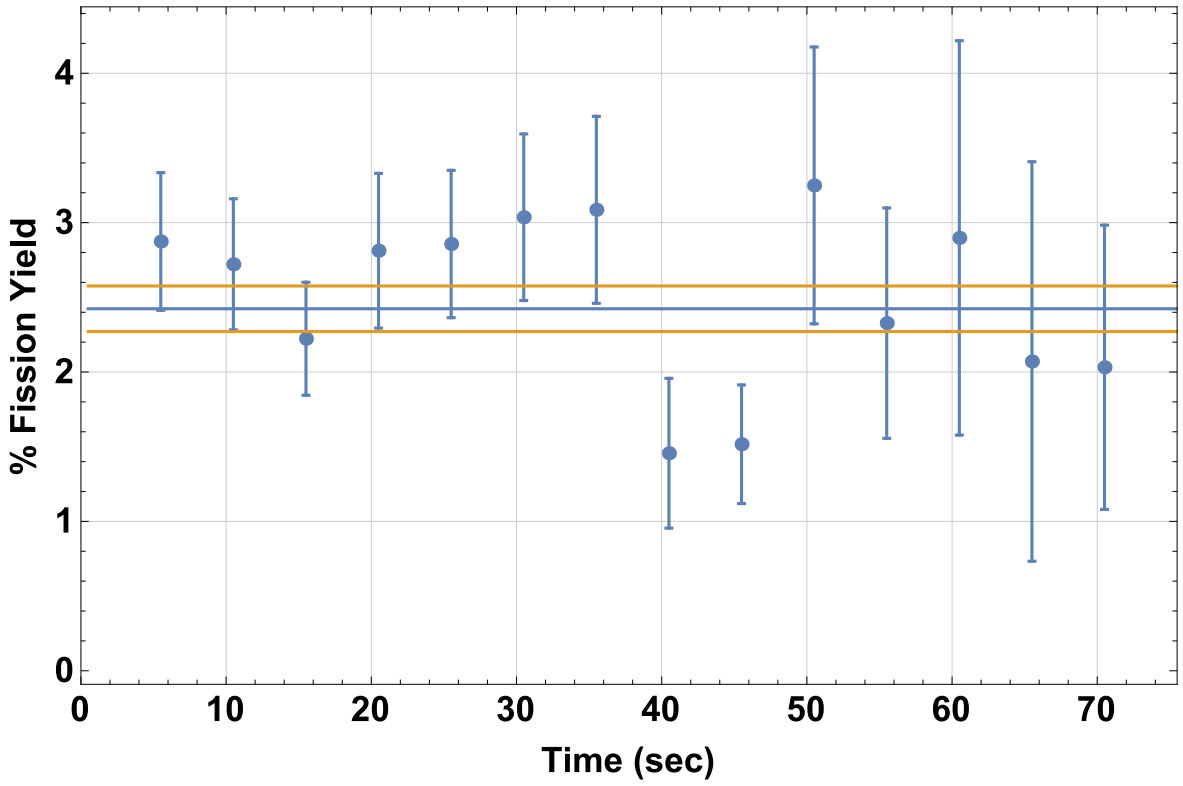

Figure 5.14: Fission yield estimates, mean, and 1σ sigma confidence for ^{86}Se over time acquired from ^{232}Th using the 2441.1 keV gamma-line. The blue line centered between the two orange lines is the fitted estimate, and the two orange lines are the 1σ prediction window. This particular estimate used an even finer time-binning structure to emphasize the temporal agreement.

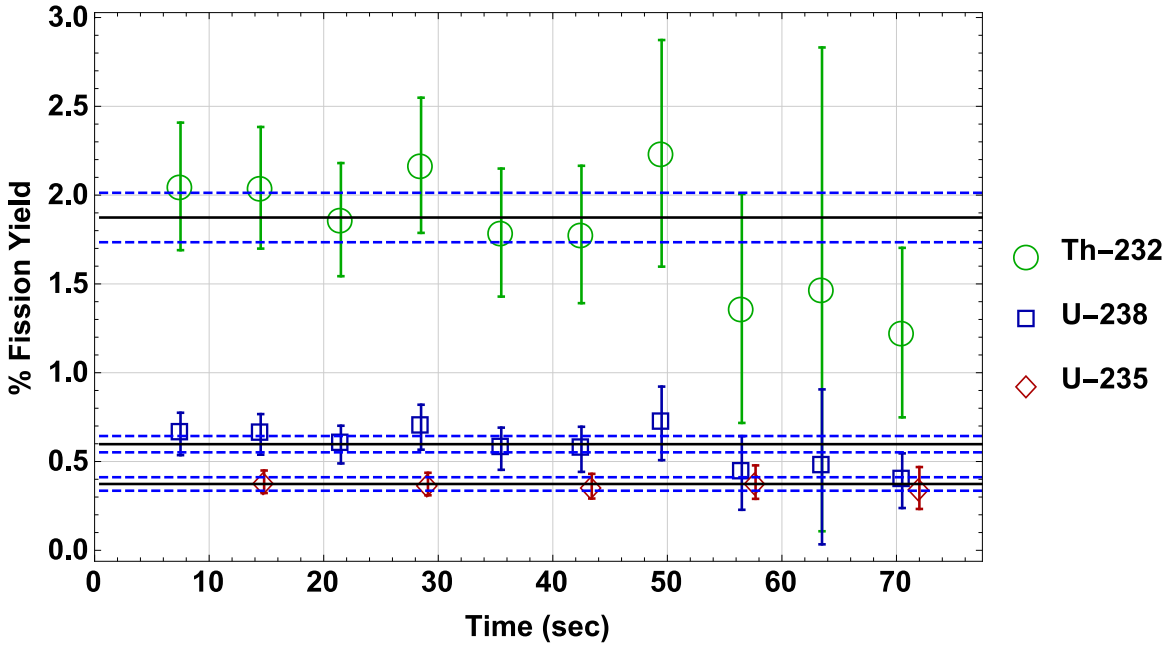

Figure 5.15: Fission yield estimates, mean, and 1σ sigma confidence for ^{86}Se over time acquired from each actinide using the 2441.1 keV gamma-line. The blue line centered between the two orange lines is the fitted estimate, and the two orange lines are the 1σ prediction window.

5.4.2 Bromine and Krypton

The fission yield measurements of bromine showed mixed agreement with ENDF/B-VII.1. In the case of ^{232}Th, all measurements agreed with ENDF/B-VII.1, whereas for the depleted-uranium target, ^{87}Br, one of the most important delayed neutron emitters, was much higher than the ENDF/B-VII.1 value. For ^{235}U, overall agreement was better than ^{238}U but the yield to ^{87}Br was measured to be 28% higher than ENDF/B-VII.1 and ^{88}Br 42% lower. ^{89,90,92}Kr agreed well with the measured results for ^{232}Th and were consistently high for the uranium targets; however, fission product yield ratio measurements made by Bocquet [193] agreed with the results of this analysis, as shown in Tab. 5.4. Good agreement between the krypton ratios indicates that gas losses from the target were not statistically significant.

Table 5.4: Comparison of fission yield ratios of krypton.

Target	^{90}Kr/^{92}Kr Measured	^{90}Kr/^{92}Kr Bocquet	^{90}Kr/^{89}Kr Measured	^{90}Kr/^{89}Kr Bocquet
^{232}Th	2.38(18)	2.20(10)	0.99(9)	0.90(4)
^{238}U	1.38(14)	1.42(7)	0.91(14)	1.02(3)
^{235}U	3.61(33)	3.58(15)	0.81(12)	0.85(2)

5.4.3 Rubidium and Strontium

Fission yield estimates from rubidium and strontium all fell within 2σ of the ENDF/B-VII.1 estimates. ^{94}Rb and ^{96}Sr measured from ^{232}Th had the worst agreement and were about 30% lower than the ENDF/B-VII.1 values. The lower measured yields to ^{94}Rb and ^{96}Sr suggest that the neutron multiplicity as a function of atomic weight within this region may be higher than expected for ^{232}Th [194], that the charge distribution model over-estimates for ^{232}Th fission, or that the centroid of the low atomic weight mass yield curve might be lower than was estimated in ENDF/B-VII.1. The last suggestion might also explain the higher yield to ^{84}As observed. No other fission yield measurements for ^{232}Th have been made for ^{94,95,96}Sr, and ^{94}Rb. Many of the fission yield estimates for ^{238}U were compared with results from Campbell in Ref. [195]. The measured independent yield of ^{94}Sr from ^{238}U in this work are in excellent agreement with results from Campbell; however, the comparison is not ideal. Campbell's work used a thermal reactor source spectrum, not a purely 14 MeV neutron source, nor was the source spectrum explicitly described as it was for this work in Ref. [2]. Regardless, the measurements from Ref. [195] were suggested by EXFOR and are the closest available comparison to the measurements made in this work [189]. The measured results for the strontium and rubidium isotopes were in good agreement with the charge distribution models and might serve as an excellent set of gamma-lines to observe directly from a nuclear detonation for nuclear forensics.

5.4.4 Yttrium and Zirconium

Two new fission yields of the metastable states of ^{96}Y and ^{97}Y are presented for ^{232}Th, ^{238}U, and ^{235}U. These estimates were generated using gamma peaks with limited interference. Peaks were free of interference because of their high energies of 1750 and 1103 keV and strong specific activity due to their short half-lives of 9.6 and 1.17 seconds for the metastable states of ^{96}Y and -97, respectively [196, 197].

An analysis of yttrium and ^{99}Zr required a more elaborate analysis method. Data analysis of this parent-daughter pair required the use of the D_2 equation when analyzing ^{99}Zr's gamma-lines. Although it was assumed that the temporal adjustment to the ^{99}Zr gamma-lines from ^{99}Y feeding would dramatically change their time-dependence, limited sensitivity of the second order function to the ^{99}Y feeding effect was observed. The cumulative yield to ^{99}Y, observed from the 724 keV gamma-line, agreed within one-sigma of the ENDF/B-VII.1 evaluation for ^{232}Th and ^{238}U and 1.27 sigma for ^{235}U. The yield estimate acquired using the D_2 equation fitting to gamma-lines of ^{99}Zr roughly agreed using the 469 keV gamma-line. Measurements were more difficult to obtain from the 546 keV gamma-line of ^{99}Zr. Several peaks were convolved around this gamma-line, making it difficult to reliably extract photo-peak areas.

5.4.5 Tellurium and Iodine

^{136}Te was found to be in agreement with ENDF/B-VII.1 for both uranium targets. The 2077 keV gamma-line of ^{136}Te is far from background contamination, free of interference, suffers from limited gamma self-shielding, and has a half-life that is long enough that dead-time effects at early times are somewhat mitigated. Measurements of ^{136}Te and the ground and first metastable states of ^{136}I were in keeping with the expectation that the cumulative fission yield estimate of the ground state of ^{136}I should be larger than tellurium; however, measurements of the yields to the ground and metastable states of ^{136}I did not agree with ENDF/B-VII.1. The isomer ratio of these radionuclides suggested the yield to the isomer

state was higher than the ground state, not in keeping with the expected behavior of the ground state yield being higher. The yield to the metastable state relative to the ground state of ^{136}I was larger. The ground and metastable state yields of ^{136}I were made by fitting the time-varying peak area of the 1313 keV gamma-line with the sum of two D_1 equations. The half-lives were assumed to be different enough for this approach to be sensitive to the two decaying radionuclides. However, during the analysis, the half-life of the meta-stable state nearly matched the observed time-dependence of the peak. The lack of observed ground-state ^{136}I is not clear at this time.

5.4.6 Xenon and Cesium

^{138}Xe, the longest lived isotope measured, showed excellent agreement with ENDF/B-VII.1 in all three cases, but the statistics of the measurement were far worse than the ENDF/B-VII.1 evaluation, as expected. The irradiation time used for this work was not designed to probe radionuclides in this time regime; nevertheless, the 1768 keV gamma-line of ^{138}Xe was clearly present throughout the experiment for all three targets. ^{139}Xe showed reasonable agreement but was consistently higher than ENDF/B-VII.1 for the uranium measurements. Peak area extraction for ^{89}Kr and ^{139}Xe were performed simultaneously. The 219 and 221 keV gamma-lines of ^{89}Kr and ^{139}Xe, respectively, were convolved, as shown in Fig. 5.16. In addition to multi-peak fitting, the low energy nature of these two gamma-lines increases the likelihood that they suffer from interference with other low emitters within this energy regime. Fig. 5.16 illustrates the complexity of the region where ^{139}Xe was measured. ^{140}Xe agreed well with ENDF/B-VII.1 for ^{238}U but exhibited lower yields relative to ENDF/B-VII.1 for ^{232}Th and ^{235}U.

Fission product yield ratios measured from this work were compared with Bocquet's measurements and are provided in Tab. 5.5. The poor agreement between the measured results and ENDF/B-VII.1 for ^{140}Xe is likely the result of poor counting statistics. The 1413 keV gamma-line was very weak in the data. Peak fitting was forced in some cases to extract

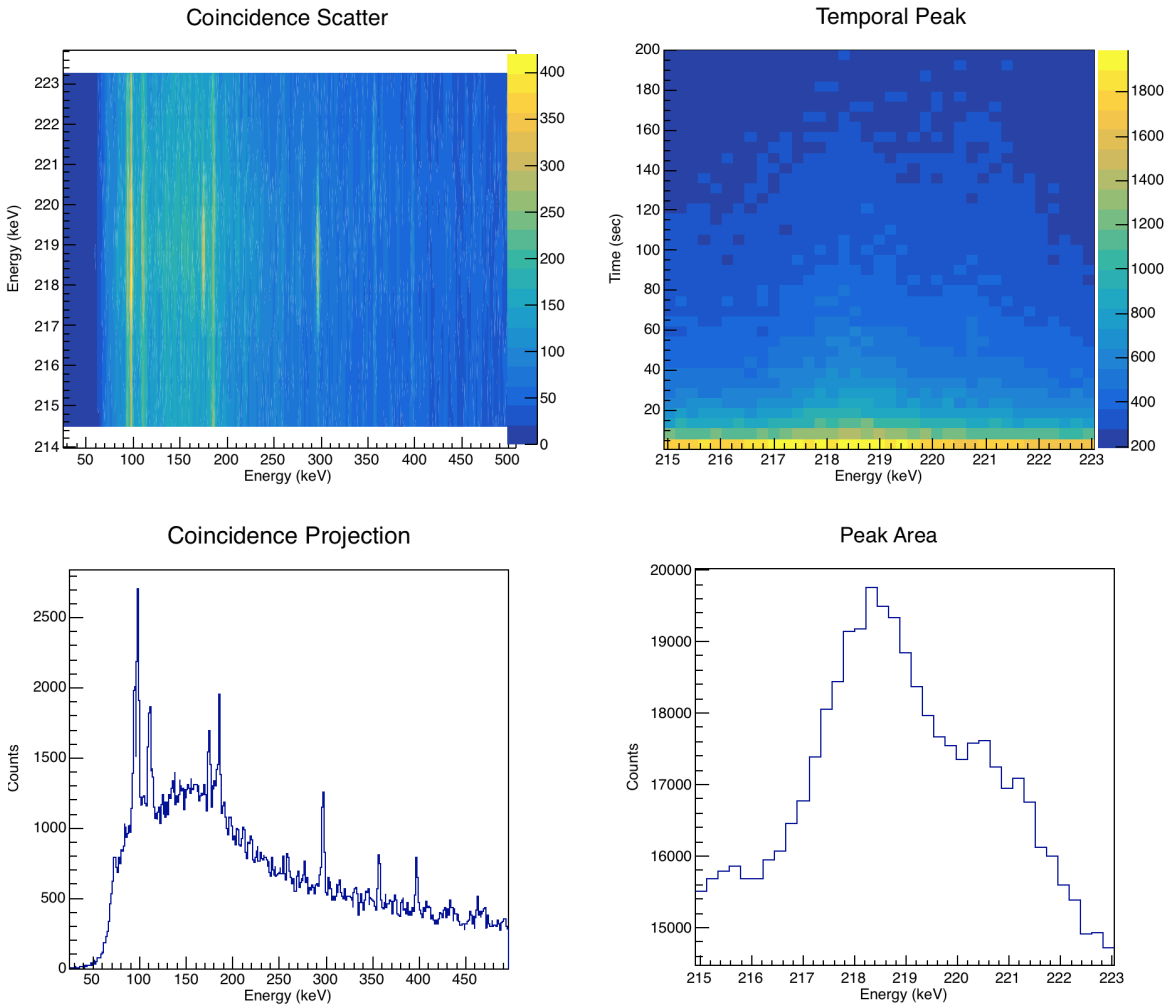

Figure 5.16: Convolved photo-peaks of ^{139}Xe at 218.6 keV and ^{89}Kr at 220.95 keV. The prominent coincidences between the 218.6, 174.9, and 296.5 keV gamma-lines of ^{139}Xe can be seen in the coincidence scatter plot (top-left). It is not visible in the figure but the coincidence between 220 and 1472 keV of ^{89}Kr was also present within this spectrum.

peak areas for the estimate (see Fig. 5.17).

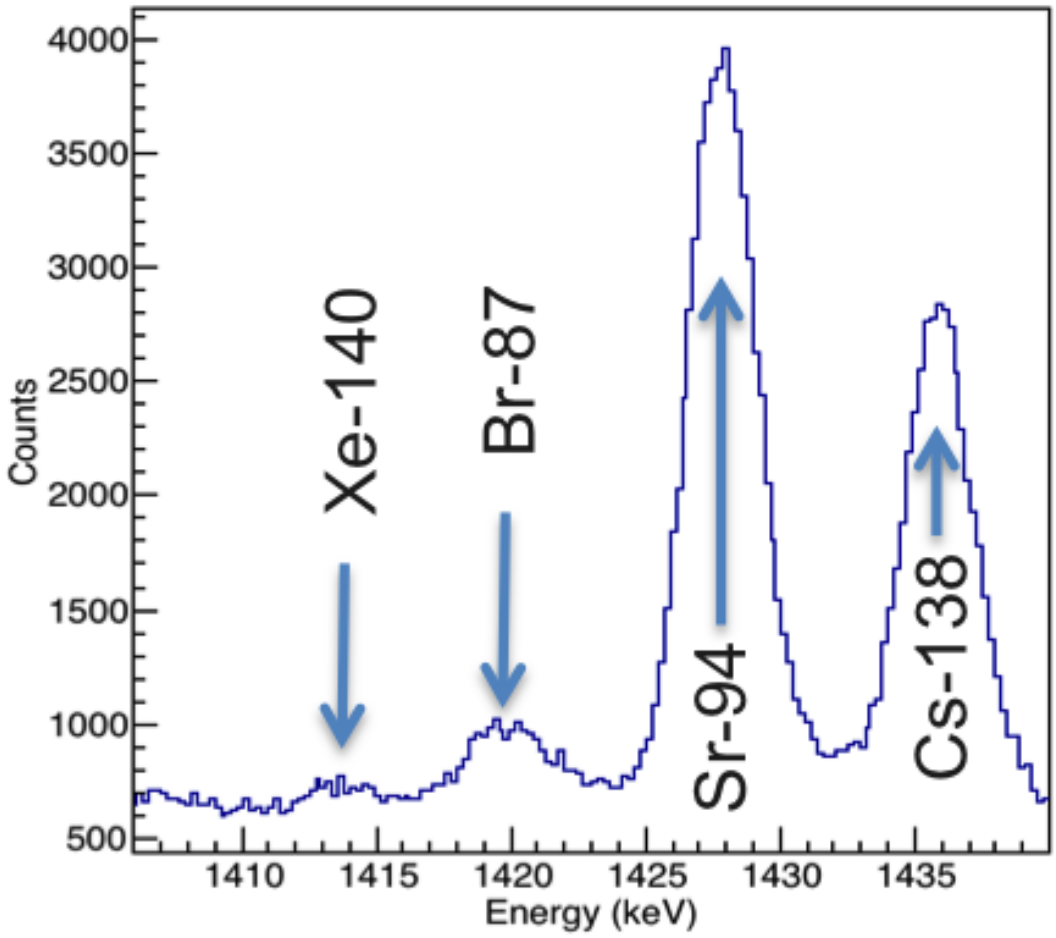

Figure 5.17: Singles spectrum of all recorded events over the 200-second counting window. Several measured fission products and the peak region where ^{140}Xe was measured from are listed.

Table 5.5: Comparison of fission yield ratios from xenon as measured in this work and by Bocquet.

Target	^{138}Xe/^{139}Xe Measured	^{138}Xe/^{139}Xe Bocquet	^{138}Xe/^{140}Xe Measured	^{138}Xe/^{140}Xe Bocquet
^{232}Th	0.97(7)	1.05(3)	1.94(25)	1.31(2)
^{238}U	1.21(18)	1.15(4)	2.01(25)	1.54(6)
^{235}U	1.13(17)	1.62(8)	5.29(83)	3.40(13)

5.4.7 Barium and Lanthanum

^{144}La was easily observed from the 397 keV gamma-line and showed multiple coincidences at 1524, 1431, 968, 845, 735, 585, 541, and at several other minor coincident lines. The measured fission yield from the 397 keV gamma-line was in agreement with ENDF/B-VII.1's estimated value using the D_2 equation, as illustrated in Fig. 5.11. Because of the more complex temporal behavior of the 397 keV gamma-line, an estimate of the cumulative yield of ^{144}Ba and an independent yield of ^{144}La was generated. All fission yields listed in Tab. 5.6—5.8 are cumulative yields. For linked parent-daughter decay chains, the independent yield is the difference in the two cumulative yields of the parent and daughter. The ground and metastable state for ^{146}La was measured from the 258 keV gamma-line in the same way as the ^{136m}I and ^{136}I pair. This line suffers from interference from the long-lived ^{138}Xe; however, the additional counts added from decay of ^{138}Xe were treated as background, given that the gamma-emission rate from ^{138}Xe relative to ^{146}La was roughly constant. Deconvolution of two yields from a single gamma-line was done by fixing the decay constant of each D_1 equation in the sum of the two and fitting the time-dependence of the gamma-line. Estimates obtained in this way yielded results with weaker statistics; however, no true measurement of these yields has been made. A comparison of the results measured in this work to those provided by ENDF/B-VII.1 indicate that the isomer ratio used to split the yield for ^{146}La was relatively close to the true ratio.

Table 5.6: Measured fission yields from ^{232}Th and additional data relevant to the respective radioisotopes. The columns of the table are: atomic weight, atomic mass, half-life and uncertainty, gamma-line energy used for the measurement, branching ratio, the ENDF/B-VII.1 estimated fission yield and uncertainty, the measured fission yield and uncertainty, percent difference from ENDF/B-VII.1, ratio of the measured uncertainty divided by the uncertainty quoted from ENDF/B-VII.1, and the number of standard deviations the measured result is from the ENDF/B-VII.1 value using the ENDF/B-VII.1 uncertainty.

A	Z	Iso	$T_{1/2}$ (sec)	E (keV)	I (%)	Meas. FY (%)	$\sigma_{Meas.}$ Meas. FY	ENDF FY (%)	$1\sigma_{ENDF}$ ENDF FY	% Difference	Ratio of $\frac{\sigma_{Meas.}}{\sigma_{ENDF}}$	Difference/σ_{ENDF}
84	33	^{84}As	4.2(5)	1454.55(10)	89.0(82)	0.99%	0.12%	0.46%	0.29%	116.24%	2.38	1.82
86	34	^{86}Se	14.3(3)	2441.1(3)	43.00(454)	2.42%	0.30%	4.03%	0.93%	-39.97%	3.14	1.74
86	34	^{86}Se	14.3(3)	1564.64(14)		2.07%	0.29%	4.03%	0.93%	-48.51%	3.19	2.11
86	35	^{86}Br	55.0(8)	1564.64(14)	65.0(77)	3.96%	0.42%	4.62%	0.74%	-14.46%	1.75	0.90
87	35	^{87}Br	55.65(13)	1419.71(7)	22.0(15)	4.18%	0.49%	4.36%	0.35%	-4.23%	0.71	0.53
88	35	^{88}Br	16.29(6)	775.28(6)	67(5)	3.20%	0.37%	3.55%	0.82%	-9.91%	2.18	0.43
89	36	^{89}Kr	189.0(24)	220.948(9)	20.10(170)	5.37%	0.67%	5.81%	0.35%	-7.57%	0.52	1.26
90	36	^{90}Kr	32.32(9)	1118.69(5)	39.00(312)	5.33%	0.66%	5.54%	1.27%	-3.80%	1.94	0.17
92	36	^{92}Kr	1.84(8)	1218.6(1)	59.61(385)	2.31%	0.30%	2.36%	0.14%	-2.22%	0.48	0.37
94	37	^{94}Rb	2.702(5)	836.9(1)	61(4)	2.34%	0.29%	3.56%	0.82%	-34.43%	2.85	1.50
94	37	^{94}Rb	2.702(5)	1577.5(2)	22.27(183)	2.45%	0.35%	3.56%	0.82%	-31.17%	2.37	1.36
94	38	^{94}Sr	75.3(2)	1427.7(1)	94.2(9)	4.80%	0.53%	5.25%	0.84%	-8.56%	1.58	0.54
95	38	^{95}Sr	23.9(14)	685.6(2)	22.60(120)	4.30%	0.53%	4.42%	0.71%	-2.70%	1.33	0.17
96	38	^{96}Sr	1.07(1)	809.40(3)	71.91(256)	2.37%	0.31%	3.01%	0.48%	-21.32%	1.57	1.33
96	39	^{96m}Y	9.6(2)	1750.6(2)	88(??)	0.49%	0.07%	0.69%	0.31%	-29.91%	4.35	0.66
97	39	^{97m}Y	1.17(3)	1103.0(2)	92.35(199)	0.81%	0.12%	0.75%	0.48%	7.81%	4.13	0.12
99	39	^{99}Y	1.47(7)	724.4(2)	17.06(203)	1.45%	0.32%	1.51%	0.35%	-4.17%	1.1	0.18
99	39	^{99}Y	1.47(7)	469.137(13)		1.72%	0.28%	1.51%	0.35%	13.82%	1.26	0.60
99	39	^{99}Y	1.47(7)	546.13(3)		0.47%	0.19%	1.51%	0.35%	-68.83%	1.84	2.99
99	40	^{99}Zr	2.1(1)	469.137(13)	55.20(220)	2.38%	0.29%	2.02%	0.47%	17.38%	1.6	0.76
99	40	^{99}Zr	2.1(1)	546.13(3)	48.29(285)	2.23%	0.26%	2.02%	0.47%	10.26%	1.79	0.45
136	52	^{136}Te	17.5(2)	2077.9(3)	22.37(250)	1.26%	0.19%	2.16%	0.50%	-41.64%	2.62	1.81
136	53	^{136g}I	83.4(10)	1313.02(1)	66.70(0)	0.68%	0.50%	3.91%	0.63%	-82.69%	1.26	5.17
136	53	^{136m}I	46.9(1)	1313.02(1)	100(0)	1.96%	0.29%	1.78%	0.41%	10.22%	1.43	0.44
138	54	^{138}Xe	844.8(48)	1768.26(13)	16.73(68)	5.00%	0.62%	5.45%	0.33%	-8.15%	0.53	1.36
139	54	^{139}Xe	39.68(14)	218.59(3)	56(6)	5.15%	0.57%	4.82%	0.29%	6.89%	0.51	1.15
140	54	^{140}Xe	13.6(1)	1413.66(10)	12.20(171)	2.66%	0.40%	3.73%	0.30%	-28.68%	0.74	3.59
140	55	^{140}Cs	63.7(3)	602.25(5)	53.30(256)	5.87%	0.65%	5.84%	0.47%	0.46%	0.72	0.06
142	55	^{142}Cs	1.684(14)	359.598(14)	27.20(274)	3.56%	0.46%	3.98%	0.91%	-10.54%	1.98	0.46
143	56	^{143}Ba	14.5(3)	798.79(2)	15.6(18)	5.47%	0.68%	4.90%	0.78%	11.48%	1.16	0.72
144	56	^{144}Ba	11.5(2)	397.440(9)		3.11%	0.35%	3.62%	0.83%	-14.15%	2.38	0.62
144	57	^{144}La	40.8(4)	397.440(9)	94.3(16)	3.82%	0.41%	4.20%	0.67%	-9.25%	1.66	0.58
146	57	^{146m}La	10(1)	258.42(5)	95.25(675)	0.71%	0.13%	0.66%	0.42%	8.08%	3.15	0.13
146	57	^{146}La	6.27(10)	258.47(6)	63.7(30)	1.21%	0.22%	1.58%	1.01%	-23.92%	4.53	0.37

Table 5.7: Measured fission yields from ^{238}U and additional data relevant to the respective radioisotopes. The columns of the table are: atomic weight, atomic mass, half-life and uncertainty, gamma-line energy used for the measurement, branching ratio, the ENDF/B-VII.1 estimated fission yield and uncertainty, the measured fission yield and uncertainty, percent difference from ENDF/B-VII.1, ratio of the measured uncertainty divided by the uncertainty quoted from ENDF/B-VII.1, and the number of standard deviations the measured result is from the ENDF/B-VII.1 value using the ENDF/B-VII.1 uncertainty.

A	Z	Iso	$T_{1/2}$ (sec)	E (keV)	I (%)	Meas. FY (%)	$\sigma_{Meas.}$ Meas. FY	ENDF FY (%)	$1\sigma_{ENDF}$ ENDF FY	% Difference	Ratio of $\frac{\sigma_{Meas.}}{\sigma_{ENDF}}$	Difference/σ_{ENDF}
84	33	^{84}As	4.2(5)	1454.55(10)	89.0(82)	0.456%	0.048%	0.302%	0.193%	51.08%	4.02	0.80
86	34	^{86}Se	14.3(3)	2441.1(3)	43.00(454)	0.630%	0.065%	1.019%	0.459%	-38.22%	7.1	0.85
86	34	^{86}Se	14.3(3)	1564.64(14)		0.561%	0.079%	1.019%	0.459%	-44.93%	5.79	1.00
86	35	^{86}Br	55.0(8)	1564.64(14)	65.0(77)	1.168%	0.087%	1.257%	0.289%	-7.06%	3.31	0.31
87	35	^{87}Br	55.65(13)	1419.71(7)	22.0(15)	2.541%	0.218%	1.548%	0.093%	64.16%	0.43	10.69
88	35	^{88}Br	16.29(6)	775.28(6)	67(5)	1.530%	0.151%	1.487%	0.164%	2.91%	1.09	0.26
89	36	^{89}Kr	189.0(24)	220.948(9)	20.10(170)	3.225%	0.480%	2.809%	0.056%	14.79%	0.12	7.40
90	36	^{90}Kr	32.32(9)	1118.69(5)	39.00(312)	2.925%	0.266%	2.746%	0.165%	6.49%	0.62	1.08
92	36	^{92}Kr	1.84(8)	1218.6(1)	59.61(385)	2.119%	0.213%	1.658%	0.046%	27.79%	0.22	9.93
94	37	^{94}Rb	2.702(5)	836.9(1)	61(4)	2.919%	0.294%	2.757%	0.634%	5.91%	2.16	0.26
94	37	^{94}Rb	2.702(5)	1577.5(2)	22.27(183)	3.271%	0.298%	2.757%	0.634%	18.66%	2.13	0.81
94	38	^{94}Sr	75.3(2)	1427.7(1)	94.2(9)	4.339%	0.354%	4.529%	0.498%	-4.19%	1.41	0.38
95	38	^{95}Sr	23.9(14)	685.6(2)	22.60(120)	4.224%	0.392%	4.282%	0.685%	-1.34%	1.75	0.08
96	38	^{96}Sr	1.07(1)	809.40(3)	71.91(256)	3.623%	0.367%	3.871%	0.890%	-6.41%	2.43	0.28
96	39	^{96m}Y	9.6(2)	1750.6(2)	88(??)	0.598%	0.058%	1.521%	0.350%	-60.66%	6.06	2.64
97	39	^{97m}Y	1.17(3)	1103.0(2)	92.35(199)	2.011%	0.170%	1.306%	0.836%	54.07%	4.92	0.84
99	39	^{99}Y	1.47(7)	724.4(2)	17.06(203)	3.837%	0.499%	3.420%	0.787%	12.19%	1.58	0.53
99	39	^{99}Y	1.47(7)	469.137(13)		2.900%	0.263%	3.420%	0.787%	-15.22%	2.99	0.66
99	39	^{99}Y	1.47(7)	546.13(3)		2.508%	0.235%	3.420%	0.787%	-26.67%	3.35	1.16
99	40	^{99}Zr	2.1(1)	469.137(13)	55.20(220)	6.841%	0.608%	5.536%	0.886%	23.56%	1.46	1.47
99	40	^{99}Zr	2.1(1)	546.13(3)	48.29(285)	5.855%	0.495%	5.536%	0.886%	5.76%	1.79	0.36
136	52	^{136}Te	17.5(2)	2077.9(3)	22.37(250)	1.292%	0.152%	1.439%	0.331%	-10.23%	2.17	0.44
136	53	^{136g}I	83.4(10)	1313.02(1)	66.70(0)	1.569%	0.150%	1.594%	0.367%	-1.57%	2.44	0.07
136	53	^{136m}I	46.9(1)	1313.02(1)	100(0)	1.905%	0.155%	3.009%	0.481%	-36.69%	3.1	2.29
138	54	^{138}Xe	844.8(48)	1768.26(13)	16.73(68)	5.067%	0.419%	4.531%	0.091%	11.83%	0.22	5.91
139	54	^{139}Xe	39.68(14)	218.59(3)	56(6)	4.191%	0.598%	3.392%	0.204%	23.55%	0.34	3.93
140	54	^{140}Xe	13.6(1)	1413.66(10)	12.20(171)	2.519%	0.297%	2.737%	0.109%	-7.96%	0.37	1.99
140	55	^{140}Cs	63.7(3)	602.25(5)	53.30(256)	6.210%	0.539%	4.468%	0.715%	38.99%	1.33	2.44
142	55	^{142}Cs	1.684(14)	1326.46(7)	12.92(130)	2.553%	0.285%	2.878%	0.662%	-11.29%	2.33	0.49
143	56	^{143}Ba	14.5(3)	798.79(2)	15.6(18)	6.441%	0.565%	3.719%	0.409%	73.19%	0.72	6.65
144	56	^{144}Ba	11.5(2)	397.440(9)		2.464%	0.242%	3.119%	0.717%	-21.00%	2.96	0.91
144	57	^{144}La	40.8(4)	397.440(9)	94.3(16)	3.644%	0.343%	3.707%	0.222%	-1.71%	0.65	0.29
146	57	^{146m}La	10(1)	258.42(5)	95.25(675)	0.687%	0.147%	0.656%	0.420%	4.71%	2.86	0.07
146	57	^{146}La	6.27(10)	258.47(6)	63.7(30)	1.691%	0.250%	1.558%	0.997%	8.51%	3.99	0.13

Table 5.8: Measured fission yields from ^{235}U and additional data relevant to the respective radioisotopes. The columns of the table are: atomic weight, atomic mass, half-life and uncertainty, gamma-line energy used for the measurement, branching ratio, the ENDF/B-VII.1 estimated fission yield and uncertainty, the measured fission yield and uncertainty, percent difference from ENDF/B-VII.1, ratio of the measured uncertainty divided by the uncertainty quoted from ENDF/B-VII.1, and the number of standard deviations the measured result is from the ENDF/B-VII.1 value using the ENDF/B-VII.1 uncertainty.

A	Z	Iso	$T_{1/2}$ (sec)	E (keV)	I (%)	Meas. FY (%)	$\sigma_{Meas.}$ Meas. FY	ENDF FY (%)	$1\sigma_{ENDF}$ ENDF FY	% Difference	Ratio of $\frac{\sigma_{Meas.}}{\sigma_{ENDF}}$	Difference/σ_{ENDF}
84	33	^{84}As	4.2(5)	1454.55(10)	89.0(82)	0.211%	0.030%	0.265%	0.170%	-20.54%	5.67	0.32
86	34	^{86}Se	14.3(3)	2441.1(3)	43.00(454)	0.397%	0.056%	0.804%	0.362%	-50.65%	6.44	1.13
86	34	^{86}Se	14.3(3)	1564.64(14)		0.335%	0.061%	0.804%	0.362%	-58.37%	5.98	1.30
86	35	^{86}Br	55.0(8)	1564.64(14)	65.0(77)	1.307%	0.144%	1.231%	0.554%	6.23%	3.85	0.14
87	35	^{87}Br	55.65(13)	1419.71(7)	22.0(15)	1.945%	0.232%	1.619%	0.259%	20.11%	1.12	1.26
88	35	^{88}Br	16.29(6)	775.28(6)	67(5)	0.938%	0.116%	1.891%	0.303%	-41.90%	2.6	3.15
89	36	^{89}Kr	189.0(24)	220.948(9)	20.10(170)	4.376%	0.715%	3.513%	0.098%	24.57%	0.14	8.77
90	36	^{90}Kr	32.32(9)	1118.69(5)	39.00(312)	3.533%	0.426%	2.960%	0.681%	19.38%	1.6	0.84
92	36	^{92}Kr	1.84(8)	1218.6(1)	59.61(385)	0.957%	0.124%	0.843%	0.051%	13.59%	0.41	2.26
94	37	^{94}Rb	2.702(5)	836.9(1)	61(4)	0.979%	0.128%	1.398%	0.321%	-29.97%	2.51	1.30
94	37	^{94}Rb	2.702(5)	1577.5(2)	22.27(183)	1.374%	0.177%	1.398%	0.321%	-1.65%	1.81	0.07
94	38	^{94}Sr	75.3(2)	1427.7(1)	94.2(9)	4.103%	0.456%	4.224%	0.972%	-2.86%	2.13	0.12
95	38	^{95}Sr	23.9(14)	685.6(2)	22.60(120)	3.458%	0.435%	3.220%	0.740%	7.42%	1.7	0.32
96	38	^{96}Sr	1.07(1)	809.40(3)	71.91(256)	1.867%	0.244%	1.950%	0.449%	-4.28%	1.84	0.19
96	39	^{96m}Y	9.6(2)	1750.6(2)	88(??)	1.047%	0.131%	2.558%	0.588%	-59.05%	4.5	2.57
97	39	^{97m}Y	1.17(3)	1103.0(2)	92.35(199)	1.820%	0.224%	1.472%	0.942%	23.64%	4.2	0.37
99	39	^{99}Y	1.47(7)	724.4(2)	17.06(203)	1.829%	0.327%	1.415%	0.326%	29.23%	0.99	1.27
99	39	^{99}Y	1.47(7)	469.137(13)		0.331%	0.092%	1.415%	0.326%	-76.64%	3.55	3.33
99	39	^{99}Y	1.47(7)	546.13(3)		0.001%	0.058%	1.415%	0.326%	-99.91%	5.6	4.34
99	40	^{99}Zr	2.1(1)	469.137(13)	55.20(220)	4.349%	0.526%	4.289%	0.986%	1.41%	1.87	0.06
99	40	^{99}Zr	2.1(1)	546.13(3)	48.29(285)	4.360%	0.513%	4.289%	0.986%	1.67%	1.92	0.07
136	52	^{136}Te	17.5(2)	2077.9(3)	22.37(250)	0.400%	0.064%	0.359%	0.230%	11.48%	3.61	0.18
136	53	^{136g}I	83.4(10)	1313.02(1)	66.70(0)	0.051%	0.051%	1.580%	0.363%	-96.78%	7.1	4.21
136	53	^{136m}I	46.9(1)	1313.02(1)	100(0)	1.473%	0.166%	1.226%	0.282%	20.14%	1.7	0.88
138	54	^{138}Xe	844.8(48)	1768.26(13)	16.73(68)	3.302%	0.388%	3.163%	0.089%	4.39%	0.23	1.57
139	54	^{139}Xe	39.68(14)	218.59(3)	56(6)	2.920%	0.488%	2.058%	0.165%	41.91%	0.34	5.24
140	54	^{140}Xe	13.6(1)	1413.66(10)	12.20(171)	0.624%	0.106%	0.934%	0.037%	-33.27%	0.35	8.32
140	55	^{140}Cs	63.7(3)	602.25(5)	53.30(256)	3.412%	0.404%	3.538%	0.814%	-3.58%	2.02	0.16
142	55	^{142}Cs	1.684(14)	359.598(14)	27.20(274)			1.416%	0.326%	NM	NM	NM
143	56	^{143}Ba	14.5(3)	798.79(2)	15.6(18)	2.216%	0.285%	2.705%	0.622%	-18.10%	2.18	0.79
144	56	^{144}Ba	11.5(2)	397.440(9)	94.3(16)	1.183%	0.159%	1.466%	0.337%	-19.31%	2.12	0.84
144	57	^{144}La	40.8(4)	397.440(9)	94.3(16)	2.611%	0.326%	2.952%	0.325%	-11.57%	1	1.05
146	57	^{146m}La	10(1)	258.42(5)	95.25(675)	0.597%	0.105%	0.542%	0.347%	10.22%	3.29	0.16
146	57	^{146}La	6.27(10)	258.47(6)	63.7(30)	0.485%	0.126%	0.722%	0.462%	-32.82%	3.66	0.51

5.4.8 Discussion

New, never before published measurements of the fission yields from 14.3(3) MeV neutron-induced fission for ^{84}As, ^{86}Se, ^{87}Br, ^{94}Rb, ^{94,95,96}Sr; the isomers of ^{96m,97m}Y, ^{99}Y, ^{99}Zr, and ^{136}Te; both the isomer and ground state of ^{136}I, ^{140,142}Cs, ^{143,144}Ba, ^{144}La, and the ground state and isomer of ^{146}La have been presented. More precise measurements of the fission yields of ^{86}Br and ^{90}Kr have also been generated from these data.

After reviewing the results, several conclusions can be inferred: 1) the neutron multiplicities in the lighter mass fission yield distribution for ≈14 MeV neutron-induced fission is likely higher than what was originally used in the England and Rider fission yield evaluation; thus, suppressing the fission yield to isotopes such as ^{84}As, ^{86}Se, ^{94}Rb, and ^{96}Sr, better neutron multiplicity and fission fragment versus fission product yield measurements are needed, 2) fission yields of isomers and linked parent-daughter decay chains where the half-life of the parent is similar to that of the daughter, but not the same, are difficult to analyze but can be measured using the CNAA technique, for more precise measurements, cyclotron based mass separation and penning ion traps [198] should be used, 3) further investigation is needed to cement the yield estimates for the bromine isotopes and noble gas isotopes, better estimates of these nuclides will assist other experimenters in validating their own measurement results; and 4) fission yields for isotopes between 90-100 amu seem to be well understood, likely because of their proximity to a closed nuclear shell.

The measured fission yields for ^{94,95}Sr, ^{136}Te, and ^{144}La agreed with the prediction estimates generated by extrapolating from the measured fission yields using the charge distribution model. The average percent deviation of the measured values from ENDF/B-VII.1 for ^{232}Th, ^{238}U, and ^{235}U were -10.2%, 4.5%, and -12.9%, respectively. Fission yield estimates from ^{232}Th and ^{238}U agreed most closely with ENDF/B-VII.1. Estimates made for the uranium targets that consistently fell within 2σ of the ENDF/B-VII.1 estimated values. The average difference of the measured fission yields compared to ENDF/B-VII.1 using the ENDF/B-VII.1 standard deviation were 0.84, 0.83, and 1.73 for ^{232}Th, ^{238}U, and ^{235}U,

respectively: these values are the average of the right most column of Tab. 5.6—5.8.

High-spin isomers and the variation in their yields, based on the energy of the incident particle, are crucial to improving fission yield models. Fine structural detail of the scission dynamics governs the final spin of the products. Understanding how the additional nuclear energy absorbed from energetic particle interactions and how it propagates to the products yields is important to developing new insights into the fission process.

CHAPTER VI

Conclusions

A total of 69 new fission product yields have been measured for three different actinide targets: thorium-232, uranium-235, and uranium-238. These fission product measurements were performed using delayed gamma-ray spectroscopy and CNAA techniques. Validation of the measured data was accomplished through the comparison of fission yield measurements of bromine-86, -87, and -88, krypton-89, -90, and -92, and xenon-138, -139, and -140 with the Evaluated Nuclear Data Files VII.1. The comparison of krypton fission yield ratios with data acquired by Bocquet [193] showed excellent agreement; the comparison of xenon fission yield ratios was not as good but fission yield estimates of bromine agreed well with ENDF in a majority of cases.

To accomplish this experimental endeavor, the UofM-NSL had to be substantially modified and optimized. Numerous improvements to the facility were made, the most prominent two were the development and characterization of a three-HPGe-crystal coincidence detector and neutron dosimetric characterization of the irradiation geometry.

The objective of this work was to measure new fission yields of arsenic-84, selenium-86, bromine-88, krypton-90 and -92, rubidium-94, strontium-94, -95, and -96, yttrium-96m, zirconium-99, barium-143, and lanthanum-146. Improvements to the fission yield estimates of krypton-90 and -92 relative to the ENDF uncertainties was not achieved; however, the values provided by ENDF are not direct measurements but extrapolations of the charge dis-

tribution model. The measurements obtained of krypton agreed well with the experimental data acquired by Bocquet [193] and suggest the extrapolated estimates from ENDF underestimate the fission yield of krypton-92. New measurements of all other fission products, including an estimate of the isomer ratio of lanthanum-146, were successful. In addition to measuring the fission yields from the original list, bromine-86 and -87, krypton-89, yttrium-96m and -97m, tellurium-136, iodine-136 metastable and ground state, xenon-138, -139, and -140, cesium-140 and -142, barium-143 and -144, and lanthanum-144 were measured.

Based on the measurements conducted for this work, it is clear that immediate air sampling of noble gases following a nuclear detonation can show distinct differences between actinides. Referencing tables 5.6−5.8, yield differences of nearly 50% can be observed between the krypton isotopes of thorium relative to the uranium samples; even xenon, in the high-mass distribution, exhibits order 20% differences in the fission yields of uranium-235 and -238. Fission yields of strontium-94 and -95 show some of the closest agreement between these three actinides and would serve as an excellent benchmark for gamma-line ratio analysis of post-detonation gamma-ray spectra acquired immediately following a detonation. Gamma-lines starting at 1118 keV from krypton-90 and up in energy to 2441 keV from selenium-86 include arsenic-84, bromine-86 and -87, strontium-94, yttrium-96m, iodine-136m/g, and xenon-138 and -139, of which arsenic-84, bromine-87, strontium-94, and xenon-140 have gamma-lines within about 42 keV of one another.

Short-lived fission product analysis for post-detonation nuclear debris analysis is a viable method of nuclear weapon detonation characterization. Fission yield estimates and comparisons obtained from cyclic activation of thorium-232, uranium-238, and uranium-235 clearly prove this assertion.

CHAPTER VII

Future Work

A new cyclic neutron activation analysis and gamma-gamma coincidence detection system is under development at Pacific Northwest National Laboratory. The new system is composed of two 100% relative efficiency germanium detectors that have an adjustable source-to-detector distance. The Thermo-Scientific D711 fusion neutron generator at PNNL is housed within the 318 building inside of the low-scatter room. Because of the size of the room, the walls, floor, and ceiling will be 18 feet from the head of fusion neutron generator decreasing the epithermal and thermal neutron contamination of the nearly pure 14.5 MeV neutron flux by roughly two orders of magnitude. Figure 7.1 is a photo of the new coincidence detection shield and detectors. The support structure is made primarily of aluminum to minimize scatter from the platform.

This new facility will be used to re-examine many of the short-lived fission products measured in this work with higher precision from the same target materials, and later other actinides including plutonium-239 and neptunium-237. The improved detection sensitivity afforded by the radiation shielding being located outside of the neutron generator room, larger lead shield and HPGe detectors, and adjustable source-to-detector distance will provide better signal-to-noise and an order-of-magnitude improvement in the counting statistics. Additional work will be dedicated to improving and expanding the capabilities of Melusine2, a software utility based on ROOT, designed for gamma-gamma coincidence spectroscopy.

Figure 7.1: HPGe coincidence detector located outside of the LSR of the 318 BLDG.

This resource currently lacks a complete list of gamma-gamma coincidence pairs and corresponding gamma-gamma coincidence branching ratios. These gamma-gamma pairs and uncertainties will be generated using an algorithm where individual cascades from each energy level are traced out and collected into a 3-dimensional matrix of decay cascades. Gamma-gamma pair probabilities from each 2-dimensional slice of the matrix are computed before summing the probabilities from common pairs. This method will not only provide a collection of gamma-gamma but beta-gamma, alpha-gamma, and higher order detection sets for automated isotope identification and activity analysis for field deployable sensors currently under development at PNNL.

APPENDIX

APPENDIX A

Fission Product Gamma-spectra Analysis

The fission yield data could not be directly acquired using the ORTEC DSPEC Pro modules because there were limited options to generate the coincident gamma-ray data stream. To identify coincident gamma-rays, using the DSPEC Pro, would've required the use of a pulser to keep the separate, internal clocks synchronized and lengthy post-processing to comb through the two separate data sets to identify coincident gamma-rays with 200 nanosecond resolution. Alternatively, the XIA Pixie-4 module prints the coincident events at their occurrence with a resolution of 13.3 nanoseconds and does not require post-processing. The XIA Pixie-4 module was loaned to the University of Michigan Neutron Science Laboratory to acquire list-mode data from the fission products. Much like the list-mode stream from the DSPEC Pro modules, the list-mode data from the XIA Pixie-4 had to be processed in conjunction with the pneumatic system output to isolate data acquired during the 200 second counting period following each cycle, ignoring all other data. The software resource used to post-process the list-mode from the XIA Pixie-4 into the set of eight CERN ROOT files is provided.

```
void TPixieReader::Read(string filename, CYCLEDATA ptubedata, double* coef) {

    // open bin file from pixie
    ifstream input;
    input.open(filename.c_str());
```

```
// declaration of naming string
string tmp;

// tree title
string treetitle("cycle_data");

// filling variables for each ROOT tree
uint ticks[4]{0}, channel[4]{0};
double energy[4]{0}, clkt[4]{0}, cyct[4]{0}, dtcalc[4]{0};

// recording vector of time responses from channel 0
vector<double> chan0time;

// is channel 0 writing
bool chancheck0(false);

// channel 0 tree
//roottree->Branch("Pneumatic System Data", &fptube_file);
string rootfilename = filename.substr(0,filename.find(".",0));
tmp = rootfilename + "_ch0.root";
TFile *rootfile0 = new TFile(tmp.c_str(), "RECREATE");
TTree *roottree0 = new TTree("CycleDirectory", treetitle.c_str());
roottree0->Branch("ticks", &ticks[0]);
roottree0->Branch("channel", &channel[0]);
roottree0->Branch("energy", &energy[0]);
roottree0->Branch("cyct", &cyct[0]);
roottree0->Branch("clkt", &clkt[0]);
roottree0->Branch("dt", &dtcalc[0]);

// channel 1 tree
tmp = rootfilename + "_ch1.root";
TFile *rootfile1 = new TFile(tmp.c_str(), "RECREATE");
TTree *roottree1 = new TTree("CycleDirectory", treetitle.c_str());
roottree1->Branch("ticks", &ticks[1]);
roottree1->Branch("channel", &channel[1]);
roottree1->Branch("energy", &energy[1]);
roottree1->Branch("cyct", &cyct[1]);
roottree1->Branch("clkt", &clkt[1]);
roottree1->Branch("dt", &dtcalc[1]);

// channel 2 tree
tmp = rootfilename + "_ch2.root";
TFile *rootfile2 = new TFile(tmp.c_str(), "RECREATE");
TTree *roottree2 = new TTree("CycleDirectory", treetitle.c_str());
roottree2->Branch("ticks", &ticks[2]);
roottree2->Branch("channel", &channel[2]);
roottree2->Branch("energy", &energy[2]);
roottree2->Branch("cyct", &cyct[2]);
roottree2->Branch("clkt", &clkt[2]);
roottree2->Branch("dt", &dtcalc[2]);

// channel 3 tree
tmp = rootfilename + "_ch3.root";
TFile *rootfile3 = new TFile(tmp.c_str(), "RECREATE");
TTree *roottree3 = new TTree("CycleDirectory", treetitle.c_str());
roottree3->Branch("ticks", &ticks[3]);
```

```
roottree3->Branch("channel", &channel[3]);
roottree3->Branch("energy", &energy[3]);
roottree3->Branch("cyct", &cyct[3]);
roottree3->Branch("clkt", &clkt[3]);
roottree3->Branch("dt", &dtcalc[3]);

// channel 0 1 tree
tmp = rootfilename + "_ch0_ch1.root";
TFile *rootfile01 = new TFile(tmp.c_str(), "RECREATE");
TTree *roottree01 = new TTree("CycleDirectory", treetitle.c_str());
roottree01->Branch("ticks0", &ticks[0]);
roottree01->Branch("ticks1", &ticks[1]);
roottree01->Branch("channel0", &channel[0]);
roottree01->Branch("channel1", &channel[1]);
roottree01->Branch("energy0", &energy[0]);
roottree01->Branch("energy1", &energy[1]);
roottree01->Branch("cyct0", &cyct[0]);
roottree01->Branch("cyct1", &cyct[1]);
roottree01->Branch("clkt0", &clkt[0]);
roottree01->Branch("clkt1", &clkt[1]);
roottree01->Branch("dt0", &dtcalc[0]);
roottree01->Branch("dt1", &dtcalc[1]);

// channel 0 2 tree
tmp = rootfilename + "_ch0_ch2.root";
TFile *rootfile02 = new TFile(tmp.c_str(), "RECREATE");
TTree *roottree02 = new TTree("CycleDirectory", treetitle.c_str());
roottree02->Branch("ticks0", &ticks[0]);
roottree02->Branch("ticks1", &ticks[2]);
roottree02->Branch("channel0", &channel[0]);
roottree02->Branch("channel1", &channel[2]);
roottree02->Branch("energy0", &energy[0]);
roottree02->Branch("energy1", &energy[2]);
roottree02->Branch("cyct0", &cyct[0]);
roottree02->Branch("cyct1", &cyct[2]);
roottree02->Branch("clkt0", &clkt[0]);
roottree02->Branch("clkt1", &clkt[2]);
roottree02->Branch("dt0", &dtcalc[0]);
roottree02->Branch("dt1", &dtcalc[2]);

// channel 1 2 tree
tmp = rootfilename + "_ch1_ch2.root";
TFile *rootfile12 = new TFile(tmp.c_str(), "RECREATE");
TTree *roottree12 = new TTree("CycleDirectory", treetitle.c_str());
roottree12->Branch("ticks0", &ticks[1]);
roottree12->Branch("ticks1", &ticks[2]);
roottree12->Branch("channel0", &channel[1]);
roottree12->Branch("channel1", &channel[2]);
roottree12->Branch("energy0", &energy[1]);
roottree12->Branch("energy1", &energy[2]);
roottree12->Branch("cyct0", &cyct[1]);
roottree12->Branch("cyct1", &cyct[2]);
roottree12->Branch("clkt0", &clkt[1]);
roottree12->Branch("clkt1", &clkt[2]);
roottree12->Branch("dt0", &dtcalc[1]);
roottree12->Branch("dt1", &dtcalc[2]);
```

```
// channel 0 1 2 tree
tmp = rootfilename + "_ch0_ch1_ch2.root";
TFile *rootfile012 = new TFile(tmp.c_str(), "RECREATE");
TTree *roottree012 = new TTree("CycleDirectory", treetitle.c_str());
roottree012->Branch("ticks0", &ticks[0]);
roottree012->Branch("ticks1", &ticks[1]);
roottree012->Branch("ticks2", &ticks[2]);
roottree012->Branch("channel0", &channel[0]);
roottree012->Branch("channel1", &channel[1]);
roottree012->Branch("channel2", &channel[2]);
roottree012->Branch("energy0", &energy[0]);
roottree012->Branch("energy1", &energy[1]);
roottree012->Branch("energy2", &energy[2]);
roottree012->Branch("cyct0", &cyct[0]);
roottree012->Branch("cyct1", &cyct[1]);
roottree012->Branch("cyct2", &cyct[2]);
roottree012->Branch("clkt0", &clkt[0]);
roottree012->Branch("clkt1", &clkt[1]);
roottree012->Branch("clkt2", &clkt[2]);
roottree012->Branch("dt0", &dtcalc[0]);
roottree012->Branch("dt1", &dtcalc[1]);
roottree012->Branch("dt2", &dtcalc[2]);

// clock ticks for time of capsule arrival
uint timeofcapsule(0);

// iterator storing counts in each type of event
uint iter[17] = {0};

// count-rate monitoring variables
uint counter_east(0), counter_west(0), counter_vert(0);
double countrate_east(0), countrate_west(0), countrate_vert(0);

// capsule return time
double chancheckstime(0);

// channel 3 time, the optical sensor from the ptube system was stashed in this channel
double channel4time(0), prevchannel4time(0);

// cycle number
uint cyclenmbr(0);

// event counter and rollflag counter, respectively
uint ticker(0), bitticker32(0);
bool boolticker(true);

// are we still cycling
bool postcnaa(true);

// count-rate monitor variables
double starttime(0), prevstarttime(0);

// clock timing storage variables
double buf_timehi(0), buf_timetotal(0), prevbuf_timehi(0), evt_timehi(0), evt_time(0), prevevt_time(0)
    ↪ ;
```

```
// unified clock, stores time whenever an event occurs, dead-time channel 0, did we reach the end of
    ↪ buffer rollflag
double uniclock(0), dtzero(0);
bool rollflag(0);

// deadtime and write speed monitoring
ofstream output1, output2, output3;

output1.open("writetime.txt");
output2.open("clkt_deadtime.txt");
output3.open("cyct_deadtime.txt");


while (!input.eof() && postcnaa) {
    // rawdata bin
    unsigned short buf[6];

    // fill rawdata bin
    input.read((char*)&buf[0], 12);

    // how much is left in the current data bin
    short nmbrofwords = buf[0] - 6;

    //         uint modnmbr = buf[1];
    //         uint formatdescriptor = buf[2];
    prevbuf_timehi = buf_timehi;
    buf_timehi = (1000./75.)*double(buf[3]*pow(2.,32));
    buf_timetotal = (1000./75.)*double(buf[3]*pow(2.,32) + buf[4]*pow(2.,16) + buf[5])*1E-9;
    //         if (buf_timehi < prevbuf_timehi) {
    //             buf_timehi += (1000./75.)*double(pow(2.,32));
    //         }
    //
    double writetime(0);

    if (buf_timetotal - uniclock > 50) {
        writetime = buf_timetotal - uniclock - pow(2,32)*1000./75.E9;
    } else if (buf_timetotal - uniclock < -50) {
        writetime = buf_timetotal - uniclock + pow(2,32)*1000./75.E9;
    } else {
        writetime = buf_timetotal - uniclock;
    }

    for (uint i = 0; i < 4; i++) {
        dtcalc[i] += abs(writetime);
        rollflag = true;

        energy[i] = 0;
        channel[i] = 0;
        ticks[i] = 0;
    }
    dtzero += writetime;


    if (chancheck0) {
        rootfile0->cd();
```

```
    roottree0->Fill();

    rootfile1->cd();
    roottree1->Fill();

    rootfile2->cd();
    roottree2->Fill();

    rootfile3->cd();
    roottree3->Fill();
}

if (chancheck0) {
    output1 << writetime << endl;
    if (bitticker32 > 0) {
        output2 << clkt[0] << " " <<  dtzero/clkt[0] << endl;
        output3 << cyct[0] << " " <<  dtzero/clkt[0] << endl;
    }
}

bitticker32++;

if (ticker > 1E6) {
    if (boolticker) {
        cout << "Spills  Total Time   Cycle Time Dead time % Dead time   ch 0      ch 1      ch 2
            ↪      ch 3      ch 0 1    ch 0 2    ch 1 2    ch 0 1 2  " << endl;
        boolticker = false;
    }

    cout.fill(' ');
    cout << left << setw(7) << bitticker32 << " " << left << setw(9) << setprecision(6) << clkt[0]
        ↪  << "    " << left << setw(7) << setprecision(6) << cyct[0] << "    " << left << setw
        ↪ (7) << dtzero << "   " << left << setw(9) << setprecision(6) << dtzero/clkt[0]*100 << "
        ↪      " << left << setw(9) << iter[8] << " " << left << setw(9) << iter[4] << " " <<
        ↪ left << setw(9) << iter[2] << " " << left << setw(9) << iter[1] << " " << left << setw
        ↪ (9) << iter[12] << " " << left << setw(9) << iter[6] << " " << left << setw(9) << iter
        ↪ [10] << " " << left << setw(9) << iter[14] << endl;

    ticker = 0;
}

while (nmbrofwords > 0) {
    // fill rawdata bin
    input.read((char*)&buf[0], 6);

    // increment rawdata bin size counter
    nmbrofwords -= 3;

    // event type flag i.e. 1110 = coincidence event channel 0 1 2
    bitset<4> flag = buf[0];

    // number of channels hit
    uint nmbrofchannels(flag[0] + flag[1] + flag[2] + flag[3]);

    // more precise timing, includes clock ticks from occurrence of event
    evt_timehi = (1000./75.)*double(buf[1]*pow(2., 16)) + buf_timehi;
```

```
prevevt_time = evt_time;

// truest estimate of the event timing
evt_time = evt_timehi + (1000./75.)*double(buf[2]);

// case statement switcher, based on 16 possible outcomes
uint caseval = flag[0]*8 + flag[1]*4 + flag[2]*2 + flag[3];

// counting of event types
iter[caseval]++;
iter[16] += nmbrofchannels;

if (evt_time < chanchecktime) {
    evt_timehi += 1000./75.*pow(2,32);
}

switch (caseval) {
    case 1:
        input.read((char*)buf, 4);
        nmbrofwords -= 2;

        energy[3] = coef[0]*buf[1]*buf[1] + coef[1]*buf[1] + coef[2];
        channel[3] = buf[1];
        ticks[3] = buf[0] - timeofcapsule;
        cyct[3] = (evt_timehi + (1000./75.)*double(buf[0]) - chanchecktime)*1.0E-9 +
            ↪ ptubedata.positiontime[cyclenmbr].transitfrom;
        clkt[3] = (evt_timehi + (1000./75.)*double(buf[0]))*1.0E-9;
        uniclock = clkt[3];
        starttime = evt_timehi + (1000./75.)*double(buf[0]);
        dtcalc[3] = 6.8E-6;

        channel4time = clkt[3];
        cout << "Channel 4 event" << endl;
        cout << "Real-time:\t" << clkt[3] << endl;
        cout << "Channel:\t" << channel[3] << endl;
        cout << "Time Since:\t" << (channel4time - prevchannel4time) << endl;
        boolticker = true;
        prevchannel4time = channel4time;

        rootfile3->cd();
        roottree3->Fill();

        break;
    case 8:
        input.read((char*)buf, 4);
        nmbrofwords -= 2;
        energy[0] = coef[0]*buf[1]*buf[1] + coef[1]*buf[1] + coef[2];
        channel[0] = buf[1];
        ticks[0] = buf[0] - timeofcapsule;
        cyct[0] = (evt_timehi + (1000./75.)*double(buf[0]) - chanchecktime)*1.0E-9 +
            ↪ ptubedata.positiontime[cyclenmbr].transitfrom;
        clkt[0] = (evt_timehi + (1000./75.)*double(buf[0]))*1.0E-9;
        uniclock = clkt[0];
        starttime = evt_timehi + (1000./75.)*double(buf[0]);
        dtzero += 6.8E-6;
        dtcalc[0] = 6.8E-6;
```

```
    ticker++;

    if (chancheck0 && bitticker32 > 100) {
        rootfile0->cd();
        roottree0->Fill();
    }

    counter_east++;
    break;
case 4:
    input.read((char*)buf, 4);
    nmbrofwords -= 2;
    energy[1] = coef[3]*buf[1]*buf[1] + coef[4]*buf[1] + coef[5];
    channel[1] = buf[1];
    ticks[1] = buf[0] - timeofcapsule;
    cyct[1] = (evt_timehi + (1000./75.)*double(buf[0])  - chanchecktime)*1.0E-9 +
        ↪ ptubedata.positiontime[cyclenmbr].transitfrom;
    clkt[1] = (evt_timehi + (1000./75.)*double(buf[0]))*1.0E-9;
    uniclock = clkt[1];
    starttime = evt_timehi + (1000./75.)*double(buf[0]);
    dtcalc[1] = 6.8E-6;



    if (chancheck0 && bitticker32 > 100) {
        rootfile1->cd();
        roottree1->Fill();
    }

    counter_west++;
    break;
case 2:
    input.read((char*)buf, 4);
    nmbrofwords -= 2;
    energy[2] = coef[6]*buf[1]*buf[1] + coef[7]*buf[1] + coef[8];
    channel[2] = buf[1];
    ticks[2] = buf[0] - timeofcapsule;
    cyct[2] = (evt_timehi + (1000./75.)*double(buf[0])  - chanchecktime)*1.0E-9 +
        ↪ ptubedata.positiontime[cyclenmbr].transitfrom;
    clkt[2] = (evt_timehi + (1000./75.)*double(buf[0]))*1.0E-9;
    uniclock = clkt[2];
    starttime = evt_timehi + (1000./75.)*double(buf[0]);
    dtcalc[2] = 6.8E-6;



    if (chancheck0) {
        rootfile2->cd();
        roottree2->Fill();
    }

    counter_vert++;
    break;
case 12:
    input.read((char*)buf, 4);
```

```
        nmbrofwords -= 2;
        energy[0] = coef[0]*buf[1]*buf[1] + coef[1]*buf[1] + coef[2];
        channel[0] = buf[1];
        ticks[0] = buf[0];
        cyct[0] = (evt_timehi + (1000./75.)*double(buf[0])  - chancheckti me)*1.0E-9 +
            ↪ ptubedata.positiontime[cyclenmbr].transitfrom;
        clkt[0] = (evt_timehi + (1000./75.)*double(buf[0]))*1.0E-9;
        starttime = evt_timehi + (1000./75.)*double(buf[0]);
        dtzero += 6.8E-6;
        dtcalc[0] = 6.8E-6;


        input.read((char*)buf, 4);
        nmbrofwords -= 2;
        energy[1] = coef[3]*buf[1]*buf[1] + coef[4]*buf[1] + coef[5];
        channel[1] = buf[1];
        ticks[1] = buf[0];
        cyct[1] = (evt_timehi + (1000./75.)*double(buf[0])  - chancheckti me)*1.0E-9 +
            ↪ ptubedata.positiontime[cyclenmbr].transitfrom;
        clkt[1] = (evt_timehi + (1000./75.)*double(buf[0]))*1.0E-9;
        starttime = evt_timehi + (1000./75.)*double(buf[0]);
        dtcalc[1] = 6.8E-6;



        if (ticks[0] > ticks[1]) {
            dtcalc[1] += abs((ticks[0] - ticks[1])*(1000./75.)*1E-9);
            uniclock = clkt[0];
        } else {
            dtcalc[0] += abs((ticks[1] - ticks[0])*(1000./75.)*1E-9);
            dtzero += abs((ticks[1] - ticks[0])*(1000./75.)*1E-9);
            uniclock = clkt[1];
        }

        if (chancheck0 && bitticker32 > 100) {
            rootfile0->cd();
            roottree0->Fill();

            rootfile1->cd();
            roottree1->Fill();

            rootfile01->cd();
            roottree01->Fill();
        }

        counter_east++;
        counter_west++;
        break;
    case 6:
        input.read((char*)buf, 4);
        nmbrofwords -= 2;
        energy[0] = coef[0]*buf[1]*buf[1] + coef[1]*buf[1] + coef[2];
        channel[0] = buf[1];
        ticks[0] = buf[0] - timeofcapsule;
        cyct[0] = (evt_timehi + (1000./75.)*double(buf[0])  - chancheckti me)*1.0E-9 +
            ↪ ptubedata.positiontime[cyclenmbr].transitfrom;
```

```
    clkt[0] = (evt_timehi + (1000./75.)*double(buf[0]))*1.0E-9;
    starttime = evt_timehi + (1000./75.)*double(buf[0]);
    dtcalc[0] += 6.8E-6;
    dtzero += 6.8E-6;



    input.read((char*)buf, 4);
    nmbrofwords -= 2;
    energy[2] = coef[6]*buf[1]*buf[1] + coef[7]*buf[1] + coef[8];
    channel[2] = buf[1];
    ticks[2] = buf[0] - timeofcapsule;
    cyct[2] = (evt_timehi + (1000./75.)*double(buf[0])  - chanchecktime)*1.0E-9 +
        ↪ ptubedata.positiontime[cyclenmbr].transitfrom;
    clkt[2] = (evt_timehi + (1000./75.)*double(buf[0]))*1.0E-9;
    starttime = evt_timehi + (1000./75.)*double(buf[0]);
    dtcalc[2] = 6.8E-6;

    if (ticks[0] > ticks[2]) {
        dtcalc[2] += abs((ticks[0] - ticks[2])*(1000./75.)*1E-9);
        uniclock = clkt[0];
    } else {
        dtcalc[0] += abs((ticks[2] - ticks[0])*(1000./75.)*1E-9);
        dtzero += abs((ticks[2] - ticks[0])*(1000./75.)*1E-9);
        uniclock = clkt[2];
    }

    if (chancheck0 && bitticker32 > 100) {
        rootfile0->cd();
        roottree0->Fill();

        rootfile2->cd();
        roottree2->Fill();

        rootfile02->cd();
        roottree02->Fill();
    }

    counter_east++;
    counter_vert++;
    break;
case 10:
    input.read((char*)buf, 4);
    nmbrofwords -= 2;
    energy[1] = coef[3]*buf[1]*buf[1] + coef[4]*buf[1] + coef[5];
    channel[1] = buf[1];
    ticks[1] = buf[0] - timeofcapsule;
    cyct[1] = (evt_timehi + (1000./75.)*double(buf[0])  - chanchecktime)*1.0E-9 +
        ↪ ptubedata.positiontime[cyclenmbr].transitfrom;
    clkt[1] = (evt_timehi + (1000./75.)*double(buf[0]))*1.0E-9;
    starttime = evt_timehi + (1000./75.)*double(buf[0]);
    dtcalc[1] = 6.8E-6;



    input.read((char*)buf, 4);
```

```
        nmbrofwords -= 2;
        energy[2] = coef[6]*buf[1]*buf[1] + coef[7]*buf[1] + coef[8];
        channel[2] = buf[1];
        ticks[2] = buf[0] - timeofcapsule;
        cyct[2] = (evt_timehi + (1000./75.)*double(buf[0])  - chancheckti
            ↪ me)*1.0E-9 + ptubedata.positiontime[cyclenmbr].transitfrom;
        starttime = evt_timehi + (1000./75.)*double(buf[0]);
        dtcalc[2] = 6.8E-6;

        if (ticks[1] > ticks[2]) {
            dtcalc[2] += abs((ticks[1] - ticks[2])*(1000./75.)*1E-9);
            uniclock = clkt[1];
        } else {
            dtcalc[1] += abs((ticks[2] - ticks[1])*(1000./75.)*1E-9);
            uniclock = clkt[2];
        }

        if (chancheck0 && bitticker32 > 100) {
            rootfile1->cd();
            roottree1->Fill();

            rootfile2->cd();
            roottree2->Fill();

            rootfile12->cd();
            roottree12->Fill();
        }

        counter_west++;
        counter_vert++;
        break;
    case 14:
        input.read((char*)buf, 4);
        nmbrofwords -= 2;
        energy[0] = coef[0]*buf[1]*buf[1] + coef[1]*buf[1] + coef[2];
        channel[0] = buf[1];
        ticks[0] = buf[0] - timeofcapsule;
        cyct[0] = (evt_timehi + (1000./75.)*double(buf[0])  - chancheckti
            ↪ me)*1.0E-9 + ptubedata.positiontime[cyclenmbr].transitfrom;
        clkt[0] = (evt_timehi + (1000./75.)*double(buf[0]))*1.0E-9;
        starttime = evt_timehi + (1000./75.)*double(buf[0]);
        dtcalc[0] = 6.8E-6;
        dtzero += 6.8E-6;


        input.read((char*)buf, 4);
        nmbrofwords -= 2;
        energy[1] = coef[3]*buf[1]*buf[1] + coef[4]*buf[1] + coef[5];
        channel[1] = buf[1];
        ticks[1] = buf[0] - timeofcapsule;
        cyct[1] = (evt_timehi + (1000./75.)*double(buf[0])  - chancheckti
            ↪ me)*1.0E-9 + ptubedata.positiontime[cyclenmbr].transitfrom;
        clkt[1] = (evt_timehi + (1000./75.)*double(buf[0]))*1.0E-9;
        starttime = evt_timehi + (1000./75.)*double(buf[0]);
        dtcalc[1] += 6.8E-6;
```

```
input.read((char*)buf, 4);
nmbrofwords -= 2;
energy[2] = coef[6]*buf[1]*buf[1] + coef[7]*buf[1] + coef[8];
channel[2] = buf[1];
ticks[2] = buf[0] - timeofcapsule;
cyct[2] = (evt_timehi + (1000./75.)*double(buf[0])  - chanchecktime)*1.0E-9 +
    ↪ ptubedata.positiontime[cyclenmbr].transitfrom;
clkt[2] = (evt_timehi + (1000./75.)*double(buf[0]))*1.0E-9;
starttime = evt_timehi + (1000./75.)*double(buf[0]);
dtcalc[2] = 6.8E-6;

int bigchannel;

if (ticks[0] >= ticks[1] && ticks[0] >= ticks[2]) {
    bigchannel = 0;
} else if (ticks[1] >= ticks[0] && ticks[1] >= ticks[2]) {
    bigchannel = 1;
} else if (ticks[2] >= ticks[0] && ticks[2] >= ticks[1]) {
    bigchannel = 2;
}

switch (bigchannel) {
    case 0:
        dtcalc[1] += abs((ticks[0] - ticks[1])*(1000./75.)*1E-9);
        dtcalc[2] += abs((ticks[0] - ticks[2])*(1000./75.)*1E-9);
        uniclock = clkt[0];
        break;
    case 1:
        dtcalc[0] += abs((ticks[1] - ticks[0])*(1000./75.)*1E-9);
        dtzero += abs((ticks[1] - ticks[0])*(1000./75.)*1E-9);
        dtcalc[2] += abs((ticks[1] - ticks[2])*(1000./75.)*1E-9);
        uniclock = clkt[1];
        break;
    case 2:
        dtcalc[0] += abs((ticks[2] - ticks[0])*(1000./75.)*1E-9);
        dtzero += abs((ticks[2] - ticks[0])*(1000./75.)*1E-9);
        dtcalc[1] += abs((ticks[2] - ticks[1])*(1000./75.)*1E-9);
        uniclock = clkt[2];
        break;
    default:
        break;
}


if (chancheck0 && bitticker32 > 100) {
    rootfile0->cd();
    roottree0->Fill();

    rootfile1->cd();
    roottree1->Fill();

    rootfile2->cd();
    roottree2->Fill();

    rootfile012->cd();
    roottree012->Fill();
```

```
        }

        counter_east++;
        counter_west++;
        counter_vert++;
        break;
    default:
        break;
}

if (starttime - prevstarttime > 1E6) {
    double delta = (starttime - prevstarttime);
    prevstarttime = starttime;
    countrate_east = counter_east/delta*1.E9;
    countrate_west = counter_west/delta*1.E9;
    countrate_vert = counter_vert/delta*1.E9;

    if (countrate_east > coef[9] && countrate_west > coef[9] && countrate_vert > coef[9] && !
        ↪ chancheck0) {
        cout << "COUNT_RATES_//////////////////////////////////////////" << endl;
        cout << countrate_east << "\t" << countrate_west << "\t" << countrate_vert << "\t" <<
            ↪ clkt[0] << endl;
        chancheck0 = true;
        chanchecktime = starttime;
        for (int q = 0; q < 4; q++) {
            dtcalc[q] = 0;
        }
    }

    if (countrate_east > coef[9]*2 && countrate_west > coef[9]*2 && countrate_vert > coef
        ↪ [9]*2) {
        cout << "PROBLEM_
            ↪ !!!!!!!!!!!!!!!!!!!!!!!!!!!!!!!!!!!!!!!!!!!!!!!!!!!!!!!!!!!!!!!!!!!!!!!!!!!!!!!!!!!!!!!!!!!!!!!!!!!!
            ↪ " << endl;
        cout << countrate_east << "\t" << countrate_west << "\t" << countrate_vert << "\t" <<
            ↪ clkt[0] << endl;
    }

    if ((starttime - chanchecktime)*1.E-9 > ptubedata.headerfile.counttime+4. && chancheck0) {
        chancheck0 = false;
        cyclenmbr++;
        memset(&dtcalc, 0, sizeof(dtcalc));

        if (cyclenmbr >= ptubedata.headerfile.cycles) {
            postcnaa = false;
        }

        cout << "_Cycle_Switch\t" << cyclenmbr << endl;
        cout << "Time_DIFF_\t" << (starttime - chanchecktime)*1.E-9 << "\t" << cyclenmbr <<
            ↪ endl;
    }

    counter_east = 0;
    counter_west = 0;
    counter_vert = 0;
```

```
            }
        }
    }

    rootfile0->cd();
    roottree0->Write();
    rootfile0->Close();

    rootfile1->cd();
    roottree1->Write();
    rootfile1->Close();

    rootfile2->cd();
    roottree2->Write();
    rootfile2->Close();

    rootfile3->cd();
    roottree3->Write();
    rootfile3->Close();

    rootfile01->cd();
    roottree01->Write();
    rootfile01->Close();

    rootfile02->cd();
    roottree02->Write();
    rootfile02->Close();

    rootfile12->cd();
    roottree12->Write();
    rootfile12->Close();

    rootfile012->cd();
    roottree012->Write();
    rootfile012->Close();


    cout << "_Total_Number_of_Observed_Cycles_\t" << cyclenmbr << endl;
    cout << "_Total_Number_of_Spills_\t" << bitticker32 << endl;
    cout << "Spills\t\tTotal_Time" << endl;
    cout << bitticker32 << "\t\t" << clkt[0] << endl;

}
```

Following the list-mode processing to generate the *root* trees, the trees were examined and parsed into spectra using a set of user defined inputs. The *root* script used to isolate photo-peaks within the spectra and analyze their peak area is provided.

```
void peekit(string* file_prefix, UInt_t nmbr_prefix, int nmbrcycles, Double_t start_time, Double_t
    ↪ end_time, Double_t energy, Double_t e_delta, Double_t time_res, UInt_t E_res, uint nmbrofgaus = 0,
    ↪ double percentvariationresolution = 40, double ecal1 = 0.1098, double ecal2 = 3.) {

    string fittername = "Minuit2";
```

```
TVirtualFitter::SetDefaultFitter(fittername.c_str());
gStyle->SetOptStat(1111111);
gStyle->SetOptFit(1111111);

clock_t ticks1, ticks2;

ticks1 = clock();

double start_energy(0), end_energy(0);

start_energy = energy - e_delta;
end_energy = energy + e_delta;


bool fullfit = false;

if(nmbrofgaus > 0) {
    fullfit = true;
}

TChain* singleschain = new TChain("CycleDirectory","singles_data");
TChain* coincchain = new TChain("CycleDirectory","coincident_data");

TString tmp;
for (UInt_t i=0; i < nmbr_prefix; i++) {
    tmp = file_prefix[i] +"_ch0_ch1.root";
    coincchain->Add(tmp);
    tmp = file_prefix[i] +"_ch0_ch2.root";
    coincchain->Add(tmp);
    tmp = file_prefix[i] +"_ch1_ch2.root";
    coincchain->Add(tmp);
}
////////////////////////////////////////////////
for (UInt_t i=0; i < nmbr_prefix; i++) {
    tmp = file_prefix[i] +"_ch0.root";
    singleschain->Add(tmp);
    tmp = file_prefix[i] +"_ch1.root";
    singleschain->Add(tmp);
    tmp = file_prefix[i] +"_ch2.root";
    singleschain->Add(tmp);
}
////////////////////////////////////////////////

UInt_t start_channel, end_channel;
start_channel = (start_energy - ecal2)/ecal1;
end_channel = (end_energy - ecal2)/ecal1;

int addedbins(0);
bool unsquarebins(true);

if(E_res > 1 && ((end_channel - start_channel) % E_res)) {
    while(unsquarebins) {
        addedbins++;
        int tmp = end_channel - start_channel + addedbins;
        if (!(tmp % E_res)) {
            unsquarebins = false;
```

```
        }
    }

    unsquarebins = ((end_channel - start_channel + addedbins) % E_res);

    if (unsquarebins) {
        cout << "ERROR " << end_channel << "\t" << start_channel << "\t" << addedbins << "\t" << E_res
            ↪ << endl;
        return;
    }

    start_channel -= floor(double(addedbins)/2.0);
    end_channel += ceil(double(addedbins)/2.0);

}

int binning = (end_channel - start_channel + 1)/(E_res);

Double_t tmp_s_e(0), tmp_e_e(0);

start_energy = ecal1*start_channel + ecal2;
end_energy = ecal1*end_channel + ecal2;

double energy_delta(end_energy-start_energy);

Double_t resolution = (0.135*sqrt(start_channel+binning*E_res/2) + 5.6)/2.;

cout << "Channels & Energy " << start_channel << "\t" << end_channel << "\t" << (end_channel-
    ↪ start_channel) << "\t" << start_energy << "\t" << end_energy << "\t" << (end_energy-
    ↪ start_energy) << endl;
// setup a canvas for visual review of data
//////////////////////////////////////////
TCanvas* c1 = new TCanvas("Peek_Region", file_prefix[0].c_str(), 1200, 800);
c1->Draw();
c1->Divide(3,2);
c1->cd(1);

Double_t minE(25), maxE(7150);
UInt_t bins((maxE - minE - ecal2)/ecal1*1/(5*E_res));

UInt_t min_chan((minE - ecal2)/ecal1*1/(5*E_res));
UInt_t low_chan((start_energy - ecal2)/ecal1*1/(5*E_res));
UInt_t high_chan((end_energy - ecal2)/ecal1*1/(5*E_res));

// plot the coincidence regions of interest to identify possible coincident lines
////////////////////////////////////////////////////////////////////////////////
/// Plot the lower and higher coincidence plane for the user-defined region of
/// interest after folding the the data along the diagonal for statistics.
stringstream drawstring1, drawstring2;
drawstring1.str("");
drawstring1 << "energy0:energy1>>hcoinc(" << bins << "," << minE << "," << maxE << "," << bins << "
    ↪ ," << minE << "," << maxE << ")";
drawstring2.str("");
drawstring2 << "cyct0>" << start_time << "&&cyct0<" << end_time;
coincchain->Draw(drawstring1.str().c_str(),drawstring2.str().c_str(),"CONT4Z");
TH2D* hcoinc = (TH2D*)c1->GetPad(1)->GetPrimitive("hcoinc");
```

```
hcoinc->SetBinContent(1, 1, -10.);

for(UInt_t i=2; i < bins; i++) {
    for(UInt_t j = 1; j < bins; j++) {
        Double_t tmp1 = hcoinc->GetBinContent(i,j);
        Double_t tmp2 = hcoinc->GetBinContent(j,i);
        hcoinc->SetBinContent(j, i, (tmp1 + tmp2));
        hcoinc->SetBinContent(i, j, (tmp1 + tmp2));
    }
}

c1->cd(4);
TH1D* hproj = hcoinc->ProjectionY("proj_y", low_chan - min_chan, high_chan - min_chan);
hproj->SetStats(0);
hproj->SetTitle("Coincidence Projection");
hproj->GetXaxis()->SetTitle("Energy (keV)");
hproj->GetXaxis()->CenterTitle();
hproj->GetYaxis()->SetTitle("Counts");
hproj->GetYaxis()->CenterTitle();
hproj->GetYaxis()->SetTitleOffset(1.5);
hproj->Draw();

c1->cd(1);
hcoinc->SetStats(0);
hcoinc->SetTitle("Coincidence Scatter");
hcoinc->GetXaxis()->SetTitle("Energy (keV)");
hcoinc->GetXaxis()->CenterTitle();
hcoinc->GetXaxis()->SetRangeUser(minE, maxE);
hcoinc->GetYaxis()->SetTitle("Energy (keV)");
hcoinc->GetYaxis()->CenterTitle();
hcoinc->GetYaxis()->SetTitleOffset(1.5);
hcoinc->GetYaxis()->SetRangeUser(start_energy, end_energy);
hcoinc->Draw("CONT4Z");
c1->Update();

// initialize access variable to the tree within the singleschain
//////////////////////////////////////////////////////////////////
Double_t real_time, dead_time, channelread;

singleschain->SetBranchAddress("channel", &channelread);
singleschain->SetBranchAddress("dt", &dead_time);
singleschain->SetBranchAddress("cyct", &real_time);

// search singleschain for starting and ending realtimes and deadtimes
//////////////////////////////////////////////////////////////////////
/// \brief cycle_dts
/// Step through the singlesTree values searching for the realtimes that
/// correspond to the user-defined start_time and end_time of the count.
/// Collect those values to average and estimate the realtime and deadtime
/// of the count.
vector <Double_t> rt_vals, lt_vals, dt_vals;
vector <int> occurence, sumofevents;

int dt_meas = floor((end_time - start_time)/time_res);
```

```
rt_vals.resize(dt_meas);
lt_vals.resize(dt_meas);
dt_vals.resize(dt_meas);
occurence.resize(dt_meas);
sumofevents.resize(dt_meas);
for (int i = 0; i < dt_meas; i++) {
    dt_vals[i] = 0;
    occurence[i] = 0;
}

for (UInt_t i = 0; i < singleschain->GetEntries(); i++) {
    singleschain->GetEntry(i);
    for (UInt_t j = 0; j < dt_meas; j++) {
        if(real_time > start_time + j*time_res && real_time < start_time + (j + 1)*time_res) {
            rt_vals[j] = time_res;
            dt_vals[j] += dead_time;
            occurence[j]++;
            sumofevents[j]++;
        }
    }
}

for (UInt_t i = 0; i < dt_meas - 1; i++) {
    dt_vals[i] = dt_vals[i]/(3*nmbrcycles);
    lt_vals[i] = rt_vals[i] - dt_vals[i];
}
rt_vals[dt_meas - 1] = rt_vals[dt_meas - 2];
dt_vals[dt_meas - 1] = dt_vals[dt_meas - 2];
lt_vals[dt_meas - 1] = rt_vals[dt_meas - 2] - dt_vals[dt_meas - 2];

for (UInt_t i = 0; i < dt_meas; i++) {
    cout << rt_vals[i] << "\t" << lt_vals[i] << "\t" << dt_vals[i] << "\t" << sumofevents[i] << endl;
}

// plot the time-dependent singles data
//////////////////////////////////////
c1->cd(2);
drawstring1.str("");

drawstring1 << "cyct:energy>>hsingle_t(" << binning << "," << start_energy << "," << end_energy << ","
    ↪ << dt_meas << "," << start_time << "," << end_time << ")";
singleschain->Draw(drawstring1.str().c_str(),"","COL4Z");
TH2D* hsingle_t = (TH2D*)c1->GetPad(2)->GetPrimitive("hsingle_t");

hsingle_t->SetStats(0);
hsingle_t->SetTitle("Temporal Peak");
hsingle_t->GetXaxis()->SetTitle("Energy (keV)");
hsingle_t->GetXaxis()->CenterTitle();
hsingle_t->GetYaxis()->SetTitle("Time (sec)");
hsingle_t->GetYaxis()->CenterTitle();
hsingle_t->GetYaxis()->SetTitleOffset(1.5);
hsingle_t->Draw("COL4Z");

Double_t* params = new Double_t[7];

if (!fullfit) {
```

```
    c1->cd(3);
    c1->SetLogz();
    Double_t* params = new Double_t[7];
    TH2D* hsingle_tsurf = (TH2D*)hsingle_t->Clone();
    hsingle_tsurf->SetStats(0);
    hsingle_tsurf->SetTitle("Temporal Peak");
    hsingle_tsurf->GetXaxis()->SetTitle("Energy (keV)");
    hsingle_tsurf->GetXaxis()->CenterTitle();
    hsingle_tsurf->GetYaxis()->SetTitle("Time (sec)");
    hsingle_tsurf->GetYaxis()->CenterTitle();
    hsingle_tsurf->GetYaxis()->SetTitleOffset(1.5);
    hsingle_tsurf->Draw("CONT4Z");
}

if(false/*fullfit*/) {
    TF2* fitfn = new TF2("expwbigaus",expwbigaus, start_energy, end_energy, start_time, end_time, 8);

    // centroid
    params[0]  = start_energy+(start_energy-end_energy)/2.0;
    // bigaussian params
    params[1]  = 2;
    params[2]  = 0.5*hsingle_t->GetMaximum();
    params[3]  = 2;
    // bkg (linear) params
    params[4] = 0;
    params[5] = 0.1*hsingle_t->GetMaximum();
    // half-life
    params[6] = 5;
    params[7] = 5;

    //set fit function paramters
    fitfn->SetParameters(params);

    //centroid
    fitfn->SetParLimits(0,  start_energy, end_energy);
    //bigaussian
    //        fitfn->SetParLimits(1,  0.75*resolution, 1.25*resolution);
    fitfn->SetParLimits(2,  0.1, 2*hsingle_t->GetMaximum());
    //        fitfn->SetParLimits(3,  0.75*resolution, 1.25*resolution);
    //bkg
    fitfn->SetParLimits(4, -0.5*hsingle_t->GetMaximum() , 0.5*hsingle_t->GetMaximum());
    fitfn->SetParLimits(5,  0, hsingle_t->GetMaximum());
    // half-life
    fitfn->SetParLimits(6,  0.1, end_time);
    fitfn->SetParLimits(7,  0.1, end_time);

    // declare TFitResultPtr for access to fitting result and print the result
    TFitResult* fitresult;
    fitresult = hsingle_t->Fit("expwbigaus", "SERBMQ").Get();
    fitresult->Print("v");

    cout << "////////////////////////// GOODNESS OF FIT //////////////////////////" << endl;
    cout << "Chi-square:\t\t" << fitresult->Chi2() << endl;
    cout << "Norm. Chi-square:\t" << fitresult->Chi2()/fitfn->GetNDF() << endl;

    // declare residual histogram
```

```
    TH2D *hres = (TH2D*)hsingle_t->Clone();
    hres->SetTitle("Temporal Residuals");
    hres->GetXaxis()->SetTitle("Energy (keV)");
    hres->GetXaxis()->CenterTitle();
    hres->GetYaxis()->SetTitle("Time (sec)");
    hres->GetYaxis()->CenterTitle();
    hres->GetYaxis()->SetTitleOffset(1.5);

    // fill residual histogram
    Double_t res(0), reserr(0);
    for (UInt_t i = 1; i < hsingle_t->GetNbinsX() + 1; i++) {
        for (UInt_t j = 1; j < hsingle_t->GetNbinsY() + 1; j++) {
            Double_t res =  fitfn->Eval(i,j) - hsingle_t->GetBinContent(i,j);
            Double_t reserr = hsingle_t->GetBinError(i,j);
            hres->SetBinContent(i, j, res/reserr);
            hres->SetBinError(i, j, 1);
        }
    }

    c1->cd(3);
    hres->Draw("COL4Z");

    // draw residual histogram
    c1->cd(5);
    hres->SetStats(0);
    hres->Draw();
}

// plot 1-D histogram
//////////////////////
c1->cd(5);
drawstring1.str("");
drawstring2.str("");
drawstring1 << "energy>>hsingletotal(" << binning << "," << start_energy << "," << end_energy << ")";
drawstring2 << "cyct_" << start_time << "&&_cyct_<" << end_time;
singleschain->Draw(drawstring1.str().c_str(),drawstring2.str().c_str());
TH1D* hsingletotal = (TH1D*)c1->GetPad(5)->GetPrimitive("hsingletotal");

hsingletotal->SetStats(0);
hsingletotal->SetTitle("Peak Area");
hsingletotal->GetXaxis()->SetTitle("Energy (keV)");
hsingletotal->GetXaxis()->CenterTitle();
hsingletotal->GetYaxis()->SetTitle("Counts");
hsingletotal->GetYaxis()->CenterTitle();
hsingletotal->GetYaxis()->SetTitleOffset(1.5);
hsingletotal->Draw();
c1->Update();


// extract peak areas from region in singleschain
//////////////////////////////////////////////////////////////////////
vector <Double_t> pkareaMAESTRO, pksigMAESTRO;
vector <Double_t> pkchi;
vector < vector <Double_t> > pkareafit, pksigfit, centroidfit, fwhmfit;

pkareaMAESTRO.resize(dt_meas);
```

```
pksigMAESTRO.resize(dt_meas);
pkchi.resize(dt_meas);

pkareafit.resize(dt_meas);
pksigfit.resize(dt_meas);
centroidfit.resize(dt_meas);
fwhmfit.resize(dt_meas);
for (uint j = 0; j < dt_meas; j++) {
    pkareafit[j].resize(nmbrofgaus);
    pksigfit[j].resize(nmbrofgaus);
    centroidfit[j].resize(nmbrofgaus);
    fwhmfit[j].resize(nmbrofgaus);
}


if (fullfit) {
    drawstring1.str("");
    drawstring1 << "channel>>hsingle(" << binning << "," << start_channel << "," << end_channel << ")"
        ↪ ;

    c1->cd(6);

    for (UInt_t i = 0; i < dt_meas; i++) {
        drawstring2.str("");
        drawstring2 << "cyct>" << start_time + i*time_res << "&&cyct<" << start_time + (i+1)*
            ↪ time_res;

        singleschain->Draw(drawstring1.str().c_str(), drawstring2.str().c_str());
        c1->Update();
        c1->Draw();
        TH1D* h = (TH1D*)c1->GetPad(6)->GetPrimitive("hsingle");

        // declare a fitting function for multipeak fitting
        TF1* sfitfn = new TF1("sfit", simplemodularfitfunction, start_channel, end_channel, 3*
            ↪ nmbrofgaus+3);
        params = new Double_t[4*nmbrofgaus+2]{0};
        params[0] = nmbrofgaus;
        //centroid
        Double_t val = h->GetMean();
        sfitfn->FixParameter(0, nmbrofgaus);

        //define background parameters
        double lbkg_slope(0), rbkg_slope(0);

        for( uint j=3; j < 8; j++) {
            lbkg_slope += h->GetBinContent(j);
            rbkg_slope += h->GetBinContent(h->GetNbinsX() - j);
        }

        double bkg_slope = (rbkg_slope/5 - lbkg_slope/5)/(end_channel - start_channel);
        double bkg_const = rbkg_slope/5 - bkg_slope*start_channel;
        double peakheight = h->GetMaximum() - (lbkg_slope + rbkg_slope)/10.;
        double peakcentroid = (end_channel - start_channel)/2 + start_channel;
        cout << "BKG_m_" << bkg_slope << "_BKG_b_" << bkg_const << "_lbkg_" << lbkg_slope << "_rbkg_"
            ↪ << rbkg_slope << "_start_ch_" << start_channel << "_end_ch" << end_channel <<  endl;
```

```
// bkg (linear) params
params[3*nmbrofgaus+1] = bkg_slope;
params[3*nmbrofgaus+2] = bkg_const;

if (nmbrofgaus == 1) {
    params[1]  = peakcentroid;
    // gaussian params
    params[2]  = resolution;
    params[3]  = peakheight;
    cout << "Peak Guess " << " centroid: " << params[1] << " resolution: " << params[2] << "
        ↪ height: " << params[3] << endl;
} else if( nmbrofgaus > 1) {
    for (uint j = 0; j < nmbrofgaus; j++) {
        // centroid
        params[1+j*3]  = (end_channel - start_channel)/(2*nmbrofgaus) + (end_channel-
            ↪ start_channel)/(nmbrofgaus)*j + start_channel;
        // gaussian params
        params[2+j*3]  = resolution + resolution*(0.1*j/nmbrofgaus);
        params[3+j*3]  = peakheight - peakheight*(0.1*j/nmbrofgaus);
        cout << "Peak Guess #" << j << " centroid: " << params[1+j*3] << " resolution: " <<
            ↪ params[2+j*3] << " height: " << params[3+j*3] << endl;
    }
}

if (nmbrofgaus == 1) {
    sfitfn->SetParLimits(1,  peakcentroid - 3*resolution, peakcentroid + 3*resolution);
    sfitfn->SetParLimits(2,  (1.-percentvariationresolution/100.)*resolution, (1.+
        ↪ percentvariationresolution/100.)*resolution);
    sfitfn->SetParLimits(3,  peakheight*0.5, peakheight*1.5);
} else if( nmbrofgaus > 1) {

    for (uint j = 0; j < nmbrofgaus; j++) {
        sfitfn->SetParLimits(1+j*3,  start_channel, end_channel);
        sfitfn->SetParLimits(2+j*3,  (1.-percentvariationresolution/100.)*resolution, (1.+
            ↪ percentvariationresolution/100.)*resolution);
        sfitfn->SetParLimits(3+j*3,  0, 2*peakheight);
    }

}

//set fit function paramters
sfitfn->SetParameters(params);

// declare TFitResultPtr for access to fitting result and print the result
TFitResult* sfitresult;
sfitresult = h->Fit("sfit", "SERBMQ").Get();
sfitresult->Print("v");
c1->Update();
c1->Draw();

params = sfitfn->GetParameters();



TF1* gaus = new TF1("gaus", gaussian, minE , maxE, 4);
Double_t* gausparams = new Double_t[4]{0};
```

```
gausparams[0] = params[1];
gausparams[1] = params[2];
gausparams[2] = params[3];
gaus->SetParameters(gausparams);

TF1* bkgfn = new TF1("bkg", bkgfunction, minE , maxE, 3);
Double_t* bkgparams = new Double_t[3]{0};
bkgparams[0] = params[1];
bkgparams[1] = params[3*nmbrofgaus+1];
bkgparams[2] = params[3*nmbrofgaus+2];
bkgfn->SetParameters(bkgparams);

h->SetStats(0);
h->SetFillColor(kGreen);
h->SetFillStyle(3003);
h->SetTitle("Peak Area");
h->GetXaxis()->SetTitle("Channel");
h->GetXaxis()->CenterTitle();
h->GetYaxis()->SetTitle("Counts");
h->GetYaxis()->CenterTitle();
h->GetYaxis()->SetTitleOffset(1.5);
h->Draw();
TLegend *lgnd = new TLegend(0.1, 0.7, 0.35, 0.9);
lgnd->AddEntry(h,"Data");

sfitfn->SetLineColor(kRed);
lgnd->AddEntry(sfitfn,"Fit");
sfitfn->Draw("same");

gaus->SetLineColor(kOrange-2);
lgnd->AddEntry(gaus,"Gaussian #1");
gaus->Draw("same");

bkgfn->SetLineColor(kBlue);
lgnd->AddEntry(bkgfn,"Background");
bkgfn->Draw("same");
lgnd->Draw("same");
c1->Update();
c1->Draw();

// print peak area for each peak
TMatrixTSym<Double_t> cov_matrix = sfitresult->GetCovarianceMatrix();
Double_t lbkg(0), rbkg(0), total(0), pkarea(0), pkareasig(0);
cout << "////////////////////// MAESTRO SUM & DIFFERENCE //////////////////////" << endl;
for (UInt_t j = 1; j < 4; j++) {
    lbkg += h->GetBinContent(j);
}

for (UInt_t j = h->GetNbinsX() - 3; j < h->GetNbinsX(); j++) {
    rbkg += h->GetBinContent(j);
}

for (UInt_t j = 1; j < h->GetNbinsX(); j++) {
    total += h->GetBinContent(j);
}
```

```
pkarea = (total - rbkg - lbkg) - (rbkg + lbkg)/6.*(h->GetNbinsX() - 5);

pkareaMAESTRO[i] = pkarea;

pkareasig = sqrt((total - rbkg - lbkg) + (rbkg + lbkg)/6.*(h->GetNbinsX() - 5));

pksigMAESTRO[i] = pkareasig;

cout << "Total Area:\t\t\t" << total << "\tl/r/bins\t" << lbkg << "\t" << rbkg << "\t" << h->
    ↪ GetNbinsX()+1 << "\t" << endl;

cout << "Peak Area:\t\t\t" << pkarea << "\t+/-\t" << pkareasig << endl;

cout << "////////////////////////// PEAK FIT & INTEGRAL //////////////////////////" << endl;
cout << "Peak Centroid: " << params[1] << "\t\t" << "Total Area:\t\t\t" << sfitfn->Integral(
    ↪ start_channel, end_channel) << "\t+/-\t" << sfitfn->IntegralError(start_channel,
    ↪ end_channel, &params[0], sfitresult->GetCovarianceMatrix().GetMatrixArray())/E_res <<
    ↪ endl;

cout << "////////////////////////// GOODNESS OF FIT //////////////////////////" << endl;
cout << "Chi-square:\t\t\t" << sfitresult->Chi2() << endl;
Double_t chi(0);
chi = sfitresult->Chi2()/sfitfn->GetNDF();
pkchi[i] = chi;
cout << "Norm. Chi-square:\t\t" << chi << endl;


// print peak area for each peak
////////////////////////////////
Double_t* singleparamset;

for (uint j = 0; j < nmbrofgaus; j++) {
    cout << "////////////////////////// INTEGRAL: PEAK #" << j+1 << "
        ↪ //////////////////////////" << endl;
    singleparamset = new Double_t[3]{0};
    TF1* sfitfnsinglepeak = new TF1("sfit", gaussian, start_channel*0.9, end_channel*1.1, 3);

    singleparamset[0] = params[1+3*j];
    singleparamset[1] = params[2+3*j];
    singleparamset[2] = params[3+3*j];

    centroidfit[i][j] = ecal1*params[1+3*j] + ecal2;
    fwhmfit[i][j] = params[2+3*j]*ecal1;
    sfitfnsinglepeak->SetParameters(singleparamset);

    //                pkarea = sfitfnsinglepeak->Integral(start_channel*0.9, end_channel*1.1)/
        ↪ E_res;
    pkarea = sfitfnsinglepeak->Integral(start_channel*0.9, end_channel*1.1);
    pkareafit[i][j] = pkarea/E_res;
    //                pkareasig = sfitfnsinglepeak->IntegralError(start_channel*0.9,
        ↪ end_channel*1.1, singleparamset, sfitresult->GetCovarianceMatrix().GetSub(3*j,3*j
        ↪ +2,3*j,3*j+2).GetMatrixArray())/E_res;
    pkareasig = sfitfnsinglepeak->IntegralError(start_channel*0.9, end_channel*1.1,
        ↪ singleparamset, sfitresult->GetCovarianceMatrix().GetSub(3*j,3*j+2,3*j,3*j+2).
        ↪ GetMatrixArray());
    pksigfit[i][j] = pkareasig/E_res;;
```

```
            cout << "Peak Centroid: " << params[1+3*j] << "\t\t" << "Peak Area:\t\t\t" << pkarea << "\
                ↪ t+/-\t" << pkareasig << endl;
        }

        c1->Draw();
        c1->Update();
        c1->Draw();

        stringstream canvas_name;

        canvas_name << "Fit #" << i+1 << ".png";

        c1->SaveAs(canvas_name.str().c_str());

        //              cin.ignore();
    }

    ofstream output;
    output.open(file_prefix[0]+".csv");

    for (uint i = 0; i < nmbrofgaus; i++) {
        cout << "////////////////////////// INTEGRAL: PEAK #" << i+1 << "//////////////////////////"
            ↪ << endl;
        cout << "Start time\t" << "End time\t" << "Real time\t" << "Live time\t" << "Dead time\t" << "
            ↪ Fit chi-sq\t" << "Fit Area\t" << "Fit sigma\t" << endl;

        for (UInt_t j = 0; j < dt_meas; j++) {
            output << start_time+j*time_res << "," << start_time+(j+1)*time_res << "," << rt_vals[j]
                ↪ << "," << lt_vals[j] << "," <<dt_vals[j] << "," << pkchi[j] << "," << centroidfit[j
                ↪ ][i] << "," << fwhmfit[j][i] << "," << pkareafit[j][i] << "," << pksigfit[j][i] <<
                ↪ ","<< sumofevents[j] << endl;
            cout << start_time+j*time_res << "\t" << start_time+(j+1)*time_res << "\t" << rt_vals[j]
                ↪ << "\t" << lt_vals[j] << "\t" << dt_vals[j] << "\t" << pkchi[j] << "\t" <<
                ↪ centroidfit[j][i] << "\t" << fwhmfit[j][i] << "\t" << pkareafit[j][i] << "\t" <<
                ↪ pksigfit[j][i] << "\t"<< sumofevents[j] << endl;
        }
    }
} else {
    drawstring1.str("");
    drawstring1 << "channel>>hsingle(" << binning << "," << start_channel << "," << end_channel << ")"
        ↪ ;

    c1->cd(6);

    int i = 0;
    drawstring2.str("");
    drawstring2 << "cyct>" << start_time + i*time_res << "&&cyct<" << start_time + (i+1)*time_res
        ↪ ;

    singleschain->Draw(drawstring1.str().c_str(), drawstring2.str().c_str());
    c1->Update();
    c1->Draw();
    TH1D* h = (TH1D*)c1->GetPad(6)->GetPrimitive("hsingle");

    h->Draw();
    c1->Update();
```

```
        c1->Draw();

    }

    ticks2 = clock();
    cout << "Processing runtime: " << (ticks2 - ticks1)/CLOCKS_PER_SEC << endl;
}
```

The final step in analyzing a fission product gamma-line was to import the peak areas from the *csv* file output from the *peekit* function. This was performed in *Mathematica*©. There were numerous functions derived to account for the uncertainty and to evaluate the consistency of the data. Each actinide target, thorium-232, uranium-235, and uranium-238 were analyzed using the same algorithms but only the analysis script from uranium-235 is present. The end of this script is one fission product analysis.

BIBLIOGRAPHY

BIBLIOGRAPHY

[1] Tr England and Bf Rider. Evaluation and compilation of fission product yields 1993. *Endf 349*, (LA-UR-94-3106):1–173, dec 1994.

[2] B D Pierson, L R Greenwood, M Flaska, and S A Pozzi. Characterization of a fusion neutron generator and gamma-gamma coincidence detector for short-lived fission product yield. *Nucl. Instr. Meth. A*, Manuscript submitted for publication, 2016 submitted.

[3] Arthur Katz and Sima R. Osdoby. The Social and Economic Effects Of Nuclear War, 1982.

[4] Thomas Fürst, Andres B Tschannen, Giovanna Raso, Cinthia a Acka, Don de Savigny, Olivier Girardin, Eliézer K N'goran, and Jürg Utzinger. Effect of an armed conflict on relative socioeconomic position of rural households: case study from western Côte d'Ivoire. *Emerging themes in epidemiology*, 7(1):6, aug 2010.

[5] Daniel H Chivers, Bethany F Lyles Goldblum, H Isselhardt, and Jonathan S Snider. Before the Day After: Using Pre-Detonation Nuclear Forensics to Improve Fissile Material Security. *Arms Control Association*, 38(6):1–6, aug 2008.

[6] P. Serneels and M. Verpoorten. The Impact of Armed Conflict on Economic Performance: Evidence from Rwanda. *Journal of Conflict Resolution*, page 39, dec 2013.

[7] Tom Collina, Kelsey Davenport, Daryl Kimball, and Greg Thielmann. Solving the Iranian Nuclear Puzzle. Technical Report February, Arms Control Association, aug 2013.

[8] Kelsey Davenport and Arms Control Association. Chronology of U.S.-North Korean Nuclear and Missile Diplomacy. *Arms Control Association*, may 2011.

[9] Matthew G. Bunn, Martin Benjamin Malin, Nickolas James Roth, and William H. Tobey. Advancing Nuclear Security: Evaluating Progress and Setting New Goals. 2014.

[10] Leonard Spector and Egle Murauskaite. *Countering Nuclear Commodity Smuggling: A System of Systems*. CNS Occasional Papers. James Martin Center for Nonproliferation Studies, mar 2014.

[11] Matthew Phillips. Uncertain justice for nuclear terror: Deterrence of anonymous attacks through attribution. 51(3):429–446.

[12] William James Perry, Brent Scowcroft, and Charles D. Ferguson. *U.S. Nuclear Weapons Policy*. Council on Foreign Relations, 2009.

[13] Michael May, Reza Abedin-Zadeh, Donald Barr, Albert Carnesale, Philip E. Coyle, Jay Davis, William Dorland, William Dunlop, Steve Fetter, Alexander Glaser, Others, Joint Working Group, American Physical Society, APS, Joint Working Group, American Physical Society, Michael May, Reza Abedin-Zadeh, Donald Barr, Albert Carnesale, APS, and May Michael. Nuclear Forensics: Role State of the Art, and Program Needs. Technical report, American Physical Society, dec 2008.

[14] Michael J. Kristo. Nuclear Forensics. In *Handbook of Radioactivity Analysis*, pages 1281–1304. Elsevier, third edit edition, 2012.

[15] Jeremy J. Bellucci, Antonio Simonetti, Christine Wallace, Elizabeth C. Koeman, and Peter C. Burns. Isotopic fingerprinting of the world's first nuclear device using post-detonation materials. *Analytical Chemistry*, 85(8):4195–4198, apr 2013.

[16] Christine Wallace, Jeremy J. Bellucci, Antonio Simonetti, Tim Hainley, Elizabeth C. Koeman, and Peter C. Burns. A multi-method approach for determination of radionuclide distribution in trinitite. *Journal of Radioanalytical and Nuclear Chemistry*, 298(2):993–1003, nov 2013.

[17] Nicholas Sharp, William F. McDonough, Brian W. Ticknor, Richard D. Ash, Philip M. Piccoli, and Dana T. Borg. Rapid analysis of trinitite with nuclear forensic applications for post-detonation material analyses. *Journal of Radioanalytical and Nuclear Chemistry*, 302(1):57–67, oct 2014.

[18] Pravin P. Parekh, Thomas M. Semkow, Miguel A. Torres, Douglas K. Haines, Joseph M. Cooper, Peter M. Rosenberg, and Michael E. Kitto. Radioactivity in Trinitite six decades later. *Journal of Environmental Radioactivity*, 85(1):103–120, 2006.

[19] Jeremy J. Bellucci and Antonio Simonetti. Nuclear forensics: Searching for nuclear device debris in trinitite-hosted inclusions. *Journal of Radioanalytical and Nuclear Chemistry*, 293(1):313–319, jul 2012.

[20] F. Belloni, J. Himbert, O. Marzocchi, and V. Romanello. Investigating incorporation and distribution of radionuclides in trinitite. *Journal of Environmental Radioactivity*, 102(9):852–862, sep 2011.

[21] Elizabeth C. Koeman, Antonio Simonetti, Wei Chen, and Peter C. Burns. Oxygen isotope composition of trinitite postdetonation materials. *Analytical Chemistry*, 85(24):11913–11919, dec 2013.

[22] Thomas M. Semkow, Pravin P. Parekh, and Douglas K. Haines. Modeling the Effects of the Trinity Test. In *Applied Modeling and Computations in Nuclear Science*, volume 945 of *ACS Symposium Series*, pages 142–159. American Chemical Society, nov 2007.

[23] Jay Davis. Post detonation nuclear forensics. volume 1596, pages 206–209. AIP Publishing, may 2014.

[24] Charles A. Ziegler and David Jacobson. *Spying Without Spies: Origins of America's Secret Nuclear Surveillance System*. Greenwood Publishing Group.

[25] Jon M. Schwantes, Matthew Douglas, Steven E. Bonde, James D. Briggs, Orville T. Farmer, Lawrence R. Greenwood, Elwood A. Lepel, Christopher R. Orton, John F. Wacker, and Andrzej T. Luksic. Nuclear archeology in a bottle: Evidence of pre-trinity U.S. weapons activities from a waste burial site. *Analytical Chemistry*, 81(4):1297–1306, feb 2009.

[26] a J Fahey, C J Zeissler, D E Newbury, J Davis, and R M Lindstrom. Postdetonation nuclear debris for attribution. *Proceedings of the National Academy of Sciences of the United States of America*, 107(47):20207–20212, 2010.

[27] Jeremy J. Bellucci, Antonio Simonetti, Christine Wallace, Elizabeth C. Koeman, and Peter C. Burns. Lead isotopic composition of trinitite melt glass: Evidence for the presence of Canadian industrial lead in the first atomic weapon test. *Analytical Chemistry*, 85(15):7588–7593, aug 2013.

[28] Jeremy J. Bellucci, Christine Wallace, Elizabeth C. Koeman, Antonio Simonetti, Peter C. Burns, Jeremy Kieser, Eli Port, and Terri Walczak. Distribution and behavior of some radionuclides associated with the Trinity nuclear test. *Journal of Radioanalytical and Nuclear Chemistry*, 295(3):2049–2057, mar 2013.

[29] Jeremy J. Bellucci, Antonio Simonetti, Elizabeth C. Koeman, Christine Wallace, and Peter C. Burns. A detailed geochemical investigation of post-nuclear detonation trinitite glass at high spatial resolution: Delineating anthropogenic vs. natural components. *Chemical Geology*, 365:69–86, feb 2014.

[30] Y. M. Jubeli and S. J. Parry. A new application of neutron activation analysis with 239U to determine uranium in groundwaters. *Journal of Radioanalytical and Nuclear Chemistry Articles*, 102(2):337–346, dec 1986.

[31] R. Zeisler, N. Vajda, G. Kennedy, G. Lamaze, and G. L. Molnr. Activation analysis. In Attila Vrtes, Sndor Nagy, Zoltn Klencsr, Rezs G. Lovas, and Frank Rsch, editors, *Handbook of Nuclear Chemistry*, pages 1553–1617. Springer US.

[32] N. M. Spyrou. Cyclic activation analysis-A review. *Journal of Radioanalytical Chemistry*, 61(1-2):211–242, mar 1981.

[33] R. Zeisler, G. P. Lamaze, and H. H. Chen-Mayer. Coincidence and anti-coincidence measurements in prompt gamma neutron activation analysis with pulsed cold neutron beams. *Journal of Radioanalytical and Nuclear Chemistry*, 248(1):35–38, apr 2001.

[34] S. Wu, R. Donangelo, J. O. Rasmussen, A. V. Daniel, J. K. Hwang, A. V. Ramayya, and J. H. Hamilton. Resolution of complex γ spectra from triple-coincidence data: BaMo split in 252Cf spontaneous fission. *Nuclear Instruments and Methods in Physics Research Section A: Accelerators, Spectrometers, Detectors and Associated Equipment*, 480(2-3):776–781, mar 2002.

[35] Xiaolin Hou. Cyclic activation analysis. pages 12447–12459. John Wiley and Sons, Chichester, 2000.

[36] Kenneth S. Krane and David Halliday. *Introductory Nuclear Physics*, volume 24. Wiley, nov 1987.

[37] Hans-Jürg Kreiner. Nuclear Charge Distribution of Light Fission Products Measured by Direct Gammaspectroscopy. *Radiochimica Acta*, 24(1):8–10, 1977.

[38] A. C. Wahl, R. L. Ferguson, D. R. Nethaway, D. E. Troutner, and K. Wolfsberg. Nuclear-charge distribution in low-energy fission. *Physical Review*, 126(3):1112, 1962.

[39] J.P. Bocquet and R. Brissot. Mass, energy, and nuclear charge distribution of fission fragments. *Nuclear Physics A*, 502:213–232, 1989.

[40] P. Casoli, T. Ethvignot, T. Granier, R. O. Nelson, N. Fotiades, M. J. Devlin, D. M. Drake, W. Younes, P. E. Garrett, and J. A. Becker. Study of the Mass and Charge Distribution of Fragments from Fission Induced by Intermediate Energy Neutrons on Uranium 238. Technical report, Los Alamos National Laboratory, jan 2004.

[41] D. H. Beddingfield and F. E. Cecil. Identification of fissile materials from fission product gamma-ray spectra. *Nuclear Instruments and Methods in Physics Research, Section A: Accelerators, Spectrometers, Detectors and Associated Equipment*, 417(2-3):405–412, 1998.

[42] M. Al-Mugrabi and N. M. Spyrou. The determination of uranium using short-lived fission products by cyclic and other modes of activation analysis. *Journal of Radioanalytical and Nuclear Chemistry Articles*, 112(2):277–283, may 1987.

[43] A. Iyengar, E. B. Norman, C. Howard, C. Angell, A. Kaplan, J. J. Ressler, P. Chodash, E. Swanberg, A. Czeszumska, B. Wang, R. Yee, and H. a. Shugart. Distinguishing fissions of 232Th, 237Np and 238U with beta-delayed gamma rays. *Nuclear Instruments and Methods in Physics Research, Section B: Beam Interactions with Materials and Atoms*, 304:11–15, jun 2013.

[44] M. Eibach, T. Beyer, K. Blaum, M. Block, K. Eberhardt, F. Herfurth, C. Geppert, J. Ketelaer, J. Ketter, J. Krämer, a. Krieger, K. Knuth, Sz Nagy, W. Nörtershäuser, and C. Smorra. Transport of fission products with a helium gas-jet at TRIGA-SPEC. *Nuclear Instruments and Methods in Physics Research, Section A: Accelerators, Spectrometers, Detectors and Associated Equipment*, 613(2):226–231, feb 2010.

[45] Ellene Tratras Contis, Krish Rengan, and Henry C. Griffin. Gas phase chemical reactions of fission products with ethylene using the gas jet technique. *Nuclear Instruments and Methods in Physics Research, Section A: Accelerators, Spectrometers, Detectors and Associated Equipment*, 422(1-3):502–504, feb 1999.

[46] K. Rengan, J. Lin, M. Zendel, and R.A. Meyer. On-line system for the isolation and study of 0.5 to 30 second selenium fission products with simultaneous suppression of

daughter bromine activity. *Nuclear Instruments and Methods in Physics Research*, 197(2-3):427–434, 1982.

[47] Ch E. Düllmann, B. Eichler, R. Eichler, H. W. Gäggeler, D. T. Jost, U. Kindler, D. Piguet, S. Soverna, P. Thörle, N. Trautmann, and A. Türler. Miss Piggy, a californium-252 fission fragment source as a generator of short-lived radionuclides. *Nuclear Instruments and Methods in Physics Research, Section A: Accelerators, Spectrometers, Detectors and Associated Equipment*, 512(3):595–605, oct 2003.

[48] J. D. Baker, D. H. Meikrantz, R. J. Gehrke, and R. C. Greenwood. Nuclear Decay Studies of Rare-earth Fission Product Nuclides using Fast Radiochemical Separation Techniques. *Journal of Radioanalytical and Nuclear Chemistry*, 142(1):159–171, sep 1990.

[49] G. Sadler, T. A. Khan, K. Sistemich, J.W. Grüter, H. Lawin, W.D. Lauppe, H.A. Selič, M. Shaanan, F. Schussler, J. Blachot, E. Monnand, G. Bailleul, J.P. Bocquet, P. Pfeiffer, H. Schrader, and B. Fogelberg. Studies of the β-decay of 96Y and the level scheme of 96Zr. *Nuclear Physics A*, 252(2):365–380, nov 1975.

[50] M. Huhta, P. Dendooven, A. Honkanen, G. Lhersonneau, M. Oinonen, H. Penttilä, K. Peräjärvi, V. Rubchenya, and J. Äystö. Independent yields of neutron-rich nuclei in charged-particle induced fission. *Nuclear Instruments and Methods in Physics Research Section B: Beam Interactions with Materials and Atoms*, 126(1-4):201–204, apr 1997.

[51] S. Tipnis, J. Campbell, G. Couchell, S. Li, H. Nguyen, D. Pullen, W. Schier, E. Seabury, and T. England. Yields of short-lived fission products produced following 235U(nth,f). *Physical Review C*, 58(2):905–915, aug 1998.

[52] W. Reisdorf, J.P. Unik, H.C. Griffin, and L.E. Glendenin. Fission fragment K x-ray emission and nuclear charge distribution for thermal neutron fission of 233U, 235U, 239Pu and spontaneous fission of 252Cf. *Nuclear Physics A*, 177(2):337–378, 1971.

[53] G. Bailleul, J. P. Bocquet, H. Schrader, R. Stippler, B. Pfeiffer, M. Asghar, C. Chauvin, J. P. Gautheron, J. Greif, G. Siegert, P. Armbruster, H. Ewald, J. Blachot, E. Monnand, and F. Schussler. Gamma-ray spectroscopy of short-lived fission products using the recoil separator "Lohengrin". *Zeitschrift für Physik A: Atoms and Nuclei*, 273(3):283–289, sep 1975.

[54] A. Bail, O. Serot, L. Mathieu, O. Litaize, T. Materna, U. Köster, H. Faust, A. Letourneau, and S. Panebianco. Isotopic yield measurement in the heavy mass region for 239Pu thermal neutron induced fission. *Physical Review C - Nuclear Physics*, 84(3):034605, sep 2011.

[55] K. T. Bainbridge. Trinity.

[56] Graham Allison. Nuclear Terrorism Fact Sheet. *Belfer Center for Science and International Affairs, Harvard Kennedy School. Belfer Center for Science and International Affairs*, 2010.

[57] William Burr. *The Atomic Bomb and the End of World War II: A Collection of Primary Sources*, volume 318. National Security Archive, jun 2005.

[58] S. D. Cannan. History of the Plutonium Production Facilities at the Hanford Site Historic District - 1943 - 1990 - June 2002. Technical report, PNNL (US), dec 2001.

[59] Battle. Documents on the u.s. atomic energy detection system [AEDS].

[60] Mary Welch. AFTAC celebrates 50 years of long range detection. pages 8–32.

[61] National Academy of Science, G. Pinte, M. A. R. Veado, A. H. Oliveira, M. Khalis, S. Ayrault, and G. Revel. *Technical Issues Related to the Comprehensive Nuclear Test Ban Treaty*, volume 373-374. The National Academies Press, Washington, DC, jun 2002.

[62] Oleg Bukharin, Pavel Leonardovich Podvig, and Frank Von Hippel. *Russian Strategic Nuclear Forces*. MIT Press.

[63] Matthew Bunn. Loose Nukes Fears: Anecdotes of the Current Crisis. *unpublished memorandum (5 December 1998)*, 51(2):225–235, mar 1998.

[64] Douglas Birch. Letting Go of Loose Nukes, 2012.

[65] Klaus Mayer, Maria Wallenius, and Ian Ray. Nuclear forensics–a methodology providing clues on the origin of illicitly trafficked nuclear materials. *The Analyst*, 130(4):433–441, mar 2005.

[66] Maria Wallenius, Klaus Lützenkirchen, Klaus Mayer, Ian Ray, Laura Aldave de las Heras, Maria Betti, Omer Cromboom, Marc Hild, Brian Lynch, Adrian Nicholl, Herbert Ottmar, Gert Rasmussen, Arndt Schubert, Gabriele Tamborini, Hartmut Thiele, Werner Wagner, Clive Walker, and Evelyn Zuleger. Nuclear forensic investigations with a focus on plutonium. *Journal of Alloys and Compounds*, 444-445(SPEC. ISS.):57–62, 2007.

[67] I D Hutcheon, P M Grant, K J Moody, Attila Vértes, Sándor Nagy, Zoltán Klencsár, Rezs G Lovas, and Frank Rösch. Nuclear Forensic Materials and Methods. Number Chapter 62, pages 2837–2891. Springer US, Boston, MA, 2011.

[68] Charles Streeper, Marcie Lombardi, and Lee Cantrell. Nefarious Uses of Radioactive Materials. In *Nuclear Instruments and Methods in Physics Research Section A: Accelerators, Spectrometers, Detectors and Associated Equipment*, volume 301, pages 543–551, mar 2007.

[69] Incident and Trafficking Database (ITDB) Factsheet, 2015.

[70] IAEA. *Advances in destructive and non-destructive analysis for environmental monitoring and nuclear forensics*. Number October. International Atomic Energy Agency, Vienna, 2003.

[71] IAEA. International Conference on Advances in Nuclear Forensics: Book of Abstracts. Technical report, International Atomic Energy Agency, jul 2014.

[72] IAEA. *Combating Illicit Trafficking in Nuclear and Other Radioactive Material*. Number 6. International Atomic Energy Agency, 2008.

[73] Congress. *Public Law 111 140, 111th Congress, Nuclear Forensics and Attribution Act*, volume 110. US Government Printing Office, 2010.

[74] Floyd E. Stanley, a. M. Stalcup, and H. B. Spitz. A brief introduction to analytical methods in nuclear forensics. *Journal of Radioanalytical and Nuclear Chemistry*, 295(2):1385–1393, 2013.

[75] Joel R. Gat and R. Gonfiantini. Stable isotope hydrology. Deuterium and oxygen-18 in the water cycle. 1981.

[76] Michael J. Kristo and Scott J. Tumey. The state of nuclear forensics. *Nuclear Instruments and Methods in Physics Research, Section B: Beam Interactions with Materials and Atoms*, 294:656–661, jan 2013.

[77] David Atkatz. Determining the yield of the Trinity nuclear device via gamma-ray spectroscopy. *American Journal of Physics*, 63(5):411, may 1995.

[78] Krish Rengan, Daniel DeVries, and Henry Griffin. Gamma rays emitted in the decay of 238Np. *Nuclear Instruments and Methods in Physics Research, Section A: Accelerators, Spectrometers, Detectors and Associated Equipment*, 565(2):612–622, sep 2006.

[79] Zsolt Varga, Róbert Katona, Zsolt Stefánka, Maria Wallenius, Klaus Mayer, and Adrian Nicholl. Determination of rare-earth elements in uranium-bearing materials by inductively coupled plasma mass spectrometry. *Talanta*, 80(5):1744–1749, mar 2010.

[80] M Wallenius and K Mayer. Age determination of plutonium material in nuclear forensics by thermal ionisation mass spectrometry. *Fresenius' journal of analytical chemistry*, 366(3):234–238, 2000.

[81] Scott D. Harvey, Martin Liezers, Kathryn C. Antolick, Ben J. Garcia, Luke E. Sweet, April J. Carman, and Gregory C. Eiden. Porous chromatographic materials as substrates for preparing synthetic nuclear explosion debris particles. *Journal of Radioanalytical and Nuclear Chemistry*, 298(3):1885–1898, dec 2013.

[82] F. G. Gosling. The Manhattan Project: Making the Atomic Bomb. 1999 Edition. Technical Report 2, USDOE Office of Human Resources and Administration, Washington, DC (United States), jan 1999.

[83] Alfred O. Nier, E. T. Booth, J. R. Dunning, and A. V. Grosse. Nuclear Fission of Separated Uranium Isotopes. *Physical Review*, 57(6):546–546, mar 1940.

[84] William E. Parkins. The uranium bomb, the calutron, and the space-charge problem. *Physics Today*, 58(5):45–51, oct 2005.

[85] N. S. Mokgalaka and J. L. GardeaTorresdey. Laser Ablation Inductively Coupled Plasma Mass Spectrometry: Principles and Applications. *Applied Spectroscopy Reviews*, 41(2):131–150, may 2006.

[86] Sarah Benson, Chris Lennard, Philip Maynard, and Claude Roux. Forensic applications of isotope ratio mass spectrometryA review. *Forensic Sci. Int.*, 157(1):1–22, February 2006.

[87] Klaus Mayer, Maria Wallenius, and Ian Ray. Tracing the Origin of Diverted or Stolen Nuclear Material through Nuclear Forensic Investigations. In Professor Dr Rudolf Avenhaus, Professor Dr Nicholas Kyriakopoulos, Dr Michel Richard, and Dr Gotthard Stein, editors, *Verifying Treaty Compliance: Limiting Weapons of Mass Destruction and Monitoring Kyoto Protocol Provisions*, pages 389–408. Springer Berlin Heidelberg, 2006.

[88] N. Erdmann, M. Nunnemann, K. Eberhardt, G. Herrmann, G. Huber, S. Köhler, J.V. Kratz, G. Passler, J.R. Peterson, N. Trautmann, and a. Waldek. Determination of the first ionization potential of nine actinide elements by resonance ionization mass spectroscopy (RIMS). *Journal of Alloys and Compounds*, 271-273:837–840, jun 1998.

[89] Johanna Sabine Becker, Hans-Joachim Dietze, Johanna Sabine Becker, and Hans-Joachim Dietze. Inorganic trace analysis by mass spectrometry. *Spectrochimica Acta Part B: Atomic Spectroscopy*, 53(11):1475–1506, oct 1998.

[90] Robert R. Greenberg, Peter Bode, and Elisabete a. De Nadai Fernandes. Neutron activation analysis: A primary method of measurement. *Spectrochimica Acta - Part B Atomic Spectroscopy*, 66(3-4):193–241, mar 2011.

[91] E. E. Haller. Germanium: From its discovery to SiGe devices. *Materials Science in Semiconductor Processing*, 9(4-5 SPEC. ISS.):408–422, jun 2006.

[92] G. T. Ewan and A. J. Tavendale. Application of high resolution lithium-drift germanium gamma-ray spectrometers to high energy gamma-rays. *Nuclear Instruments and Methods*, 26:183–186, 1964.

[93] D. V. Freck and J. Wakefield. Gamma-Ray Spectrum obtained with a Lithium-drifted pin Junction in Germanium. *Nature*, 193(4816):669–669, feb 1962.

[94] Gordon Gilmore. *Practical gamma-ray spectrometry*. Wiley, Chichester, England; Hoboken, NJ, 2008.

[95] H. R. Koch, H. G. Börner, J. A. Pinston, W. F. Davidson, J. Faudou, R. Roussille, and O. W. B. Schult. The curved crystal gamma ray spectrometers GAMS 1, GAMS 2, GAMS 3 for high resolution (n, γ) measurements at the high flux reactor in Grenoble. *Nuclear Instruments and Methods*, 175(23):401–423, sep 1980.

[96] M. Szlachetko, M. Berset, J.-Cl Dousse, J. Hoszowska, and J. Szlachetko. High-resolution Laue-type DuMond curved crystal spectrometer. *Review of Scientific Instruments*, 84(9):093104, sep 2013.

[97] G.F. Knoll. *Radiation detection and measurement*, volume 171. John Wiley & Sons, 1980.

[98] H. Bateman. *Solution of a System of Differential Equations Occurring in the Theory of Radioactive Transformations*, volume 15. 1910.

[99] Robley D. Evans and Richard O. Evans. Studies of self-absorption in gamma-ray sources. *Reviews of Modern Physics*, 20(1):305, 1948.

[100] Lawrence R. Greenwood and Christian D. Johnson. User guide for the staysl pnnl suite of software tools.

[101] Eri Jay Cohen. Live time and pile-up correction for multichannel analyzer spectra. *Nuclear Instruments and Methods*, 121(1):25–32, 1974.

[102] IAEA. *Neutron Generators for Analytical Purposes*, volume 1. International Atomic Energy Agency, Vienna, 1 edition, 2012.

[103] Ye.P. Bogolubov, S.A. Korotkov, L.A. Korytko, V.G. Morukov, V.I. Nazarov, Yu.G. Polkanov, and T.O. Khasaev. Method and system based on pulsed neutron generator for fissile material detection in luggage. *Nuclear Instruments and Methods in Physics Research Section B: Beam Interactions with Materials and Atoms*, 213:439–444, January 2004.

[104] Ulrich Brosa, Siegfried Grossmann, and Andreas Mller. Nuclear scission. *Phys. Rep.*, 197(4):167–262, 1990.

[105] S M Polikanov. Spontaneously fissioning isomers. *Sov. Phys. Uspekhi*, 11(1):22–33, January 1968.

[106] S.I. Mulgin, K.-H. Schmidt, A. Grewe, S.V. V Zhdanov, S I Mulgina, K.-H. Schmidt, A. Grewe, and S.V. V Zhdanov. Shell effects in the symmetric-modal fission of pre-actinide nuclei. *Nuclear Physics A*, 640(3-4):375–388, 1998.

[107] A. Wahl. Compilation and evaluation of fission yield nuclear data.

[108] Sarah Benson, Chris Lennard, Philip Maynard, and Claude Roux. Forensic applications of isotope ratio mass spectrometry - A review. *Forensic Science International*, 157(1):1–22, 2006.

[109] Rosara F. Payne, J. A. Drader, J. I. Friese, L. R. Greenwood, C. C. Hines, L. A. Metz, J. D. Kephart, M. D. King, B. D. Pierson, J. D. Smith, and D. E. Wall. Neutron fluence and energy reproducibility of a 2-dollar TRIGA reactor pulse. *J. Radioanal. Nucl. Chem.*, 282(1):59–62, July 2009.

[110] D. W. Heikkinen, J. C. Davis, D. J. Massoletti, D. W. Short, and D. B. Tuckerman. The RTNS-II fusion materials irradiation facility. *J. Nucl. Mat.*, 141–143, Part 2:1061–1063, November 1986.

[111] Rtns-ii: Irradiations at the rotating target neutron source-ii. 1983 annual report.

[112] D. R. Nethaway and B. Mendoza. Comparison of yields from fission of ^{233}U, ^{234}U, ^{235}U, ^{236}U, and ^{238}U with 14.8-MeV neutrons. *Phys. Rev. C*, 6(5):1827–1837, November 1972.

[113] D. R. Nethaway and A. E. Richardson. Independent yields of ^{148m}Pm, ^{148g}Pm and ^{150}Pm from fission of ^{235}U and ^{238}U with 14.8 MeV neutrons. *J. Inorg. Nucl. Chem.*, 43(5):889–893, January 1981.

[114] D. R. Nethaway, B. Mendoza, and T. E. Voss. Low-yield products from fission of ^{232}Th, ^{235}U, and ^{238}U with 14.8-MeV neutrons. *Phys. Rev.*, 182(4):1251–1259, August 1969.

[115] D. R. Nethaway and G. W. Barton. Compilation of fission product yields in use at the lawrence livermore laboratory.

[116] M. Mac Innes, M. B. Chadwick, and T. Kawano. Fission product yields for 14 MeV neutrons on 235U, 238U and 239Pu. *Nuclear Data Sheets*, 112(12):3135–3152, dec 2011.

[117] G. P. Ford and A. E. Norris. Compilation of Yields from Neutron-Induced Fission of /Sup 232/Th, /Sup 235/U, /Sup 236/U, /Sup 237/Np, /Sup 238/U, and /Sup 239/Pu Measured Radiochemically at Los Alamos. Technical report, Los Alamos Scientific Lab., N.Mex. (USA), oct 1975.

[118] V. A. Roshchenko, V. M. Piksaikin, S. G. Isaev, and A. A. Goverdovski. Energy dependence of nuclear charge distribution in neutron induced fission of z-even nuclei. *Phys. Rev. C*, 74(1):014607, July 2006.

[119] Ho Manh Dung, Menno Blaauw, Daniel Beasley, and Maria Do Carmo Freitas. Development of the k 0-based cyclic neutron activation analysis for short-lived radionuclides. *Journal of Radioanalytical and Nuclear Chemistry*, 291(2):485–492, jul 2012.

[120] J. Adam, A. A. Byalko, A. I. Slyusarenko, M. E. Fooks, V. M. Tsoupko-Sitnikov, and A. K. Churakov. Method and program for decay scheme reconstruction based on formal logical analysis of gamma-gamma coincidence matrix. *Nuclear Instruments and Methods in Physics Research, Section A: Accelerators, Spectrometers, Detectors and Associated Equipment*, 385(3):492–500, 1997.

[121] R. M. Lindstrom, R. Zeisler, and R. R. Greenberg. Accuracy and uncertainty in radioactivity measurement for NAA. *Journal of Radioanalytical and Nuclear Chemistry*, 271(2):311–315, feb 2007.

[122] A. De Clercq, H. Thierens, D. De Frenne, P. De Gelder, P. D'Hondt, E. Jacobs, and A.J. Deruytter. Method for the determination of the yields of short-lived fission products. *Nuclear Instruments and Methods*, 173(3):531–536, jul 1980.

[123] M Lammer, A. L Nichols, and International Atomic Energy Agency. *Fission product yield data for the transmutation of minor actinide nuclear waste*. International Atomic Energy Agency.

[124] T. R. England and B. F. Rider. Evaluation and compilation of fission yields.

[125] Richard M. Lambrecht, Katsumi Tomiyoshi, and Toshiaki Sekine. *Radionuclide Generators*, volume 77. Springer US, Boston, MA, 1997.

[126] F. Ajzenberg-Selove. Energy levels of light nuclei A = 16 – 17. *Nuclear Physics A*, 166(1):1–139, April 1971.

[127] D. R. Tilley, H. R. Weller, and C. M. Cheves. Energy levels of light nuclei A= 16 – 17. *Nuclear Physics A*, 564(1):1183, 1993.

[128] S. A. Scott and A. Notea. A new determination of the ^{16}N half-life. *Nuclear Physics*, 77(3):641–649, March 1966.

[129] ORTEC. DSPEC Pro digital gamma-ray spectrometer hardware users manual. Revision C, 2005.

[130] D. Cline and P.M.S. Lesser. Error estimation in non-linear least squares analysis of data. *Nuclear Instruments and Methods*, 82:291–293, May 1970.

[131] Richard M. Lindstrom, Menno Blaauw, and Ronald F. Fleming. The half-life of ^{76}As. *Journal of radioanalytical and nuclear chemistry*, 257(3):489491, 2003.

[132] J.K. Bienlein and Elsbeth Kalsch. The half-life of ^{16}N. *Nuclear Physics*, 50:202–208, January 1964.

[133] Peter R. Gray and Arlen R. Zander. The half-life of ^{16}N. *Nuclear Physics*, 71(2):382–384, September 1965.

[134] D. E. Alburger and G. A. P. Engelbertink. Half-lives of ^{11}Be , ^{15}C, ^{16}N, ^{19}O, and ^{28}Al. *Physical Review C*, 2(5):1594–1596, November 1970.

[135] T. Goorley, M. James, T. Booth, F. Brown, J. Bull, L. J. Cox, J. Durkee, J. Elson, M. Fensin, R. A. Forster, and others. Initial MCNP6 release overview. 180(3):298–315.

[136] S. Ram, N.L. Singh, S.K. Bose, and J.Rama Rao. Absolute yields of some fission products in the fast neutron induced fission of 238U. *Nuclear Instruments and Methods in Physics Research Section B: Beam Interactions with Materials and Atoms*, 24-25:501–502, apr 1987.

[137] A. L. Prindle, D. H. Sisson, D. R. Nethaway, M. V. Kantelo, and R. A. Sigg. Fission of am241 with 14.8-MeV neutrons. 20(5):1824–1830.

[138] C. Bhatia, B. F. Fallin, M. E. Gooden, C. R. Howell, J. H. Kelley, W. Tornow, C. W. Arnold, E. Bond, T. A. Bredeweg, M. M. Fowler, W. Moody, R. S. Rundberg, G. Y. Rusev, D. J. Vieira, J. B. Wilhelmy, J. A. Becker, R. Macri, C. Ryan, S. A. Sheets, M. A. Stoyer, and A. P. Tonchev. Exploratory study of fission product yields of neutron-induced fission of $ˆ{235}\mathrm{U}, ˆ{238}\mathrm{U}$, and $ˆ{239}\mathrm{Pu}$ at 8.9 MeV. 91(6):064604.

[139] R. H. Iyer, H. Naik, A. K. Pandey, P. C. Kalsi, R. J. Singh, A. Ramaswami, and A. G. C. Nair. Measurement of absolute fission yields in the fast neutron-induced fission of actinides: ^{238}u, ^{237}np, ^{238}pu, ^{240}pu, ^{243}am, and ^{244}cm by track-etch-cum-gamma spectrometry. 135(3):227–245.

[140] C. Bhatia, B. Fallin, M.E. Gooden, C.R. Howell, J.H. Kelley, W. Tornow, C.W. Arnold, E.M. Bond, T.A. Bredeweg, M.M. Fowler, W.A. Moody, R.S. Rundberg, G. Rusev, D.J. Vieira, J.B. Wilhelmy, J.A. Becker, R. Macri, C. Ryan, S.A. Sheets, M.A. Stoyer, and A.P. Tonchev. Dual-fission chamber and neutron beam characterization for fission product yield measurements using monoenergetic neutrons. *Nuclear Instruments and Methods in Physics Research Section A: Accelerators, Spectrometers, Detectors and Associated Equipment*, 757:7–19, sep 2014.

[141] M Lammer, A. L Nichols, and International Atomic Energy Agency. Fission Product Yield Data for the Transmutation of Minor Actinide Nuclear Waste. pages 1–353, 2008.

[142] Sea Agostinelli, John Allison, K. al Amako, J. Apostolakis, H. Araujo, P. Arce, M. Asai, D. Axen, S. Banerjee, G. Barrand, and others. GEANT4a simulation toolkit. 506(3):250–303.

[143] John W. Hayes, Erin Finn, Larry Greenwood, and Rick Wittman. Characterization of a Thermo Scientific D711 D-T neutron generator located in a low-scatter facility. *Nuclear Instruments and Methods in Physics Research, Section A: Accelerators, Spectrometers, Detectors and Associated Equipment*, 741:57–66, mar 2014.

[144] XIA LLC. User's manual digital gamma finder (DGF) pixie-4, May 2013. V 2.54.

[145] G.P. Westphal. Instrumental correction of counting losses in nuclear pulse spectroscopy. *Nuclear Instruments and Methods in Physics Research Section B: Beam Interactions with Materials and Atoms*, 1011, Part 2:1047–1050, May 1985.

[146] M. Blaauw, R. F. Fleming, and R. Keyser. Digital signal processing and zero-dead-time counting. 248(2):309–313.

[147] Richard M. Lindstrom and Ronald F. Fleming. Dead time, pileup, and accurate gamma-ray spectrometry. *Radioactivity and Radiochemistry*, 6(2), 1995. Peer Reviewed.

[148] S. I. Kafala. Simple method for true coincidence summing correction. *Journal of radioanalytical and nuclear chemistry*, 191(1):105114, 1995.

[149] B. Blank, J. Souin, P. Ascher, L. Audirac, G. Canchel, M. Gerbaux, S. Grévy, J. Giovinazzo, H. Guérin, T. Kurtukian Nieto, I. Matea, H. Bouzomita, P. Delahaye, G. F. Grinyer, J. C. Thomas, S. Grevy, J. Giovinazzo, H. Guerin, T. Kurtukian Nieto, I. Matea, H. Bouzomita, P. Delahaye, G. F. Grinyer, and J. C. Thomas. High-precision efficiency calibration of a high-purity co-axial germanium detector. *Nuclear Instruments and Methods in Physics Research Section A: Accelerators, Spectrometers, Detectors and Associated Equipment*, 776:34–44, mar 2014.

[150] Rene Brun and Fons Rademakers. ROOT - An object oriented data analysis framework. *Nuclear Instruments and Methods in Physics Research, Section A: Accelerators, Spectrometers, Detectors and Associated Equipment*, 389(1-2):81–86, apr 1997.

[151] M Morhác, J Kliman, M Jandel, L Krupa, and V Matousek. Study of fitting algorithms applied to simultaneous analysis of large numbers of peaks in gamma-ray spectra. *Applied spectroscopy*, 57(7):753–760, jul 2003.

[152] Miroslav Morháč, Ján Kliman, Vladislav Matoušek, Martin Veselský, and Ivan Turzo. Identification of peaks in multidimensional coincidence γ-ray spectra. *Nuclear Instruments and Methods in Physics Research, Section A: Accelerators, Spectrometers, Detectors and Associated Equipment*, 443(1):108–125, 2000.

[153] A. B. Cusick, M. E. Morell-Gonzalez, and M. R. Hartman. Development of a fast-pneumatic sample transfer system for DT neutron activation analysis at the University of Michigan. *Journal of Radioanalytical and Nuclear Chemistry*, 302(3):1137–1141, aug 2014.

[154] G.F. Knoll. *Radiation Detection and Measurement*. John Wiley & Sons, 2010.

[155] J. C. Hardy, V. E. Iacob, M. Sanchez-Vega, R. T. Effinger, P. Lipnik, V. E. Mayes, D. K. Willis, and R. G. Helmer. Precise efficiency calibration of an HPGe detector: source measurements and monte carlo calculations with sub-percent precision. 56(1):65–69.

[156] M. M. B, V. P. Chechev, R. Dersch, O. A. M. Helene, R. G. Helmer, M. Herman, S. Hlav, A. Marcinkowski, G. L. Molnr, A. L. Nichols, and others. Update of x ray and gamma ray decay data standards for detector calibration and other applications, volume 1: Recommended decay data, high energy gamma ray standards and angular correlation coefficients.

[157] Lise Meitner and Otto Frisch. Disintegration of uranium by neutrons: a new type of nuclear reaction. *Nature*, 143:239–240, February 1939.

[158] Kotoyuki Okano, Yoichi Kawase, Yoshihiro Funakoshi, and Ichiro Fujiwara. Half-life measurements of 93Sr, 94Sr, 95Sr, 139Cs, 141Cs and 143Ba mass-separated by KUR-ISOL. *International Journal of Radiation Applications and Instrumentation. Part A. Applied Radiation and Isotopes*, 37(6):521–525, 1986.

[159] K. Meierbachtol, F. Tovesson, D. Shields, C. Arnold, R. Blakeley, T. Bredeweg, M. Devlin, A. A. Hecht, L. E. Heffern, J. Jorgenson, A. Laptev, D. Mader, J. M. ODonnell, A. Sierk, and M. White. The SPIDER fission fragment spectrometer for fission product yield measurements. *Nucl. Instr. Meth. A*, 788:59–66, February 2015.

[160] O. Serot, C. Amouroux, A. Bidaud, N. Capellan, S. Chabod, A. Ebran, H. Faust, G. Kessedjian, U. Kester, A. Letourneau, O. Litaize, F. Martin, T. Materna, L. Mathieu, S. Panebianco, J. M. Regis, M. Rudigier, C. Sage, and W. Urban. Recent results from Lohengrin on fission yields and related decay properties. *Nucl. Data Sheets*, 119:320–323, May 2014.

[161] a Kankainen, J Äystö, and a Jokinen. High-accuracy mass spectrometry of fission products with Penning traps. *Journal of Physics G: Nuclear and Particle Physics*, 39(9):093101, sep 2012.

[162] Eugene Feenberg and Kenyon C. Hammack. Nuclear shell structure. *Phys. Rev.*, 75(12):1877, 1949.

[163] G. Skarnemark, K. Brodén, N. Kaffrell, S. G. Prussin, N. Trautmann, K. Rengan, D. Eriksen, D. F. Kusnezov, and R. A. Meyer. Subshell closure effects on the collectivity of36 88Kr52 and the beta decay of88Br to levels in88Kr. *Zeitschrift für Physik A Atomic Nuclei*, 323(4):407–418, dec 1986.

[164] A. Bhagwat, X. Viñas, M. Centelles, P. Schuck, and R. Wyss. Microscopic-macroscopic approach for binding energies with the Wigner-Kirkwood method. II. Deformed nuclei. *Phys. Rev. C*, 86(4), October 2012.

[165] I. V. Panov, E. Kolbe, B. Pfeiffer, T. Rauscher, K. L. Kratz, and F. K. Thielemann. Calculations of fission rates for r-process nucleosynthesis. *Nucl. Phys. A*, 747(2):633–654, January 2005.

[166] E. Sahin, G. de Angelis, G. Duchene, T. Faul, A. Gadea, A.F. Lisetskiy, D. Ackermann, A. Algora, S. Aydin, F. Azaiez, D. Bazzacco, G. Benzoni, M. Bostan, T. Byrski, I. Celikovic, R. Chapman, L. Corradi, S. Courtin, D. Curien, U. Datta Pramanik, F. Didierjean, O. Dorvaux, M.N. Erduran, S. Erturk, E. Farnea, E. Fioretto, G. de France, S. Franchoo, B. Gall, A. Gottardo, B. Guiot, F. Haas, F. Ibrahim, E. Ince, A. Khouaja, A. Kusoglu, G. La Rana, M. Labiche, D. Lebhertz, S. Lenzi, S. Leoni, S. Lunardi, P. Mason, D. Mengoni, C. Michelagnoli, V. Modamio, G. Montagnoli, D. Montanari, R. Moro, B. Mouginot, D.R. Napoli, D. ODonnell, J.R.B. Oliveira, J. Ollier, R. Orlandi, G. Pollarolo, F. Recchia, J. Robin, M.-D. Salsac, F. Scarlassara, R.P. Singh, R. Silvestri, J.F. Smith, I. Stefan, A.M. Stefanini, K. Subotic, S. Szilner, D. Tonev, D.A. Torres, M. Trotta, P. Ujic, C. Ur, J.J. Valiente-Dobn, D. Verney, M. Yalcinkaya, P.T. Wady, K.T. Wiedemann, and K. Zuber. Structure of the As, Ge, Ga nuclei. *Nucl. Phys. A*, 893:1–12, November 2012.

[167] W. Urban, J. A. Pinston, J. Genevey, T. Rzaca-Urban, A. Zomaniec, G. Simpson, J. L. Durell, W. R. Phillips, A. G. Smith, B. J. Varley, I. Ahmad, and N. Schulz. The $\nu 9/2$ [404] orbital and the deformation in the A 100 region. *European Physical Journal A*, 22(2):241–252, nov 2004.

[168] L. Fiorito, C. J. Diez, O. Cabellos, a. Stankovskiy, G. Van Den Eynde, and P. E. Labeau. Fission yield covariance generation and uncertainty propagation through fission pulse decay heat calculation. *Annals of Nuclear Energy*, 69:331–343, 2014.

[169] A. Iyengar, E. B. Norman, C. Howard, C. Angell, A. Kaplan, J. J. Ressler, P. Chodash, E. Swanberg, A. Czeszumska, B. Wang, R. Yee, and H. A. Shugart. Distinguishing fissions of ^{232}Th, ^{237}Np and ^{238}U with beta-delayed gamma rays. *Nucl. Instr. Meth. B*, 304:11–15, June 2013.

[170] L. R. Greenwood, R. Wittman, B. P. Pierson, L. A. Metz, R. Payne, E. C. Finn, and J. I. Friese. Design and Testing of a Boron Carbide Capsule for Spectral Tailoring in Mixed-Spectrum Reactors. *Journal of ASTM International*, 9(3):103959, 2012.

[171] L. R. Greenwood and J. P. Foster. Retrospective reactor dosimetry with zirconium alloy samples in a pwr. In *Reactor Dosimetry State of the Art 2008*, pages 58–66. World Scientific, August 2009.

[172] Luke W. Campbell, L. Eric Smith, and Alex C. Misner. High-energy delayed gamma spectroscopy for spent nuclear fuel assay. *IEEE Transactions on Nuclear Science*, 58(1 PART 2):231–240, feb 2011.

[173] A. B. Cusick, M. E. Morell-Gonzalez, and M. R. Hartman. Development of a fast-pneumatic sample transfer system for DT neutron activation analysis at the University of Michigan. *J. Radioanal. Nucl. Chem.*, 302(3):1137–1141, August 2014.

[174] Bruce D. Pierson, Henry C. Griffin, Marek Flaska, Jeff a. Katalenich, Brian B. Kitchen, and Sara a. Pozzi. Benchmarking the repeatability of a pneumatic cyclic neutron activation analysis facility using 16O(n,p)16N for nuclear forensics. *Appl. Radiat. Isotopes*, 96:20–26, 2015.

[175] J. Danon. Adsorption of Thorium by anion–exchange resins from nitric acid media. *J. Am. Chem. Soc.*, 78(22):5953–5954, November 1956.

[176] Erin Finn, Lori Metz, Larry Greenwood, Bruce Pierson, Judah Friese, Rosara Kephart, and Jeremy Kephart. Short-lived fission product measurements from >0.1 MeV neutron-induced fission using boron carbide. *J. Radioanal. Nucl. Chem.*, 293(1):267–272, February 2012.

[177] Lawrence R. Greenwood and Christian D. Johnson. User Guide for the STAYSL PNNL Suite of Software Tools. Technical Report PNNL-22253, Pacific Northwest National Laboratory (PNNL), Richland, WA (US), February 2013.

[178] Robley D. Evans and Richard O. Evans. Studies of self-absorption in gamma-ray sources. *Rev. Mod. Phys.*, 20(1):305, 1948.

[179] N. Soppera, M. Bossant, and E. Dupont. JANIS 4: An Improved Version of the NEA Java-based Nuclear Data Information System. *Nucl. Data Sheets*, 120:294–296, June 2014.

[180] A. A. Sonzogni. Nudat 2.0: Nuclear structure and decay data on the internet. *AIP Conf. Proc.*, 769:574, 2005.

[181] E. Browne. Nuclear data sheets for a = 90. *Nucl. Data Sheets*, 82(3):379–546, November 1997.

[182] Ho Manh Dung, Menno Blaauw, Daniel Beasley, and Maria Do Carmo Freitas. Development of the k_0-based cyclic neutron activation analysis for short-lived radionuclides. *J. Radioanal. Nucl. Chem.*, 291(2):485–492, July 2011.

[183] Robert R. Greenberg, Peter Bode, and Elisabete a. De Nadai Fernandes. Neutron activation analysis: A primary method of measurement. *Spectrochim. Acta B*, 66(3-4):193–241, March 2011.

[184] Michael J. Kristo. Nuclear forensics. In *Handbook of Radioactivity Analysis*, pages 1281–1304. Elsevier, 2012.

[185] M.B. Chadwick, M. Herman, P. Obloinsk, M.E. Dunn, Y. Danon, A.C. Kahler, D.L. Smith, B. Pritychenko, G. Arbanas, R. Arcilla, R. Brewer, D.A. Brown, R. Capote, A.D. Carlson, Y.S. Cho, H. Derrien, K. Guber, G.M. Hale, S. Hoblit, S. Holloway, T.D. Johnson, T. Kawano, B.C. Kiedrowski, H. Kim, S. Kunieda, N.M. Larson, L. Leal, J.P. Lestone, R.C. Little, E.A. McCutchan, R.E. MacFarlane, M. MacInnes, C.M. Mattoon, R.D. McKnight, S.F. Mughabghab, G.P.A. Nobre, G. Palmiotti, A. Palumbo, M.T. Pigni, V.G. Pronyaev, R.O. Sayer, A.A. Sonzogni, N.C. Summers, P. Talou, I.J. Thompson, A. Trkov, R.L. Vogt, S.C. van der Marck, A. Wallner, M.C. White, D. Wiarda, and P.G. Young. ENDF/B-VII.1 Nuclear Data for Science and Technology: Cross Sections, Covariances, Fission Product Yields and Decay Data. *Nucl. Data Sheets*, 112(12):2887–2996, December 2011.

[186] Eva M. Zsolnay, Roberto Capote Noy, Henk J. Nolthenius, and Andrej Trkov. Summary description of the new international reactor dosimetry and fusion file (IRDFF release 1.0). Technical report, International Atomic Energy Agency, 2012.

[187] R. Capote, K. Zolotarev, V. Pronyaev, and A. Trkov. Updating and Extending the IRDF-2002 Dosimetry Library. *Updating and Extending the IRDF-2002 Dosimetry Library*, 2012.

[188] J. K. Tuli. Nuclear data sheets for A = 144. *Nuclear Data Sheets*, 56(4):607–707, April 1989.

[189] N. Otuka, E. Dupont, V. Semkova, B. Pritychenko, A. I. Blokhin, M. Aikawa, S. Babykina, M. Bossant, G. Chen, S. Dunaeva, R. A. Forrest, T. Fukahori, N. Furutachi, S. Ganesan, Z. Ge, O. O. Gritzay, M. Herman, S. Hlava, K. Kat, B. Lalremruata, Y. O. Lee, A. Makinaga, K. Matsumoto, M. Mikhaylyukova, G. Pikulina, V. G. Pronyaev, A. Saxena, O. Schwerer, S. P. Simakov, N. Soppera, R. Suzuki, S. Takcs, X. Tao, S. Taova, F. Trknyi, V. V. Varlamov, J. Wang, S. C. Yang, V. Zerkin, and Y. Zhuang. Towards a More Complete and Accurate Experimental Nuclear Reaction Data Library (EXFOR): International Collaboration Between Nuclear Reaction Data Centres (NRDC). *Nucl. Data Sheets*, 120:272–276, June 2014.

[190] D. R. Nethaway and G. W. Barton. Compilation of fission product yields in use at the Lawrence Livermore Laboratory. Technical Report UCRL–51458, California Univ., 1973.

[191] A. C. Wahl, R. L. Ferguson, D. R. Nethaway, D. E. Troutner, and K. Wolfsberg. Nuclear-charge distribution in low-energy fission. *Phys. Rev.*, 126(3):1112, 1962.

[192] A. C. Wahl. Systematics of Fission-Product Yields. Technical Report LA–13928, Los Alamos National Laboratory (LANL), 2002.

[193] J. P. Bocquet, R. Brissot, J. Cranon, and A. Moussa. On-line measurements of rare-gas fission yields in 14 MeV neutron fission. *Nucl.ear Phys. A*, 189(3):556–576, July 1972.

[194] Robert E. Howe. Measurement of Fission Neutron Multiplicities for Thorium-232 and Uranium-235 with Incident Neutron Energies to 49 MeV. *Nucl. Sci. Eng.*, 86(2):157–167, February 1984.

[195] Joann Marie Campbell. Yields of short-lived fission products following fast fission of U-238. *Ph.D. Thesis*, page 103, July 1997.

[196] D. Abriola and A. A. Sonzogni. Nuclear data sheets for a = 96. *Nucl. Data Sheets*, 109(11):2501–2655, November 2008.

[197] N. Nica. Nuclear Data Sheets for A = 97. *Nucl. Data Sheets*, 111(3):525–716, March 2010.

[198] M. Block, C. Bachelet, G. Bollen, M. Facina, C. M. Folden, C. Gunaut, A. A. Kwiatkowski, D. J. Morrissey, G. K. Pang, A. Prinke, R. Ringle, J. Savory, P. Schury, and S. Schwarz. Discovery of a nuclear isomer in ^{65}fe with PenningTrap Mass Spectrometry. *Phys. Rev. Lett.*, 100(13):132501, April 2008.